POLITECNICO DI MILANO

SCHOOL OF INDUSTRIAL AND INFORMATION ENGINEERING

MASTER OF SCIENCE IN ENERGY ENGINEERING

HOT WIRE ANEMOMETRY FOR FLUID-MACHINES WAKE INVESTIGATION: MAIN FLOW PROPERTIES AND TURBULENCE

Supervisor: Prof. Giacomo PERSICO

Master Thesis of:
Giulia BOSCHI Matr. 853038

Academic Year 2016-2017

a mia mamma Angela,
che mi ha insegnato la forza per conquistare i miei obiettivi.

Ringraziamenti

Il più sincero ringraziamento va al Prof. Giacomo Persico, che durante questi ultimi nove mesi mi ha constantemente affiancata, mettendosi in gioco in prima persona e con grande umiltà, gratificando i miei sforzi, dimostrando sempre interesse verso il mio lavoro di Tesi e spronandomi ogni volta a superare me stessa. Dal punto di vista personale e professionale, sicuramente il miglior relatore che uno studente possa desiderare. Insieme a lui ringrazio tutto il gruppo di Fluidodinamica delle Turbomacchine, con i quali ho passato gli ultimi mesi in Laboratorio, in particolare il Prof. Paolo Gaetani, che mi ha dato la possibilità unica di partecipare in prima persona ai test su uno stadio di turbina assiale, e l'Ing. Alberto Fusetti, che ha sempre supportato le nostre campagne di prove. Vorrei inoltre ringraziare con affetto anche gli altri membri del laboratorio, tra cui in particolare il Prof. Alessandro Mora, il Prof. Vincenzo Dossena, e tra i tecnici anche Paolo Grigatti, che hanno saputo dare consigli utili, oltre che sdrammatizzare i fallimenti sul banco di prova. Un altro ringraziamento speciale va alla dottoranda Elissavet Boufidi del VKI e alla ormai Dott.ssa Sara Vassallo, con le quali ho condiviso le lunghe giornate di prove, e che hanno rappresentato per me un appoggio importante, non solo in ambito tecnico.

Un abbraccio commosso a tutti coloro che mi sono stati vicini in questi anni universitari, a partire da quei disgraziati di Bomby, Daniel, Omar, Peri, Tener e Mosca, senza i quali questa esperienza non sarebbe mai stata la stessa. Ringrazio di cuore anche chi ha preso altre strade, ma che mi ha dato a suo modo l'esempio giusto per affrontare questa avventura: Sophie, Monica, e soprattutto Lorenzo, che non ha mai smesso di supportarmi e sopportarmi, vivendo con me i momenti più felici e quelli più bui.

Infine, il ringraziamento più sentito e dovuto va alla mia famiglia intera che ha sempre creduto in me e senza la quale nulla di tutto ciò sarebbe stato possibile. In particolar modo ringrazio mia mamma Angela, la mia roccia. Il vostro aiuto non è stato solo economico, ma soprattutto morale e motivazionale, cosa molto più importante se non imprescindibile.

Extended Abstract

The hot wire anemometer is a miniaturized instrument for velocity measurements based on the principle of heat transfer. It is made of a very thin metal wire, heated up by Joule effect and exposed to a cooling flow. Depending on the cooling potential of the flow in which the wire is immersed, its control unit provides a variable current, to maintain a constant temperature in the sensitive part. The current change can be then related to the velocity of the flow running over the wire by means of the measured output voltage. Thanks to its remarkably high frequency response, the hot wire anemometer is widely used for flow measurements that involve the detection of high frequency unsteady phenomena.

This is the case of the flow downstream of a vertical axis wind turbine (VAWT), a highly unstable wake whose features cannot be captured by a simple time-mean analysis. This kind of machine descends from an idea of G. Darrieus patented in 1931, but it was soon overcome by the horizontal axis wind turbine technology, more efficient on a large scale energy production and characterized by simpler aerodynamics.

Nowadays the concept of energy harvesting is more oriented towards a diffuse production of electricity, in which consumers are also suppliers, and vice versa. It is hence in the new field of microgeneration in the urban environment, that the vertical axis wind turbine prevails on the horizontal axis configuration. Moreover, the vertical axis technology adapts well to the installation in deep off-shore farms, also known as deepwind. Among the benefits of the VAWT there are its insensitivity to yaw angle, gearbox installation at the turbine base, and lower noise due to optimal operation at lower tip-speed ratios. This kind of machine represents thus a promising technology to satisfy the new needs of the energy system, today and in the future. Nowadays, the development of the vertical axis wind turbine can count on powerful computational methods and advanced aerodynamics studies that allowed to develop far more sophisticated procedures for the machine optimal design, addressed as vortex models. For this purpose, the fluid-machines scientific community agrees to focus on the study of the

VAWT wake as the effect of the force exchange between wind and blades, in contrast to the streamtube momentum balance models, which are now considered obsolete. Therefore, the studies presented in this Master Thesis work, conducted on the VAWT wake are of truly actual concern, and they mirror the direction in which the research is going, all over the world. The works of S. Ferreira [1] at TU Delft, and of H. Y. Lam and H. F. Peng [2] at the Hong Kong University, together with the previous studies of the Laboratory fo Fluid Machines (LFM) at Politecnico di Milano carried out in collaboration with the Trento University [3] [4] [5] [6] confirm the global academic feeling upon this topic.

In this work, experimental data on a Darrieus turbine collected during winter 2016/17 in the large scale low-turbulence wind tunnel of Politecnico di Milano have been further elaborated, in order to derive the complete wake flow field, the deterministic unsteadiness, the 2×2 Reynolds stress tensor, and finally the turbulent integral length scale. Only the H-shaped VAWT has been considered, and only in two operating conditions, the optimal and a low loading case. These are identified by a tip-speed ratio (λ), and two kinds of comparisons have been done: first at the same rotational speed and at different tip-speed ratios, and then lower rotational speeds for the same low loading case were compared to evaluate the effect of Reynolds number on similarity. The flow has been characterized on both phase-averaged and unsteady basis. The latter, in particular, is crucial to detect the vortical structures shed in the wake due to dynamic stall. For the first time, in the 2016 campaign, together with the conventional near wake vertical plane, a horizontal measuring grid on the blade-to-blade plane at the machine midspan was sampled. This new idea allows to clearly visualize the vortex shedding and convection along the streamwise direction. For this fundamental reason, the majority of the data elaboration efforts carried out in this work were focused on the blade-to-blade measurements.

The purpose of the work from the point of view of the wind turbine data, was to provide the LFM software written in Fortran 90 with more advanced routines for the calculation of the yaw angle and the 2D Reynolds stress tensor, both phase-averaged and unsteady, together with a third routine for the evaluation of the turbulent integral length scale. These codes, whose algorithms are fully explained in the fifth chapter, have been successfully implemented in the main program, and provided the team with a compete vision of the straight hot wire possibilities for a deep flow characterization. Besides, the work done on the wind data ended up with a wider overview on the criticalities of hot wire measurements during elaboration. The slanted hot wire shall be abandoned for pitch angle

evaluations, and evidence to support this statement is provided in chapter six. On the other hand, the slanted wire may be a good instrument to investigate turbulence, for instance, to pass from a 2D to a 3D Reynolds tensor. The results of hot wire measurements on the vertical axis wind turbine confirm the expected trends on the basis of previous rougher calculations, and show the improvements obtained with the newly implemented routines.

The investigation of the flow downstream of the stator of the axial turbine stage located in the Laboratory of Fluid-Machines of the Energy Department of Politecnico di Milano, was instead carried out in winter 2017/18, while the present Thesis work was underway. The chance for this second part of the work was given by the collaboration with a Ph.D. student from the Von Karman Institute for Fluid-Dynamics. With her and a mechanical engineering collegue, who was already working on the TC rig with the FRAP probe for her Master Thesis, the stator wake was investigated with a straight hot wire anemometer for the first time. For this very reason, the task was quite challenging, and the hot wire was placed in the axial gap between stator and rotor, to sample the stator wake, for a start. As a matter of fact, due to its particularly steady state flow, the field downstream of the stator was expected to be a favorable measuring condition compared to the rotor unsteady wake. Up to now, the flow of the axial turbine of the TC test rig has been investigated with the unsteady FRAP probe. The great advantage of the hot wire over the FRAPP, is essentially its geometry, that allows to get closer to the hub along the radial position, and hence to map the hub structures, which are quite relevant and interesting to see. Besides, since the hot wire can provide more accurate results on turbulence compared to the FRAPP, it would be useful to have an alternative probe to support the FRAPP on turbulence measurements. The experimental campaign carried out on the high-pressure turbine stage with the anemometer, hence, was meant to be the starting point for further investigations in the application of this kind of probe in such a facility. The goal was to increase the experience of the team with hot wires in diverse applications. For this purpose, the present Thesis work was engaged in this new experimental campaign, and it became the chance to observe the behavior of the instrument in two different applications.

In this case, only the time mean data were elaborated, since downstream of the stator periodic unsteadiness is particularly weak, as it is related only to the rotor pressure field propagating upstream, in the gap between the two cascades. The first results to be investigated were the velocity field and the yaw angle, and to this purpose, the same routines

of the wind data were implemented for this new domain. During these tests, several issues arose, among which the most evident are for sure the dependency of the probe calibration parameters on temperature and the zero capturing procedure. All these criticalities are then presented in detail in the appendix, since they are considered an important background for future investigations. With the idea to have the hot wire as alternative probe to the FRAPP for flow characterization in the TC rig, the tests of winter 2017/18 discussed in this Thesis, and most of all the uncertainties come to light, open the way to further tests and studies on the applicability of hot wires to high-velocity high-temperature flows. On the other hand, the results obtained for turbulence are much more reliable. These data will be then presented in the results discussion chapter.

The present Thesis work is organized in six chapters, in which the most important steps of the experimental investigation, the elaboration algorithms and the results presentation are discussed in detail. The first chapter gives a rapid overview of the theoretical background that is necessary to understand the topics discussed in the body of the Thesis, with a particular attention to turbulence statistics.

The second chapter, instead, is still mostly theoretical, but it concerns the hot wire probe in detail. The working principle of the anemometer will be presented, together with the related heat transfer equations, and a historical overview of the calibration equations proposed up to now. Nowadays, the King's law for the flow cooling velocity and the Jørgensen equation for the angular sensitivity of the probe are used worldwide, and in this chapter they are presented and explained, since they will be used a lot in the succeeding sections. It is still in the second chapter that a basic description of the probe electronic circuit is given, the Wheatstone bridge is presented, and the difference between constant current and constant temperature configurations is made clear. Besides, a reference frame is proposed. It is indeed of priority importance to distinguish between the reference frame of the wire (relative frame), and the one of the turbine (absolute frame), and to find a correspondence between the two, in order to correctly relate the measurements to the absolute flow properties.

The third chapter goes in the details of calibration and how it has been done in practice on the calibration nozzle of the LFM. For this kind of procedure, the calibration rig operates with pressurized air in open loop coming from tank reservoirs, which is properly throttled to the desired expansion ratio through a valve commanded from the control panel. In this chapter, the equipment of the calibration rig, the monitoring of the main flow quantities of interest, and the moving system of the probe is presented. The same equipment for the hot wires calibration was was

used both for the wind and for the axial stage tests [7]. Afterwards, the steps followed for the calibration procedure are described, such as the connection of the probe to the anemometric unit and its entry into service. Then, the cooling velocity calibration by means of the King's law and the angular calibration through the Jørgensen equation are mentioned, together with the temperature correction and the zero voltage calibration with temperature. To obtain the two parameters of the King's law, the probe was kept still in its position with the calibrating jet coming along the direction perpendicular to the wire and to the probe holder. This procedure, for the TC rig campaign, was repeated first at ambient temperature, as it was historically done for the wind application, and then, after the first criticalities were observed, it was repeated at the flow temperature conditions, in order to give the dependence of the King's parameters on temperature. The yaw and pitch coefficients, instead, considered in the Jørgensen equation, are evaluated by turning the probe around its axes, in order to test the wire sensitivity to a flow coming from different directions. The calibration of the zero voltage, finally, was carried out in a thermostatic oven, and only for the axial-flow stage campaign, since issues regarding the zero capturing and its dependency with temperature have been observed herein.

In chapter four, the experimental apparatus is described, and its technical characteristics are presented. These are the wind tunnel facility, the testing prototype of the vertical axis wind turbine, and the TC test rig for the axial stage campaign. Besides, also the measuring grids of all the sampled planes are presented. This chapter is actually fundamental to make the results comparable with other tests.

The fifth chapter represents the core of the whole work, since it reports all the data processing algorithms implemented in the LFM software, that allow to pass from a raw voltage measurement to several flow properties of interest. Some of these procedures are iterative, since they require the solution of a strongly non-linear system of equations, such as the yaw and pitch angle algorithms, and the solution to the over-constrained systems of equations for the Reynolds stresses. The other algorithms are instead linear, and given a certain input, the output can be derived straightaway. This is the case of the iso-constrained Reynolds stress and the turbulent integral length scale. As largely recommended for experimental data elaboration, where available, a certain over-determination of the solving systems was preferred. This is the case of the application of the Jørgensen equations to the yaw and pitch algorithms, and in particular for the slanted hot wire, that typically requires a high degree of overdetermination. In any case, the results of the normal wire presented in

chapter six, show similar trends and with relatively little displacement from the highly over-constrained solution.

Several sensitivity analyses were carried out on the numerical methods implemented in this work, and they all gave a positive outcome concerning the robustness of the numerical procedures, except for the pitch angle calculation with the slanted hot wire. This algorithm presentes an improvement compared to the one used in previous works [7], but the results do not seem to get better, compared to previous five-hole probe assessments. The analyses on the numerical procedures were carried out mainly on a sample measuring grid made of fewer points. It is the case not only of the pitch algorithm, but also of the validation of the number of equations to use to constrain the problems.

The sixth chapter of results discussion on the wind turbine is divided in two, a first part that regards the vertical 2D plane, and a second one where the horizontal blade-to-blade plane is commented. The 2D maps give the chance to comment on the main features of the overall VAWT wake, since all the regions, from midspan to tip and from leeward to windward are measured. Thanks to these maps, it is then possible to comment on the overall machine aerodynamics, and the contours presented in the steady and unsteady forms, exactly reflect the expectations from previous works [5] [1]. Furthermore, the unsteady evolution of the wake is particularly interesting, mainly for the low loading condition, which is the one showing higher unsteadiness. It is in this case that the time-depending analysis shows its avails against the phase-averaged results. The blade-to-blade plane, instead, presents the wake only at midspan, and hence here no tip region is detected. Nevertheless, this gives the possibility to clearly visualize the vortices shed by the machine, that in the 2D plane are just foreseen. On this plane, it makes sense also to plot the sole periodic velocity components cleaning the map from the time-mean velocity. This is a way to isolate the vortices and see how they stretch and convect along the stream-cross direction. In the second part of chapter six, the results for the axial stage and the comparison between the iso and the over-constrained problem are shown. For this case, as previously discussed, only the Reynolds stresses are presented and interpreted.

Looking globally at the work done in this Thesis, many conclusions can be drawn. First of all, the hot wire anemometer cannot be used in the same way for the wind and the axial-flow turbine stage, the two conditions are too different, especially in terms of air velocity and temperature. Some precautions need to be undertaken, and further tests and studies shall be implemented to deeply understand the behavior of the hot wire with this kind on flows. The objective may be to have another

high-accuracy unsteady instrument such as the hot wire, to support the FRAPP measurements in the TC axial-flow stage. To what emerges from the results on the rig, these concerns apply mainly to the yaw angle and velocity magnitude measurements, while turbulence is well captured. The other very important message that this Thesis work wants to pass regards wind tunnel measurements on the vertical axis wind turbine. The data processing developed in the present work shows the potential carried by blade-to-blade plane measurements. Regarding this topic, two paths shall be undertaken, a first one is the improvement of the Reynolds stress from a 2D to a 3D tensor, including also the components on the longitudinal direction, while another one may be the sampling of other planes rather than midspan, with the idea of moving then from a 2D to a 3D experimental wake characterization.

When I meet God, I am going to ask him two questions:
Why relativity? And why turbulence?
I really believe he will have an answer for the first.

Werner Heisenberg [1901 - 1976]

Abstract

This Master Thesis is an experimental investigation on the application of hot wire anemometry in two very different kinds of fluid-machine wakes: a H-shaped vertical axis wind turbine and an axial high-pressure turbine stage. Its objective is to understand how the same measurement technique can be used to study a flow in two very different conditions, and the issues that may arise.

A rich experimental database collected in 2016/17 for the H-shape vertical axis wind turbine was used to map the wind flow field, turbulence, the 2×2 Reynolds stress tensor and the turbulent integral length scale, both for phase-average and unsteady data. In the wind turbine, together with the traditional near wake, for the first time, the flow was sampled also on a horizontal blade-to-blade plane at midspan. The results of the latter are outstanding to the understanding of this machine aerodynamics, and their success suggests to keep delving into blade-to-blade plane measurements by means of hot wires. An idea, for instance, could be to sample other planes rather than the midspan one, and to use different geometry hot wire probes to improve the flow characterization. The axial turbine campaign, instead, was carried out while the present Thesis was underway. For the first time, the axial turbine stage of the Laboratory of Fluid-Machines of the Energy Department at Politecnico di Milano was tested applying hot wire anemometry. The outcome, made the team aware of the critical issues related to such kind of measurements, and opens the way to further tests and studies on the use of hot wires for high-temperature high-velocity flows investigation.

Keywords: Hot Wire Anemometer, VAWT, Near Wake, Blade-To-Blade Plane, TC Test Rig, Reynolds Stress, Turbulent Integral Lengthscale

Sommario

Il presente lavoro di Tesi tratta l'applicazione dell'anemometria a filo caldo per caratterizzare il flusso a valle di due macchine a fluido tra loro molto diverse: una turbina eolica H ad asse verticale e uno stadio di turbina assiale ad alta pressione. L'obiettivo è comprendere come la stessa tecnica misuristica possa essere usata per lo studio di due scie così distanti, e le criticità che ne possono derivare.

Si è attinto ad un ricco database sperimentale risalente al 2016/17 per mappare il campo di moto della turbina eolica, e con esso la turbolenza, il tensore degli sforzi di Reynolds 2×2 e la scala integrale di turbolenza, sia per i dati medi che per quelli instazionari. Sulla turbina eolica, oltre alla *near wake* convenzionale, è stato campionato per la prima volta anche un piano orizzontale a metà altezza nel piano interpalare. I risultati che ne derivano sono sorprendenti per comprendere l'aerodinamica della macchina, e suggeriscono di approfondire le misure su questo piano. Un'idea potrebbe essere quella di campionare altri piani interpalari diversi da quello a mezza altezza, e di impiegare sonde con altre geometrie per migliorare la caratterizzazione del flusso. La campagna sullo stadio di turbina, invece, è stata portata avanti in parallelo con la presente Tesi. Per la prima volta, lo stadio di turbina del Laboratorio di Fluidodinamica delle Macchine del Dipartimento di Energia del Politecnico di Milano è stato testato con un anemometro a filo caldo. L'esito di questo set di prove ha reso il team consapevole di alcune criticità che questo tipo di misure porta con sé, e apre la strada a nuovi test e ulteriori studi sull'uso dei fili caldi per indagare flussi ad alta temperatura ed alta velocità.

Parole chiave: Anemometro a Filo Caldo, VAWT, *Near Wake*, Piano Interpalare, Banco Prova TC, Tensore di Reynolds, Scala Integrale di Turbolenza

Contents

List of Figures

List of Tables

Introduction

The hot wire anemometer is a miniaturized instrument for velocity measurements working on the principle of heat transfer. It is made of a very thin metal wire, heated up by Joule effect and exposed to a cooling flow. Depending on the cooling potential of the flow in which the wire is immersed, its control unit provides more or less current, to maintain constant the temperature of the sensitive part. The current change can be then related to the velocity of the flow running over the wire by means of the measured output voltage. Thanks to its very high frequency response, the hot wire anemometer is widely used for flow measurements that involve high frequency unsteady phenomena to be detected.

This is the case of the flow downstream of a vertical axis wind turbine (VAWT), a high instability wake whose features cannot be captured by a simple time mean analysis. This kind of machine started thanks to an idea of Darrieus patented in 1931, but it was soon overcome by the horizontal axis wind turbine technology, more efficient on a large scale energy production and characterized by simpler aerodynamics. Nowadays the new concept of energy harvesting is oriented more towards a diffuse production of electricity, in which consumers are also suppliers, and the vice versa. It is hence in the new field of microgeneration in the urban environment, that the vertical axis wind turbine prevails on the horizontal axis configuration. Moreover, the vertical axis technology adapts well to the installation in deep off-shore farms, also known as deepwind. Among the benefits of the VAWT there are its insensitivity to yaw angle, but also gearbox installation at the turbine base, and lower noise due to optimal operation at lower tip-speed ratios. This kind of machine represents thus a promising technology to satisfy the new needs of the energy system, today and in the the future. Nowadays, the development of the vertical axis wind turbine can count on powerful computational methods and advanced aerodynamics studies that allowed to develop more and more sophisticated procedures for the machine optimal design, addressed as vortex models. For this purpose, the fluid-machines scientific community agrees to focus

on the study of the VAWT wake as the effect of the force exchange between wind and blades, in contrast to the streamtube momentum balance models, which are now considered obsolete. For this reason, the studies presented in this Master Thesis work, conducted on the VAWT wake are of truly actual concern, and they mirror the direction in which the research is going, all over the world. The works of Ferreira [1] at TU Delft, and of Lam and Peng [2] at the Hong Kong University, together with the previous studies of the Laboratory fo Fluid Machines (LFM) at Politecnico di Milano carried out in collaboration with the Trento University [3] [4] [5] [6] confirm the global academic feeling upon this topic.

In this work, experimental data on a Darrieus turbine collected during winter 2016/17 in the large scale low-turbulence wind tunnel of Politecnico di Milano have been further elaborated, in order to derive the complete wake flow field, the deterministic unsteadiness, the 2×2 Reynolds stress tensor, and finally the turbulent integral length scale. Only the H-shaped VAWT has been considered, and only in two operating conditions, the optimal and a low loading case. These are identified by a tip-speed ratio (λ), and two kinds of comparisons have been done: first at the same rotational speed and at different tip-speed ratios, and then lower rotational speeds for the same low loading case were compared to evaluate the effect of Reynolds number on similarity. The flow has been characterized on a phase-averaged and, even more important, on an unsteady basis. The latter, in particular, is crucial to detect the vortical structures shed in the wake by dynamic stall. For the first time, in the 2016 campaign, together with the conventional near wake vertical plane, a horizontal measuring grid on the blade-to-blade plane at the machine midspan was sampled. This new idea allows to clearly visualize the vortex shedding and convection along the streamwise direction. For this very important reason, the majority of the data elaboration efforts carried out in this work were focused on the blade-to-blade measurements.

The purpose of the work from the point of view of the wind turbine data was to provide the LFM software written in Fortran 90 with more advanced routines for the calculation of the yaw angle and the 2D Reynolds stress tensor, both phase-averaged and unsteady, together with a third routine for the evaluation of the turbulent integral length scale. These codes, whose algorithms are fully explained in the fifth chapter, have been successfully implemented in the main program, and provided the team with a compete vision of the straight hot wire possibilities for a deep flow characterization. Besides, the work done on the wind data ended up with a wider overview on the criticalities of hot wire measurements during elaboration. The slanted hot wire shall be abandoned for pitch angle

evaluations, and evidence to support this statement is provided in chapter six. On the other hand, the slanted wire may be a good instrument to investigate turbulence, for instance, to pass from a 2D to a 3D Reynolds tensor. The results of hot wire measurements on the vertical axis wind turbine confirm the expected trends on the basis of previous rougher calculations, and show the improvements obtained with the newly implemented routines.

The investigation of the flow downstream of the stator of the axial turbine stage located in the Laboratory of Fluid-Machines of the Energy Department of Politecnico di Milano, was instead carried out in winter 2017/18, while the present Thesis work was underway. The chance for this second part of the work was given by the collaboration with a Ph.D. student from the Von Karman Institute for Fluid-Dynamics. With her and a mechanical engineering student, who was already working on the TC rig with the FRAP probe for her Master Thesis, the stator wake was investigated with a straight hot wire anemometer for the first time. For this very reason, the task was quite challenging, and the hot wire was placed in the gap between stator and rotor, to sample the stator wake, for a start. As a matter of fact, due to its particularly steady state flow, the field downstream of the stator was expected to be a favorable measuring condition compared to the rotor unsteady wake. Up to now, the flow of the axial turbine of the TC test rig has been investigated with the unsteady FRAP probe. The great advantage of the hot wire over the FRAPP, is essentially its geometry, that allows to get closer to the hub along the radial position, and hence to map the hub structures, which are quite relevant and interesting to see. Besides, since the hot wire can provide more accurate results on turbulence compared to the FRAPP, it would be useful to have an alternative probe to support the FRAPP on turbulence measurements. The experimental campaign carried out on the high-pressure turbine stage with the anemometer, wanted hence to be the starting point for further investigations in the application of this kind of probe in such a facility, in the perspective of increasing the experience of the team with hot wires in diverse applications. For this purpose, the present Thesis work was engaged in this new experimental campaign, and it became the chance to observe the behavior of the instrument in two different applications.

In this case, only the time mean data were elaborated, as downstream of the stator periodic unsteadiness is particularly weak, since related only to the rotor pressure field that propagates upstream, in the gap between the two cascades. The first results to be investigated were the velocity field and the yaw angle, and to this purpose, the same routines of the

wind data were implemented for this new domain. During these tests, several issues arose, among which the most evident are for sure the dependency of the probe calibration parameters on temperature and the zero capturing procedure. All these criticalities are then presented in detail in the appendix, since they are considered an important background for future investigations. With the idea to have the hot wire as alternative probe to the FRAPP for flow characterization in the TC rig, the tests of winter 2017/18 discussed in this Thesis, and most of all the uncertainties come to light, open the way to further tests and studies on the applicability of hot wires to high-velocity high-temperature flows. On the other hand, the results obtained for turbulence are much more reliable. These data will be then presented in the results discussion chapter.

The present Thesis work is organized in six chapters, in which the most important steps of the experimental investigation, the elaboration algorithms and the results presentation are discussed in detail. In the next lines the outline of the work is presented:

1. The first chapter gives a rapid overview of the theoretical background regarding turbulence statistics.

2. The second chapter as well is mostly theoretical, but it specifically concerns the hot wire probe, its working principle and governing equations, and the electronic circuit.

3. The third chapter goes in the details of calibration and how it has been done in practice on the LFM nozzle.

4. In chapter four, the experimental apparatus is described, and its technical characteristics are presented.

5. The fifth chapter represents the core of the whole work, since it reports all the data processing algorithms implemented in the LFM software, that allow to pass from a raw voltage measurement to several flow properties of interest.

6. In the sixth chapter, the results discussion is carried out, for both experimental campaigns.

7. Finally, the conclusions of the work are drawn and some future developments are proposed.

Chapter 1

Turbulence

The present work discusses flow measurements downstream of two different kinds of machines: an axial-flow turbine stage (GT) in the axial gap between the stator trailing edge and the rotor leading edge, and an H-shaped vertical axis wind turbine (VAWT). More precisely, the present work focuses mainly on the unsteady characterization of the wake of these machines, in terms of velocity magnitude, flow angles and turbulence. Between the two machines, a deeper insight is given in the VAWT investigation, since it is the one characterized by the stronger unsteady phenomena, still largely unexplored and for this reason more interesting. In this chapter, a brief argumentation on unsteady flow phenomena and turbulence is given.

In this section, an introduction on turbulent flows is carried out, with the purpose of recalling the basic concepts necessary for the experimental investigation on turbulence that is developed in the next chapters.

1.1 General Concepts

In nature as in engineering applications, the vast majority of flows is turbulent, and so are the wakes considered in the present Thesis work. Turbulence is a particularly complex problem, to which there is generally no analytical solution, but studies are mainly based on experiments, computational methods and dimensional reasonings. Despite the common way of thinking, giving a definition of turbulence is rather complex, but there are some main intuitive characteristics that can distinguish a turbulent flow:

- Randomness: Fluid particles in a turbulent flow move irregularly, in a seemingly chaotic way.

- Non-linearity: The non-linearity of turbulent flows exhibits in two other phenomena. The first is the existence of a dimensionless parameter such as the Reynolds number, that when exceeding a certain threshold gives rise to instability. The other issue of non-linearity of the turbulent flows is the vortex stretching phenomenon.

- Diffusivity: Thanks to its macroscopic mixing due to vortices, turbulent flows ensure a high diffusivity of mass, energy and momentum.

- Vorticity: Vortices, also called *eddies*, are the most characteristic features of turbulent flows, and they can be of many several sizes, as discussed in the next lines. These eddies are continuously stretching, spinning, splitting and combining. These vortices act as energy vectors, and transfer energy from the bulk flow to the dissipation ranges, by means of the energy cascade process, described later.

- Dissipation: Turbulent flows are also rather dissipative. There is in action a continuous transfer of energy from the largest to the smallest scales, where dissipation takes place, and a continuous energy supply is required to support this process.

It is possible to distinguish between two main kinds of turbulent flows:

- Wall-Free Shear flows: Flows not bounded by any solid interface. Here turbulence is mainly due to friction between fluid layers with a particularly steep velocity gradient. It is the case of jets, shear layers and wakes, as the case under consideration.

- Wall-Bounded Shear flows: Flows limited by a solid surface. It is the case of boundary layers.

1.2 Averages

By its very nature, as discussed in the previous section, turbulence appears as a random phenomenon, and as a consequence it is impossible to find an analytical equation able to describe a turbulent flow in space and time in a deterministic way. Hence, the only quantitative way to describe turbulence is through a statistical approach. A first step is to separate the random component of velocity from its average. This is called *Reynolds decomposition* and it can be expressed this way:

$$U = \overline{u} + u' \tag{1.1}$$

Where U is the instantaneous time-dependent velocity magnitude, $\overline{u}$ is its average and u' the random fluctuation around such average. Anyway, the concept of "average" is not so trivial, and there are two possible averages that are computed in turbulent flows. The most basic one that can be conceived is the *time average*:

$$\overline{u} = \lim_{t_0 \to 0} \frac{1}{t_0} \int_0^{t_0} U(t) dt \tag{1.2}$$

This very intuitive way to compute the average can be representative of a flow field only for steady state conditions, in which velocity oscillates around an average that is constant in time. With reference to the subject of this work, this is for instance the case of the flow downstream of the axial-flow turbine stator. Downstream of a rotor, such as the VAWT wake, instead, the flow is not steady, but suffers periodic oscillations. This means that in these kinds of flow, there is a velocity component that is not stochastic, but deterministic, because it is related to the periodic passage of the rotor blade, which is a matter of fact. Thus, in this case, a simple time average is not enough to capture the flow randomness. The correct way to proceed is instead to compute an *ensemble average*. This is a time-dependent average that is used to characterize sets of experimental data recorded a certain number of times (N) in the same conditions. Considering for instance the case of the VAWT reported in this work, it is reasonable to think that the wake during a blade passing period exhibits the same features of the previous and of the following period, since every period is characterized by the same boundary conditions which are repeated N times during the sampling interval. In this context, a blade passing period can be then considered an *ensemble*, and the most representative way to compute an average field is to combine the records acquired at the same position within such period. Addressing as $U_i(t)$ the instantaneous velocity belonging to the i-th ensemble, the average is defined as:

$$\overline{u}(t) = \frac{1}{N} \sum_{i=1}^{N} U_i(t) \tag{1.3}$$

The ensemble average can be also seen as the sum of a time mean term, and a zero average periodic deterministic component. In case such a component is combined to turbulence, it is possible to apply the so-called triple decomposition, and this is the precise concept that will be applied to the VAWT turbulent wake.

$$U = (U_{TM} + U_{PER}) + u' \tag{1.4}$$

The triple decomposition is represented in Fig.1.1, where the time mean, periodic and fluctuating velocities are plotted together.

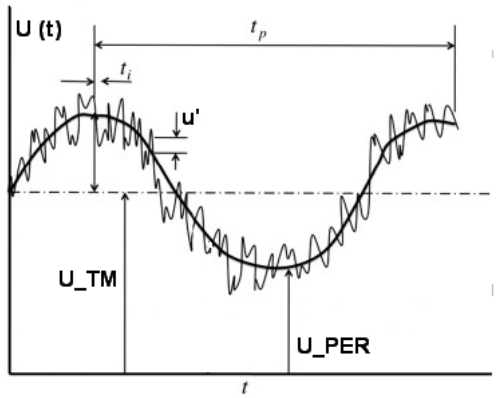

Figure 1.1: Ensemble averaging for an unsteady flow.

The resulting turbulence is then a random fluctuating signal $u'(t)$ with zero average, from which it is possible to define a *turbulence intensity* based on further statistics. One of the most significant statistics that provides a measurement of how wide are the fluctuations around the average, and hence of the flow randomness, is the variance of the $u'(t)$ signal, or alternatively its standard deviation, which is also called *root-mean-square (RMS)*. This is defined as:

$$U_{variance} = \overline{(u')^2} \tag{1.5}$$

$$U_{RMS} = \sqrt{U_{variance}} = \left(\overline{(u')^2}\right)^{0.5} = \left(\overline{\left(U - (U_{TM} + U_{PER})\right)^2}\right)^{0.5} \tag{1.6}$$

On the basis of this concept, turbulence intensity will be defined normalized with respect to the incoming flow velocity, and usually given in percentage:

$$I_{TU} = \frac{U_{RMS}}{U_0} \times 100 \tag{1.7}$$

1.3 Autocorrelation and Integral Time Scale

When studying turbulence, it is interesting to investigate the memory of the flow, as to say, for how long the consequences of a perturbation last. This problem is solved by the so called *eulerian autocorrelation coefficient*,

which is a measure of the "degree" of correlation of a homogeneous flow with itself, and it is defined as:

$$R_E(t_1, t_2) = \overline{u'(t_1)u'(t_2)} \tag{1.8}$$

The homogeneity hypothesis is required in order to eliminate the space dependence, but this definition can be applied even if the flow is not properly homogeneous. As a matter of fact, when dealing with experimental data, a certain spatial discretization is always defined, and it is then sufficient to limit the homogeneity hypothesis in a neighborhood of the measuring point, applying then eq.1.8 for every step of the measuring grid. Usually, it is preferable to write the autocorrelation as a function of one single variable (τ), which is the time lag from a generic reference time (t). Besides, it is also useful to normalize the autocorrelation, and for this purpose the average turbulent kinetic energy is a good choice, which is nothing but the velocity fluctuations variance. Hence, eq. 1.8 is rewritten as:

$$r_E(\tau) = \frac{\overline{u'(t)u'(t+\tau)}}{\overline{u'^2}} \tag{1.9}$$

By definition, the moment in which the flow is most strongly correlated with itself is for $\tau = 0$, and for this case $r_E(\tau = 0) = 1$, which must be the maximum of the autocorrelation function. Then, as time passes and the lag increases, the flow loses memory and the correlation reduces. Hence, the autocorrelation decreases, until it reaches zero when the flow is no longer correlated with itself. This means that it is valid the condition:

$$r_E(\tau) \leq 1 \tag{1.10}$$

If the flow is steady, the autocorrelation function should go monotonically to zero and remain zero up to infinity, as shown in Fig. 1.2. In real flows, instead, especially in the VAWT unsteady wake, it is pretty common to find periodicity, and this means that after a while, the autocorrelation, instead of remaining zero, will start to fluctuate more or less periodically around the zero value. It is furthermore possible to give an indication of how long the flow can be considered highly correlated with itself. This is represented by the *integral time scale*, defined as:

$$T_E = \int_0^\infty r_E(\tau)d\tau \tag{1.11}$$

The upper extreme of the integration interval is infinity only in the non-periodicity case, but in a real case, where periodicity arises, the integral

should be computed up to the point at which the autocorrelation goes to zero. The rest of the domain can be then forgotten.

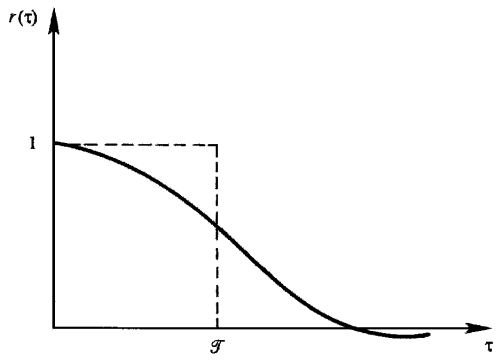

Figure 1.2: Autocorrelation funciton and integral time scale.

As it is defined, the integral time scale represents the memory of the process and hence the duration time of the largest vortical structures present in the flow.

A further step is then represented by the concept of *energy spectrum*, which is the distribution of energy in the frequency domain. Given the autocorrelation as a function of the time lag, it is possible to pass form the time to the frequency domain by means of a Fourier transform. Hence, let us call $E(f)$ the Fourier transform of the autocorrelation function:

$$E(f) = \frac{1}{2\pi} \int_{-\infty}^{\infty} e^{-i2\pi f\tau} R_E(\tau) d\tau \tag{1.12}$$

$$R_E(\tau) = 2\pi \int_{-\infty}^{\infty} e^{i2\pi f\tau} E(f) df \tag{1.13}$$

It is then possible to demonstrate that $R_E(\tau)$ and $E(f)$ represent a Fourier transform pair, and this holds true anytime the autocorrelation decays to zero rapidly enough. It is also possible to show that if $R_E(\tau)$ is real and symmetric, as it is for a non-periodic flow, then also its Fourier transform is real and symmetric. Thus replacing $\tau = 0$ in eq. 1.13:

$$\overline{u'^2} = 2\pi \int_{-\infty}^{\infty} E(f) df \tag{1.14}$$

From eq. 1.14, it is easy to deduce that the $E(f)$, Fourier transform of the autocorrelation function, represent the energy distribution on the frequency domain, and hence this is defined as the energy spectrum $E(f)$.

Finally, it is possible to compute an approximation of the turbulent integral length scale starting from the time scale value, by means of the Taylor's hypothesis, which states that the turbulent eddies passing through a measuring point can be considered frozen as they advect past the probe, and hence there is no local change within the eddy.

$$X_E[m] = T_E[s] \times \overline{u} \tag{1.15}$$

This integral length scale is hence an estimate of the dimension of the largest eddies present in the wake.

1.4 Averaged Equations of Motion

When studying a turbulent flow, it is impossible in practice to solve the problem for the whole scales of space and time, since the spectrum is pretty wide, and it would take a huge computational effort to resolve the Navier-Stokes equations for an ordinary turbulent flow problem in these conditions. Nevertheless, it is not so relevant for common engineering purposes to go so deeply in the detail of a turbulent flow, while it is usually more interesting to derive the average temperature and velocity field. Hence, for this purpose, the Reynolds decomposition discussed in sec.1.2 is applied to the instantaneous equations of mass, momentum and energy. The purpose of this argumentation is then to investigate the consequences that the turbulent fluctuations shall have on the main flow.

In this section, for sake of simplicity, the instantaneous quantities will be addressed with a tilde, the average will be written in capital letters, and the fluctuations in lowercase ones. Hence, the Reynolds decomposition for velocity will be for instance:

$$\widetilde{U} = U + u$$

The only exception will be temperature. In order to avoid misunderstanding with the time variable, the average temperature is $\overline{T}$, and the fluctuation is T'. For an incompressible steady state flow, the continuity equation decomposed by Reynolds is:

$$\frac{\partial \widetilde{U}_i}{\partial x_i} = \frac{\partial}{\partial x_i}(U_i + u_i) = 0 \tag{1.16}$$

Computing the average of eq. 1.16, the result is the following:

$$\overline{\frac{\partial}{\partial x_i}(U_i + u_i)} = \frac{\partial U_i}{\partial x_i} + \overline{\frac{\partial u_i}{\partial x_i}} = \frac{\partial U_i}{\partial x_i} + \frac{\partial \overline{u_i}}{\partial x_i} = 0 \tag{1.17}$$

The continuity equation for the mean flow states that:

$$\frac{\partial U_i}{\partial x_i} = 0 \tag{1.18}$$

Substituting eq. 1.18 in eq. 1.17 it is straight-forward that:

$$\frac{\partial u_i}{\partial x_i} = 0 \tag{1.19}$$

Eq. 1.19 represents the continuity equation relatively to the fluctuating velocity field. This means that continuity equation applies also to the fluctuating velocity, together with the main flow. All the instantaneous, the average and the fluctuating velocity terms are non divergent. This is an interesting result, that will be used for the following argumentations as well.

The momentum equation, instead, written under the Boussinesq approximation, states that:

$$\frac{\partial \widetilde{U}_i}{\partial t} + \widetilde{U_j}\frac{\partial \widetilde{U}_i}{\partial x_j} = -\frac{1}{\rho_0}\frac{\partial \widetilde{p}}{\partial x_i} - g[1-\alpha(\widetilde{T}-T_0)]\delta_{i3} + \nu\frac{\partial^2 \widetilde{U}_j}{\partial^2 x_j} \tag{1.20}$$

Written with the Reynolds decomposition, eq. 1.20 becomes:

$$\begin{aligned}\frac{\partial}{\partial t}(U_i+u_i) + (U_j+u_j)\frac{\partial}{\partial x_j}(U_i+u_i) = \\ = -\frac{1}{\rho_0}\frac{\partial}{\partial x_i}(P+p) - g[1-\alpha(\overline{T}+T'-T_0)]\delta_{i3} + \nu\frac{\partial^2}{\partial x_j^2}(U_i+u_i)\end{aligned} \tag{1.21}$$

To simplify the notation, the average of each term of eq. 1.21 will be reported separately. The time derivative term is:

$$\overline{\frac{\partial}{\partial t}(U_i+u_i)} = \frac{\partial U_i}{\partial t} + \overline{\frac{\partial u_i}{\partial t}} = \frac{\partial U_i}{\partial t} + \cancelto{0}{\frac{\partial \overline{u}_i}{\partial t}} = \frac{\partial U_i}{\partial t} \tag{1.22}$$

The average of the advective term, thanks to the results on continuity, becomes:

$$\begin{aligned}\overline{(U_j+u_j)\frac{\partial}{\partial x_j}(U_i+u_i)} &= U_j\frac{\partial U_i}{\partial x_j} + U_j\cancelto{0}{\frac{\partial \overline{u}_i}{\partial x_j}} + \overline{u}_j\frac{\partial U_i}{\partial x_j} + \overline{u_j\frac{\partial u_i}{\partial x_j}} = \\ &= U_j\frac{\partial U_i}{\partial x_j} + \frac{\partial}{\partial x_j}(\overline{u_i u_j})\end{aligned} \tag{1.23}$$

Furthermore, the average of the pressure gradient can be computed as well, and it is:

$$\overline{\frac{\partial}{\partial x_i}(P+p)} = \frac{\partial P}{\partial x_i} + \cancelto{0}{\frac{\partial \overline{p}}{\partial x_i}} = \frac{\partial P}{\partial x_i} \tag{1.24}$$

Then, the average of the gravity term coming from the Boussinesq approximation is evaluated considering that the average of the temperature fluctuation is zero, and the result is:

$$\overline{g[1-\alpha(\overline{T}+T'-T_0)]} = g[1-\alpha(\overline{T}-T_0)] \tag{1.25}$$

Finally, the average of the viscous term is:

$$\overline{\nu\frac{\partial^2}{\partial x_j^2}(U_i+u_i)} = \nu\frac{\partial^2 U_i}{\partial x_j^2} \tag{1.26}$$

In the end, the final step is to collect all the average terms to obtain the average momentum equation for the Reynolds decomposition.

$$\frac{\partial U_i}{\partial t} + U_j\frac{\partial U_i}{\partial x_j} + \frac{\partial}{\partial x_j}(\overline{u_i u_j}) = -\frac{1}{\rho_0}\frac{\partial P}{\partial x_i} - g[1-\alpha(\overline{T}-T_0)]\delta_{i3} + \nu\frac{\partial^2 U_i}{\partial x_j^2} \tag{1.27}$$

Looking at eq. 1.27, it is interesting to note that together with all the average terms, resembling those of eq. 1.20, there is one more term, that is made only by the velocity fluctuations $\overline{u_i u_j}$. This term can be interpreted in many ways, but it is usually defined as the *Reynolds stress*. Looking at the equations of motion in the three directions of space, the notation used in the previous equations suggests that $\overline{u_i u_j}$ actually refers to a symmetrical matrix. Let us write the $\overline{u_i u_j}$ term on the right-hand side of eq. 1.27, and gather the remaining terms in the material derivative notation:

$$\frac{DU_i}{Dt} = -\frac{1}{\rho_0}\frac{\partial P}{\partial x_i} - g[1-\alpha(\overline{T}-T_0)]\delta_{i3} + \frac{\partial}{\partial x_j}\left[\nu\frac{\partial U_i}{\partial x_j} - \overline{u_i u_j}\right] \tag{1.28}$$

The same equation can be then rewritten as:

$$\frac{DU_i}{Dt} = \frac{1}{\rho_0}\frac{\partial \overline{\tau}_{ij}}{\partial x_j} - g[1-\alpha(\overline{T}-T_0)]\delta_{i3} \tag{1.29}$$

Where inside the $\overline{\tau}_{ij}$ term, the following has been gathered:

$$\overline{\tau}_{ij} = -P\delta_{ij} + \mu\left(\frac{\partial U_i}{\partial x_j} + \frac{\partial U_j}{\partial x_i}\right) - \rho_0\overline{u_i u_j} \tag{1.30}$$

Cmparing then equations 1.29 and 1.30, with those written for the instantaneous flow quantities:

$$\frac{D\widetilde{U}_i}{Dt} = \frac{1}{\rho_0}\frac{\partial \overline{\tau}_{ij}}{\partial x_j} - g[1 - \alpha(\widetilde{T} - T_0)]\delta_{i3} \tag{1.31}$$

$$\overline{\tau}_{ij} = -\widetilde{p}\delta_{ij} + \mu\left(\frac{\partial \widetilde{U}_i}{\partial x_j} + \frac{\partial \widetilde{U}_j}{\partial x_i}\right) - \rho_0\overline{u_i u_j} \tag{1.32}$$

The term $-\rho_0\overline{u_i u_j}$ can be regarded as an additional stress that is applied to the mean flow, due to the action if the turbulent velocity fluctuations. Notice that such stresses coming up on the main flow field, are actually much larger than the viscous contributions, represented by the μ term, except for regions close to solid walls, where the fluctuations are small, while the mean flow gradients are high. Writing the additional stress in a matrix notation, the result is the so called *Reynolds stress tensor*, which is a 3×3 symmetric matrix.

$$-\rho_0 \begin{bmatrix} \overline{u_1^2} & \overline{u_1 u_2} & \overline{u_1 u_3} \\ \overline{u_2 u_1} & \overline{u_2^2} & \overline{u_2 u_3} \\ \overline{u_3 u_1} & \overline{u_3 u_2} & \overline{u_3^2} \end{bmatrix}$$

Where the subscripts indicate the three spatial directions. As any stress tensor, the diagonal components describe the normal stresses, while the off-diagonal ones are the shear stresses applied to a fluid element. At this point of the argumentation, it is interesting to introduce the concept of isotropic and anisotropic turbulence, represented graphically in Fig. 1.3.

- Isotropic: Turbulence is said to be isotropic when there is no preferential direction of the velocity fluctuations. Alternatively, when the velocity fluctuations in a certain direction are not correlated with those along any other direction, which means $\overline{u_i u_j} = 0$ with $i \neq j$, and at the same time the diagonal components are equal one to another ($u_1^2 = u_2^2 = u_3^2$). The physical interpretation is that there are no shear stresses in the flow, and hence no vortex stretching. From this brief discussion, it is evident that perfectly isotropic turbulence is a purely theoretical concept, because without vortex stretching there is no energy cascade, which means that dissipation cannot be supported.

- Anisotropic: Turbulence is said to be anisotropic when the flow field has a certain polarity, and there can be identified a certain correlation between fluctuations of different velocity components. If $\overline{u_i u_j} < 0$ with $i \neq j$, positive velocity fluctuations along i are likely associated to negative fluctuations along j. This is generally what is expected in a turbulent flow [8].

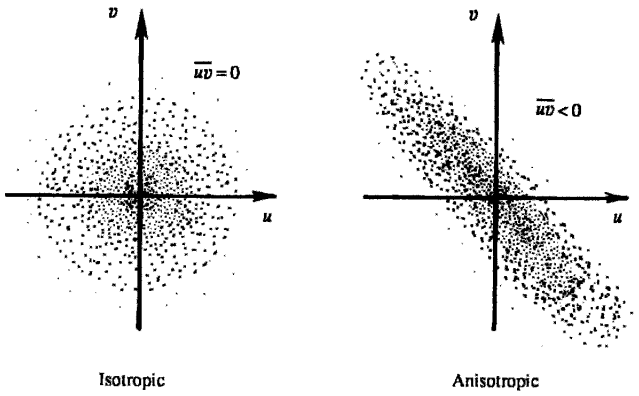

Figure 1.3: Graphical distinction between isotropic and anisotropic turbulence on a scatter plot.

Alternatively, the components of the Reynolds stress tensor may be interpreted as the rate of momentum transfer by means of turbulent fluctuations. For instance, considering a generic shear flow (u_1, u_2, u_3) and its turbulent fluctuations, the instantaneous rate of x_1 momentum along the x_2 direction is:

$$\rho_0 \overline{(U_1 + u_1)u_2} = \rho_0 U_1 \overline{u_2} + \rho_0 \overline{u_1 u_2} = \rho_0 \overline{u_1 u_2} \tag{1.33}$$

Finally, it is possible to generalize the concept of Reynolds stress, and see it as the average flux of the i-momentum along the j-direction, which is equal to the j-momentum along the i-direction.

1.5 Energy Cascade

In the history of the studies on turbulent phenomena, a very important work was carried out by Lewis Richardson in 1922, a British meteorologist who proposed that in turbulent flows the kinetic energy is transferred from large to gradually smaller eddies, until it is dissipated by viscosity. This phenomenon is called *energy cascade*, and it is still today at the basis of the current understanding of turbulence. This theory suggests that

the dimension of the largest eddies is of the same order of magnitude of the main shear flow and these subtract kinetic energy to the bulk flow by means of vortex stretching. Then, smaller eddies get strained by the larger ones, and by means of the same vortex stretching phenomenon, they extract energy from the larger structures. This energy transfer process goes on to smaller and smaller eddies until energy is finally dissipated by viscous forces. Hence, this is a proper cascade process, and this way energy gets transferred from the bulk flow to the dissipation scale. Dissipation finally takes place when viscosity is able to overcome inertia forces, and this shall occur when Reynolds number is close to unity. The dissipation scale represents then the dimension of the smallest eddies, which are in the end smeared out and their kinetic energy contributes to increase the thermal energy of the flow. The fluid viscosity does not affect the energy cascade process, since vortex stretching arises from the nonlinear terms of the equations of motion, and this process is hence inviscid. Nevertheless, viscosity does affect the scale at which the smallest eddies are definitely smeared out. This scale is therefore called the *Kolmogorov microscale* and indicated with the Greek letter μ. The phenomenon should look like the one proposed in Fig. 1.4.

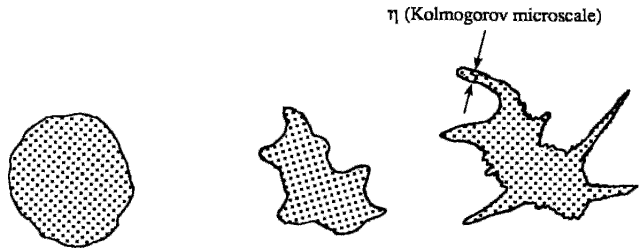

Figure 1.4: Three sequential frames representing the vortex stretching of a fluid particle.

Chapter 2

The Probe

The hot wire anemometer (HW) is a highly miniaturized instrument for velocity measurements in fluids, both gases and liquids. It works on the principle of heat transfer, which of course depends on the fluid velocity magnitude and direction. The instrument is made of a sensitive part, which is the wire itself heated up by Joule effect and exposed to the cooling flow, the mechanical support, and control electronics which is also able to convert the output of the probe in a voltage signal. The HW anemometer, thanks to its very small dimension, is a particularly adequate probe when measuring turbulent phenomena and turbulent fluctuations in space and time, and this happens for three fundamental reasons:

- A small probe can measure the flow properties with little perturbations of the velocity field.
- The smaller the probe, the smaller the spatial measurement uncertainty, such that the probe output as punctual can be considered punctual.
- Since the HW measurement is based on heat transfer, the smaller the sensitive part, the smaller its thermal inertia and the higher the frequency response of the instrument itself.

Furthermore, thanks to its particular accuracy in turbulence measurements, it is a valid term of comparison for the validation of the results produced by other probes, such as the Fast-Response Aerodynamic Pressure Probe (FRAPP). In the following chapter provides a description of the instrument, its working principle, the possible configurations of its electric circuit, its sensitivity to the flow direction, and the issues that can lead to its failure.

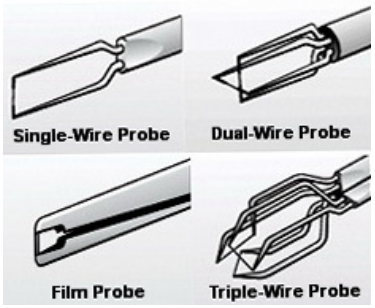

Figure 2.1: Examples of Hot Wires

2.1 Probe description

Many kinds of probes are available, depending on the application, some of the most widely used sensors are shown in Fig.2.1. For instance, one of the simplest probes is the single wire one, but double or triple wire sensors are also available, to improve the sensitivity of the instrument in the three spatial directions. For boundary layer measurements, instead, specific probes can be employed with a curved stem of 45° or 90°, in order to reduce the flow disturbance close to the wall. Furthermore, film probes can be used instead of wire ones, where the sensitive element is a metal film deposition.

For the experimental campaign carried out in the wind tunnel il 2016, the Dantec Dynamics' 55P11 and 55P12 probes were used, whose sensitive element is made of a platinum-rhodium wire 1.25 mm long and with a diameter of 5 μm. On the market are also available wires up to 1 μm of diameter for special applications, and generally in between $0.4 \div 2.2$ mm long. The two aforementioned probes are the followings:

- Straight probe (55P11). The wire is perpendicular with respect to the probe stem, which means that the needles that hold the wire are of the same length. This configuration will be considered as the reference for zero-inclination ($\alpha = 0°$).

- Slanted probe (55P12). The wire is inclined with respect to the 0° position of $\alpha = 45°$. This particular shape allows the sensor to have a higher sensitivity in the third dimension in space.

During the latest experimental campaign (Dec. 2017 - Jan. 2018) downstream of the stator of an axial-flow turbine stage, instead, only the straight probe was used, since it was considered more reliable than the slanted one, and the radial component of velocity is not of particular

interest, as it is was already known to be very small, from previous measurement campaigns with other techniques. These probes were chosen for the following reasons:

- Possibility to combine the results of the two probes for the VAWT case, obtaining the whole velocity field and the Reynolds' stress tensor.
- Smaller dimensions of the probe compared to the multi-wire ones, which means lower error while considering the measurements as punctual.
- Lower cost of the probes, the electronics and of the acquisition system of the single-wire probe compared to the multi-wire one.

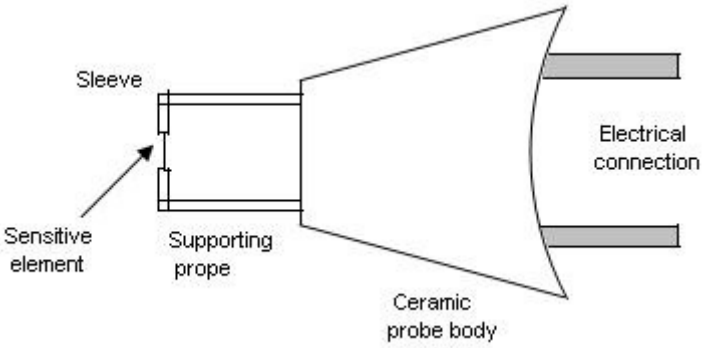

Figure 2.2: Hot Wire Structure

The probe has the structure shown in Fig.2.2. Two inox steel cylindrical prongs are enclosed in a ceramic body of a proper aerodynamic shape, that protects the connection to the electrical circuit. On their outer side, the prongs take the shape of two sleeves on which the sensitive element wire is welded, while on the inner part, the electrical connection is enhanced by means of golden elements. The electrical circuit, instead, has the structure of a Wheatstone Bridge, whose arrangement depends on whether a Constant Temperature (CT) or Constant Current (CC) configuration is chosen.

2.2 Working Principle

As mentioned at the beginning, the working principle of the HW is heat transfer that takes place between the wire heated by Joule effect,

and the flow in which it is immersed, which depends of course on the relative velocity felt by the wire itself, in terms of magnitude and direction. Hence, it is possible to write a relationship between the flow velocity and the voltage that supplies the instrument.

2.2.1 Energy Balance on the Probe

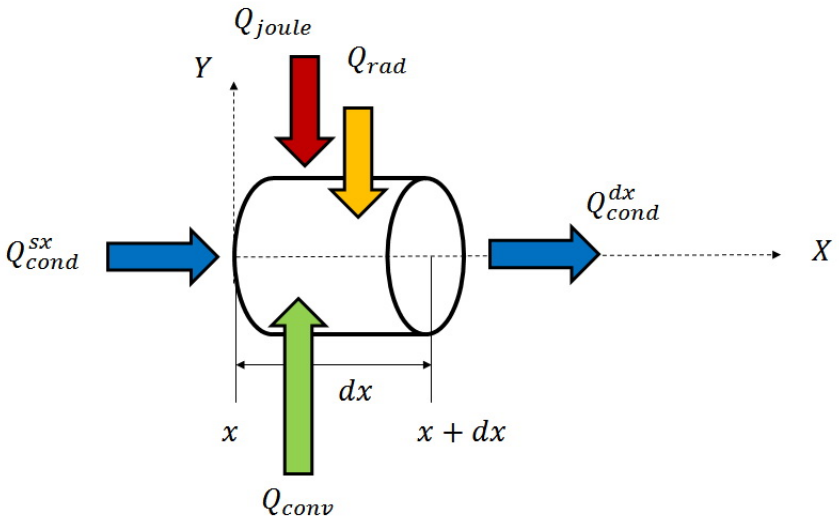

Figure 2.3: Energy balance on the hot wire

The energy balance on the hot wire is described by the scheme shown in Fig.2.3, and it includes the following terms:

- Heat transfer by forced convection, with the flow running over the sensitive element is the main heat transfer mechanism involved.
- Heat transfer by conduction through the metal prongs cannot be neglected for the aspect ratio of the considered probe.
- Heat transfer by natural convection and by radiation are usually neglected.
- Energy is stored inside the wire. Even if the wire has a very small mass, this effect cannot be neglected because it strongly influences the frequency response of the instrument in constant current configuration, making it unsuitable for turbulence measurements.

As explained in Fig.2.3, the energy balance is carried out on an infinitesimal element of length dx, diameter D, cross section A and total length l. Thermal energy is generated inside the infinitesimal control volume, a portion is discharged by thermal interaction with the surroundings, while the rest is stored inside the wire itself. The balance is written in its general form in eq. 2.1.

$$Q_{joule} + Q_{cond}^{sx} + Q_{cond}^{dx} + Q_{conv} + Q_{rad} = Q_{store} \tag{2.1}$$

Where the terms of the equation can be expanded as follows from left to right.

- Energy generated inside the element by Joule effect, due to the passage of an electric current.

  $$Q_{joule} = \frac{I^2 \rho_w}{A}\ dx$$

  Where I is the current intensity passing through the wire and ρ_w is its resistivity.

- Energy transferred by thermal conduction from the left-hand side of the control volume at coordinate x.

  $$Q_{cond}^{sx} = -k_w A \frac{\partial T_w}{\partial x}\bigg|_x$$

  Which is nothing but the Fourier's law, where k_w is the thermal conduction of the wire.

- Energy transferred by thermal conduction from the right-hand side of the control volume at coordinate $x + dx$.

  $$Q_{cond}^{dx} = +k_w A \frac{\partial T_w}{\partial x}\bigg|_{x+dx}$$

  This equation is analogous to the one for Q_{cond}^{sx}, but evaluated at another x coordinate. Rewriting it in a Taylor's expansion:

  $$Q_{cond}^{dx} = +k_w A \frac{\partial T_w}{\partial x}\bigg|_x + A\frac{\partial}{\partial x}\left(k_w \frac{\partial T_w}{\partial x}\bigg|_x\right) dx$$

- Energy transferred to the cooling flow by forced convection. As mentioned before, natural convection is neglected when forced convection is present.

  $$\begin{aligned} Q_{conv} &= Q_{conv}^{forced} + \cancel{Q_{conv}^{nat}} = -hS_{lat}(T_w - T_f) \\ &= -h\pi D(T_w - T_f)\ dx \end{aligned}$$

Where the surface interested by the phenomenon is the lateral surface of a cylinder of diameter D and infinitesimal length dx, which is $S_{lat} = \pi D dx$. The characteristic temperature difference is the one between the wire and the flow $(T_w - T_f)$, and h is the convective heat transfer coefficient that characterizes the problem.

- Energy transferred by radiation from the environment.

$$\begin{aligned} Q_{rad} &= -S_{lat}\sigma\varepsilon(T_w^4 - T_{amb}^4) \\ &= -\pi D\sigma\varepsilon(T_w^4 - T_{amb}^4)\ dx \end{aligned}$$

Where σ is the Stefan-Boltzmann constant and ε is the emissivity of the material.

- Energy stored inside the control volume.

$$Q_{store} = \rho c A \frac{\partial T_w}{\partial t}\ dx$$

Where ρ is the density and c is the specific heat of the material of which the wire is composed. The time coordinate, instead, is indicated with t.

The thermal balance can be rewritten with all the single terms made explicit, and the result is in eq. 2.2

$$\begin{aligned} \frac{I^2\rho_w}{A}\ dx\ +\ A\frac{\partial}{\partial x}\left(k_w\frac{\partial T_w}{\partial x}\right) dx\ -\ h\pi D(T_w - T_f)\ dx\ + \\ -\ \pi D\sigma\varepsilon(T_w^4 - T_{amb}^4)\ dx = \rho c A\frac{\partial T_w}{\partial t}\ dx \end{aligned} \tag{2.2}$$

The energy balance so expressed is in the form of a partial differential equation that could be solved in order to obtain the temperature profile inside the hot wire along the x coordinate. It is evident that eq. 2.2 is also time-dependent, which is necessarily an issue when evaluating the frequency response of the probe. Nevertheless, it is not in the purpose of this work to go in the detail of such analysis, but it is preferable to solve the equation under the following hypotheses:

- Steady state conditions: $\frac{\partial}{\partial t} = 0$
- Negligible heat transfer by radiation: $Q_{rad} \rightarrow\ 0$

- Homogeneous wire with thermal conductivity not depending on its temperature

And eq. 2.2 can be written in a simplified way as follows, where the coordinate system has $x = 0$ at the wire mid-length

$$\frac{I^2 \rho_w}{A} + A k_w \frac{\partial^2 T_w}{\partial x^2} - h\pi D(T_w - T_f) = 0 \tag{2.3}$$

It also possible to define:

- $\vartheta = T_w - T_f$
- $K_1 = \frac{\alpha I^2 R_o - \pi D h l}{A k_w l}$
- $K_2 = -\frac{I^2 R_f}{A k_w l}$

Eq. 2.3 becomes then:

$$\frac{d^2\vartheta}{dx^2} + K_1 \vartheta = K_2 \tag{2.4}$$

When solved, the differential equation written above expresses the temperature profile inside the wire. Nevertheless, to close the problem, a set of proper boundary conditions is required, which are:

- The problem is symmetric, and hence the center of the wire corresponds to a stationary point in the equation of the temperature profile. In particular, since the wire is being cooled down, at its mid-length, such stationary point corresponds to a maximum in temperature.

$$\left.\frac{d\vartheta}{dx}\right|_{x=0} = 0$$

- The metal support at the wire extremities can be considered in thermal equilibrium with the external fluid, thanks to its small dimension. Hence, both supports will have the same temperature as the cooling flow.

$$T_w\left(x = \pm\frac{l}{2}\right) = T_f \quad \Rightarrow \quad \vartheta\left(x = \pm\frac{l}{2}\right) = 0$$

Finally, a solution to the problem is obtained, and the temperature profile inside the wire is:

$$T_w = \frac{K_2}{|K_1|}\left[\frac{\cosh(\sqrt{|K_1|}x)}{\cosh(\sqrt{|K_1|}\frac{l}{2})} - 1\right] + T_f \tag{2.5}$$

Nevertheless, the interest of the experimentalist is usually focused on the mean value of the temperature along the wire, which is computed as the integral of the profile over the wire length divided by the length itself.

$$\overline{T}_w = \frac{1}{l}\int_{-\frac{l}{2}}^{\frac{l}{2}} T_w dx = \frac{K_2}{K_1}\left[\frac{\tanh(\sqrt{|K_1|}\frac{l}{2})}{\sqrt{|K_1|}\frac{l}{2}} - 1\right] + T_f \tag{2.6}$$

Hence, once it is possible to calculate the constants K_1 and K_2, the average temperature of the sensor can be computed.

2.2.2 Heat Transfer Laws

In literature there are several laws describing heat transfer in the HW anemometer, and these allow to determine the flow properties of interest, such as the velocity magnitude first. As previously described, the anemometer exchanges heat with the flow by conduction, forced and natural convection, and radiation. With a good approximation, natural convection and radiation can be neglected. Furthermore, with a second rougher approximation, it is possible to neglect also thermal conduction, and this means that in steady state conditions the heat produced in the wire by Joule effect has to be completely discharged to the cooling flow by forced convection.

$$Heat\ Supply = I^2 R_w = \pi D l h (T_w - T_f) = Heat\ Dissipation \tag{2.7}$$

To be precise, the temperature is not homogeneous inside the wire. As it has been previously demonstrated, there is a temperature profile inside the sensitive element, which is symmetric with a maximum in the center. Hence, the terms that arise in eq. 2.7 have to be considered as average values, especially the convective heat transfer coefficient h and the wire temperature T_w. The dimensionless group called Nusselt number shall be introduced, defined as

$$\mathrm{Nu} = \frac{hD}{k_f}$$

Where k_f is the thermal conductivity of the flow at its temperature T_f, and not the one of the wire. Hence, eq. 2.7 can be written as:

$$I^2 R_w = \pi D l h (T_w - T_f) = \pi l k_f (T_w - T_f)\,\mathrm{Nu} \tag{2.8}$$

In eq. 2.8, all the dependencies of the convective heat transfer coefficient on the geometry of the problem, on the fluid and flow properties, are discharged on the Nusselt number. These properties themselves can be gathered in other dimensionless groups, and hence Nu can be written as a function of:

$$\mathrm{Nu} = f\left(\mathrm{Re}, \mathrm{Pr}, \mathrm{Gr}, \frac{\Delta T_w}{T_f}, \frac{U^2}{c_p \Delta T_w}, \frac{l}{D}, \varphi\right) \tag{2.9}$$

Where the dimensionless groups that appear in this relationship are so defined:

- Reynolds number: $\mathrm{Re} = \frac{\rho_f U D}{\mu_f}$
- Prandtl number: $\mathrm{Pr} = \frac{c_p \mu_f}{k_f}$
- Grashof number: $\mathrm{Gr} = \frac{g \rho_f^2 D^3 \beta \Delta T_w}{\mu_f^2}$

$\Delta T_w = T_w - T_f$ = Characteristic temperature difference
μ_f = Dynamic viscosity of the fluid at its temperature T_f
ρ_f = Fluid density at its temperature T_f
c_p = Specific heat at constant pressure of the fluid at its temperature T_f
β = Volumetric expansion coefficient of the fluid
g = Gravity acceleration constant
U = Fluid velocity magnitude
φ = Yaw angle, which is the complementary angle between the wire axis and the flow direction

Now, a brief description of the parameters of eq. 2.9 will be given:

- Re $\rightarrow$ Reynolds number
  Very well known dimensionless group that expresses the ratio of inertia forces over viscous forces.
- Pr $\rightarrow$ Prandtl number
  Another very widely used dimensionless parameter that is known for comparing the diffusivities of momentum, expressed by the fluid viscosity and energy, expressed by its conductivity.

- Gr $\rightarrow$ Grashof number
  Used when dealing with natural convection, since it describes the importance of buoyancy over viscosity.

- $\frac{\Delta T_w}{T_f} \rightarrow$ Overheat ratio
  This ratio is a characteristic dimensionless temperature difference that takes into account the fluid properties variation due to the non-uniformity of the temperature profile inside the wire. In fact, a non-uniform temperature profile of the wire leads to non-uniformities in the temperature profile of the flow close to the wire itself.

- $\mathrm{Ec} = \frac{U^2}{c_p \Delta T_w} \rightarrow$ Eckert number
  This dimensionless group expresses the ratio of the kinetic energy of the flow and the heat transfer driving force. The interesting observation is that the Eckert number can be related to the Mach number as follows:

  $$\mathrm{Ec} = \frac{U^2}{c_p \Delta T_w} = \mathrm{Ma}^2(\gamma - 1)\frac{T_f}{\Delta T_w}$$

  where $\gamma = \frac{c_p}{c_v}$ is the specific heat ratio. As a general rule, Mach number is important in this analysis, but in incompressible flow conditions it can be omitted. In the present work, two uses of the HW for wake measurements are presented: one downstream of a VAWT at very low air velocities, where the flow can be considered incompressible and Ma is not of interest, and the other one downstream of an axial-flow turbine statoric cascade, where the flow velocities are much higher and Ma becomes relevant.

- $\frac{l}{D} \rightarrow$ Aspect Ratio
  It is the shape parameter of the wire, and hence it accounts for the geometry of the instrument.

- $\varphi \rightarrow$ Yaw Angle
  It takes into account the geometry of the flow with respect to the wire.

Hence, the Nusselt number can be written as a function of the following parameters:

$$\mathrm{Nu} = f\left(\mathrm{Re}, \mathrm{Pr}, \mathrm{Gr}, \mathrm{Ma}, \frac{\Delta T_w}{T_f}, \frac{l}{D}, \varphi\right) \tag{2.10}$$

Eq. 2.10 is the most complete form of the Nusselt number expression that can be figured out. Nevertheless, such equation is rather complex to be handled in practical applications. Hence, some approximations are made:

1. Infinite wire: $\frac{l}{D} \to +\infty$
2. Negligible overheat effects
3. Negligible effects of the flow direction
4. Negligible natural convection
5. Negligible compressibility effects

Hence, eq. 2.10 can be written in the following simplified form:

$$\mathrm{Nu} = f(\mathrm{Re}, \mathrm{Pr}) \tag{2.11}$$

It is possible then to conclude that heat transfer in the hot wire is described by two dimensionless groups: the Reynolds number Re and the Prandtl number (Pr). The first is more related to the flow conditions, while the second depends only on the fluid characteristics and not on the velocity field of each specific case. Besides, the heat transfer properties of the flow change a lot when passing from laminar to transitional to fully turbulent regimes, depending on the value of (Re). As a consequence, it is not possible to draw a unique relation for the Nusselt number.

King's Law

One of the very first laws for the description of the hot wire heat transfer was proposed by L. V. King in 1914, and still today it is considered one of the most valid relations to calibrate the instrument. The so called King's law states that:

$$\mathrm{Nu} = 1 + \sqrt{2\pi\,\mathrm{Pé}} \tag{2.12}$$

Where Pé is the Péclet number, defined as:

$$\mathrm{Pé} = \frac{\rho_f c_p U D}{k_f} = \mathrm{Re} * \mathrm{Pr} \tag{2.13}$$

Eq. 2.12 is considered valid only for some values of the Péclet number, falling in the range $(0.08, +\infty)$. Hence, eq. 2.12 can be rewritten as:

$$\mathrm{Nu} = 1 + \sqrt{2\pi\,\mathrm{Pé}} = 1 + \sqrt{2\pi\,\mathrm{Re}\,\mathrm{Pr}} \propto \sqrt{\mathrm{Re}} \tag{2.14}$$

The relation originally proposed by King is now used in a slightly different form, since the two constants 1 and $\sqrt{2\pi}$ have been replaced by two other constant parameters that are determined experimentally and change from case to case. For negligible natural convection and flow compressibility, the two constants are actually functions of the Prandtl number, and eq. 2.14 is written in a general form as:

$$\mathrm{Nu} = C_1(\mathrm{Pr}) + C_2(\mathrm{Pr})\,\mathrm{Re}^{0.5} \tag{2.15}$$

An empiric law of this kind was proposed by Kramers in 1946 and it is reported in the eq. 2.16 below:

$$\mathrm{Nu} = 0.42\,\mathrm{Pr}^{0.2} + 0.57\,\mathrm{Pr}^{0.33}\,\mathrm{Re}^{0.5} \tag{2.16}$$

Eq. 2.16 is valid in diatomic gases, and hence in air as well, in the range for Reynolds: $\mathrm{Re} \in (0.5, 10^4)$. To be precise, for the dimensionless groups computation, furthermore, the gas properties shall be evaluated at the so called film temperature. This is an average temperature between the flow and the wire ones.

$$T_{film} = \frac{T_w + T_f}{2} = T_f + \frac{\Delta T_w}{2}$$

Another very important phenomenon that has to be studied when dealing with hot wire anemometry, is the dependency of the wire resistance with its temperature. This is the principle on which the constant temperature HW anemometer is based, and can be expressed by the following relation:

$$R_w = R_0\big[1 + b(T_w - T_0) + b_1(T_w - T_0)^2 + ...\big] \tag{2.17}$$

Where R_0 is the wire resistance at the reference temperature T_0, while b_1 and b_2 are the coefficients that relate the temperature variation to the resistance one, with respect to their own references. For practical applications, the quadratic terms are usually neglected, since b_2 is four orders of magnitude smaller than the other coefficient b_1. Hence, eq. 2.17 can be simplified and the temperature difference $\Delta T_w = T_w - T_f$ can be easily rewritten in terms of resistance difference $R_w - R_f$, where R_f is nothing but the wire resistance evaluated at the fluid temperature T_f.

$$T_w = T_f + \frac{R_w - R_f}{bR_0} \tag{2.18}$$

Hence, replacing eq. 2.18 in eq. 2.8, the following expression for the energy balance on the wire is obtained:

$$I^2 R_w = \pi l k_f \frac{R_w - R_f}{b R_0} * \mathrm{Nu} \tag{2.19}$$

Besides, if the expression for Nu presented in eq. 2.16 given by Kramers is considered, and it gets plugged in eq. 2.19, which is possible when $\mathrm{Re} > 40$, the following equation is obtained:

$$I^2 R_w = \pi l k_f \frac{R_w - R_f}{b R_0} \left[0.42\,\mathrm{Pr}^{0.2} + 0.57\,\mathrm{Pr}^{0.33}\,\mathrm{Re}^{0.5}\right] \tag{2.20}$$

Eq. 2.20 can be rearranged in a standard way as:

$$\frac{I^2 R_w}{R_w - R_f} = A + B\sqrt{U} \tag{2.21}$$

Where the two constants A and B replace those originally present in the King's law and become:

$$A = [\text{King}] = 1 \rightarrow A = [\text{Kramers}] = 0.42 \frac{\pi l k_f}{b R_0}\,\mathrm{Pr}^{0.2}$$

$$B = [\text{King}] = \sqrt{2\pi} \rightarrow B = [\text{Kramers}] = 0.57 \frac{\pi l k_f}{b R_0} \left(\frac{\rho_f D}{\mu_f}\right)^{0.5} \mathrm{Pr}^{0.33}$$

For a HW anemometer with a diameter of 5 μm, as the one used for the tests, eq. 2.20 can be used only in case of particularly high velocity, as explained by the constraint on Re above, which means for U higher than 150 m/s. For the specific cases investigated in the present work, this never happens. Even in the axial turbine stage measurements, where the velocities are definitely higher than the VAWT ones, the air velocity remains below 150 m/s. For $\mathrm{Re} < 44$, instead, the equation proposed by Collis and Williams (1959) shall be used:

$$\frac{I^2 R_w}{R_w - R_f} = A + B U^{0.45} \tag{2.22}$$

Where the two coefficients A and B are determined experimentally and the flow properties shall be evaluated at the film temperature. Moreover, in order to make eq. 2.22 even more general, the following expression can be written:

$$\frac{I^2 R_w}{R_w - R_f} = A + B U^n \tag{2.23}$$

Where also the exponent n has to be determined experimentally, by means of a proper calibration of the probe. The main reason why eq. 2.24 is the most interesting one, is that the three coefficients A, B and n depend a lot on the wire condition, they can change significantly from case to case, and it is not possible to predict them analytically. This is why an empirical deduction of those coefficients has to be preferred to any analytical derivation.
Particularly important in HW anemometry is to have a heat transfer equation that is valid also at very low Reynolds numbers, and this aspect has been improved by the same Collis and Williams:

$$\mathrm{Nu}\left(\frac{T_{film}}{T_f}\right)^{-0.17} = 0.24 + 0.56\,\mathrm{Re}^{0.45} \qquad for\ 0.02 < \mathrm{Re} < 44 \quad (2.24)$$

$$\mathrm{Nu}\left(\frac{T_{film}}{T_f}\right)^{-0.17} = 0.48\,\mathrm{Re}^{0.51} \qquad for\ 44 < \mathrm{Re} < 140 \quad (2.25)$$

Once again, the fluid properties have to be evaluated at the film temperature. The first equation is drawn for low Reynolds flows, usually subsonic ones, while the second relation is for high Re. Notice that in eq. 2.24 and 2.25, a temperature correction is present, but further experiments carried out by Ahmed, showed that this approach does not work for cases in which heat transfer goes in the opposite direction, from the fluid to the wire, which is the case of a fluid that is hotter than the sensitive element. Hence, a relation that can be applied to both hotter and colder flow cases has an expression similar to eq. 2.24, but it considers a correction based on the viscosity ratio instead of the temperature ratio. This is not the case of the experimental campaigns presented in this work, but it is still an interesting issue from the literature point of view.

$$\mathrm{Nu}\left(\frac{\mu_{film}}{\mu_f}\right)^{0.15} = 0.21 + 0.50\,\mathrm{Re}^{0.45} \quad (2.26)$$

For low values of the Reynolds number usually observed during HW anemometry measurements, it is possible to figure out a tight relationship between heat transfer on the wire and the fluid-dynamic resistance produced by the wire. An example of such relation has been proposed by Davies and Fisher, and it is the following:

$$\mathrm{Nu} = \frac{c_f}{\pi\gamma}\,\mathrm{Pr} * \mathrm{Re} \quad (2.27)$$

Where c_f is the friction coefficient, for which the authors propose the following formulation:

$$c_f = 2.6\,\mathrm{Re}^{-2/3} \qquad for\ 0.1 < \mathrm{Re} < 50 \tag{2.28}$$

It might be interesting to compare eq. 2.28 with eq. 2.24 and 2.25 proposed by Collis and Williams, and then it will be possible to notice that within such range, substituting c_f with $2c_f$ in eq. 2.27, a higher correspondence of the two expressions is achieved.

In HW anemometry literature, several other laws are available, trying to characterize heat transfer. An example is the one proposed by Cole and Roshko, specifically for very low Reynolds number flows:

$$\mathrm{Nu} = \frac{2}{\ln \frac{8}{\mathrm{Pé} - \Gamma}} \tag{2.29}$$

Where $\Gamma = 0.577...$ is the Euler-Mascheroni constant.

2.3 The Electronics

The electronics is the other fundamental part of the instrument. It has the purpose of expressing the heat transfer of the wire in terms of an electric voltage, which is the output signal registered by the acquisition software, and then elaborated to obtain velocity magnitude and direction. The whole electronic system is made of a Wheatstone bridge and an electric circuit. The first is independent of the power source, while the second one has a different arrangement depending on whether the anemometer is in a Constant Temperature (CT) or a Constant Current (CC) configuration.

2.3.1 The Wheatstone Bridge

The Wheatstone bridge is a particular configuration of four resistances placed at the four sides of a square, also called diamond-like arrangement, as shown in Fig.2.4, in a series-parallel configuration. The resistances are then connected to a voltage supply, and a ground terminal, which measures zero voltage when the parallel branches are balanced.

When a variation in one of the four resistances is registered, the bridge becomes unbalanced, and the measured voltage is different from zero and proportional to the resistance change. For the case of the HW anemometer, one of the four resistances of the bridge is the wire resistance itself, and when a change in the flow velocity takes place, there are two possibilities:

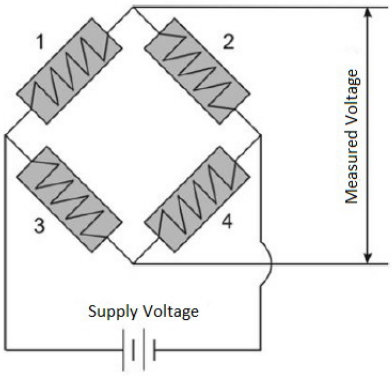

Figure 2.4: A scheme of the Wheatstone bridge

1. Constant Current (CC) configuration:
   The flow velocity affects heat transfer and if a constant current is supplied to the wire, its temperature will change according to the energy balance on the wire itself. The consequence of the wire temperature change is a change in the value of the resistance, which is a function of the material temperature. Hence, the resistance change will lead to an imbalance of the bridge, and hence to a measured voltage different from zero. This configuration is the most intuitive one, but it has a very important disadvantage, which is low frequency response due to the heating and cooling transients of the wire. This makes the CC configuration unsuitable for turbulence measurements, which require a high frequency response in order to properly catch all the turbulent fluctuations of the flow properties in time.

2. Constant Temperature (CT) configuration:
   In this second configuration, the hot wire resistance is supposed to remain constant in order to keep the wire temperature constant during measurements. Since the changes in the flow velocity tend to change also the wire temperature, to keep it constant, the only term that can be controlled is the energy generation by Joule effect inside the wire. Hence, the control unit will change the current inside the wire in order to compensate heat transfer and keep the wire temperature constant. Finally, this current change can be directly related to the flow velocity. Without temperature changes inside the wire, there are no thermal transients, but only electric ones, which are much faster, and hence able to give a much higher frequency response, by far more adequate for turbulence measurements.

In the next paragraph, the two configurations will be presented deeper in detail, while in the following lines the basic laws that regulate the electric circuit of the Wheatstone bridge are reported. Consider the following notation:

$E \rightarrow$ Circuit supply voltage
$V \rightarrow$ Measured voltage
$i \rightarrow$ Circulating current
$R_w \rightarrow$ Wire resistance
$R_x \rightarrow$ Variable resistance adjacent to the wire
$R \rightarrow$ Other resistances of the Wheatstone bridge

With reference to Fig.2.4, the hot wire is represented by branch 3, and the variable resistance adjacent to it is addressed as branch 4. Then, it is possible to write the equation of the bridge, considering the other resistances R_1 and R_2 equal one to another.

$$R_1 = R_2 = R$$

$$V = V_1 - V_2 = V_w - V_x$$

Where applying the voltage dividers rule, the voltages are proportional to the resistances of the branch:

$$V_w = \frac{R_w}{R_w + R} E$$

$$V_x = \frac{R_x}{R_x + R} E$$

And rewriting the equation:

$$\begin{aligned} V &= E\left(\frac{R_w}{R_w + R} - \frac{R_x}{R_x + R}\right) \\ &= E\left(\frac{R_w R - R_x R}{(R_w + R)(R_x + R)}\right) \end{aligned}$$

Hence, it is possible to notice that the measured voltage V is proportional to the supplied one, addressed as E. When the voltage read is null, the bridge is balanced, and this happens when the wire resistance is equal to the one of the adjacent side:

$$V = 0 \qquad \rightarrow \qquad R_w = R_x$$

When the Wheatstone bridge is unbalanced in such a way that all are resistances change of a certain delta, the equation above becomes:

$$\Delta V_{imbalance} = E\left(\frac{(R_w+\Delta R_w)(R+\Delta R)-(R_x+\Delta R_x)(R+\Delta R)}{((R_w+\Delta R_w)+(R+\Delta R))((R_x+\Delta R_x)+(R+\Delta R))}\right)$$
$$= E\frac{R^2}{(2R)^2}\left(\frac{\Delta R}{R}-\frac{\Delta R}{R}+\frac{\Delta R_w}{R_w}-\frac{\Delta R_x}{R_x}\right)$$

There are generally two possibilities when measuring with a Wheatstone bridge:

1. By resetting
2. By deflecting

The first option consists in considering zero the condition at which the bridge is balanced. Hence, any imbalance is compensated by a resistance variation, which is used to measure the original perturbation of the bridge balance. The second possibility, instead, which is the case of the hot wire anemometer, consists in measuring the voltage variation from a reference "zero" configuration which is not at zero voltage. Hence, in the HW, the measured voltage coming from the measuring diagonal has to be seen in terms of increment from the reference condition. Under the hypothesis that only one side of the bridge can be affected by the fluid motion and can then contribute to the imbalance of the system, which is the one related to the wire resistance, the former expression can be rewritten as:

$$\Delta V = E\frac{\Delta R}{4R^2}$$

Which remarks that the voltage increment that is measured at the extremes of the bridge is proportional to a change in the electric resistance of the wire.

2.3.2 Constant Current Configuration

All the instruments that work on the basis of a constant current circuit, are built with an electric circuit in the configuration shown in Fig.2.5, where the two main components are the Wheatstone bridge and the current generator.

Two of the four resistances of the bridge, the ones indicated with R_1, are equal one to another, while the comparison resistance R, instead, is equal to the resistance of the heated wire, generally 1.8 times greater than

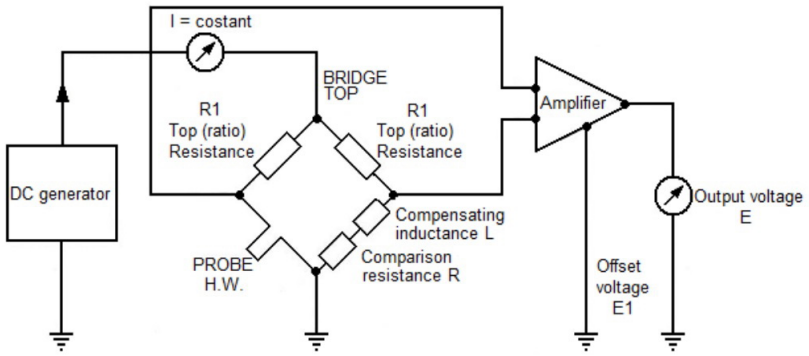

Figure 2.5: Constant Current circuit configuration

the one of the cold wire. Finally, the last resistance of the bridge is the hot wire itself, which is compared with the variable resistance R while measuring. To register the zero velocity condition of the instrument, the current I is increased until the bridge is balanced. During measurement, a change in the flow velocity will change the heat transfer between fluid and wire, and hence will change the wire temperature and its resistance as well. As a consequence, the bridge will suffer an imbalance, that is registered in terms of voltage on the measuring diagonal. Looking at the first Ohm's law:

$$V = RI = \left(\frac{\rho_{el}(T) l}{\frac{\pi D^2}{4}} \right)$$

Where $\rho_{el}(T)$ is the electric resistivity of the material, which in a metal wire is a linear function of temperature:

$$\rho_{el}(T) = \rho_{el}^0 \left[1 + \alpha (T - T^0) \right]$$

Hence, it is evident that a change in the flow velocity will directly lead to a change in voltage at the terminals of the bridge measuring diagonal.

One of the greatest advantages of using a HW anemometer, is that it has a good capability of detecting flow properties fluctuations, which is a quality that is needed when measuring turbulence. The anemometer in a CC configuration, actually, if these fluctuations are too fast, is not particularly adequate for this kind of measurements, because its thermal inertia will give rise to a lag in the output voltage signal. Since the wire is a very tiny piece of metal, its thermal inertia will be small, and its thermal transient will expire fast, but still not enough for fast fluctuations measurements. Assuming that:

- The wire is short enough to consider the temperature profile as a constant over its entire length.
- Radiative heat transfer is negligible.

It is possible to write an expression for a heated wire probe frequency response, starting from an instantaneous heat transfer equation.

$$I^2 R_w = h(U)(T_w - T_f) + C_w \frac{dT_w}{dt} \tag{2.30}$$

Where R_w is the hot wire resistance, $h(U)$ is the overall heat transfer coefficient as a function of the flow velocity, T_w and T_f are the wire and the flow velocities respectively, and C_w is the wire thermal inertia:

$$C_w \approx \rho C \frac{\pi D^2 l}{4} \tag{2.31}$$

Then, eq. 2.30 can be linearized and solved for small velocity perturbations. The heat transfer coefficient and the output voltage can be expressed as the sum of an average term and its fluctuation:

$$h(U,t) = \overline{h(U)} + h'(U,t) \tag{2.32}$$

$$E(t) = \overline{E}(t) + E'(t) \tag{2.33}$$

Hence, it is possible to write the following expression for the fluctuating components, which is a first order differential equation:

$$\tau_w \frac{de}{dt} + E' = -h' \tag{2.34}$$

Where τ_w is the time constant of the wire, which is a term that is proportional to the speed of the instrument response, and it can be written as:

$$\tau_w = \frac{C_w R_w}{R_0 h(U)} \tag{2.35}$$

Where $R_0 = R_w(T_0)$ is the resistance of the cold wire. Hence, eq. 2.30 corresponds to a first order instrument, whose maximum frequency response to a sinusoidal fluctuation is:

$$f_{max} = \frac{1}{2\pi\tau_w} \tag{2.36}$$

Eq. 2.36 shows the dependency of the frequency response of the anemometer on the flow velocity U, since the time constant of the wire τ_w is a function of the heat transfer coefficient h, which is itself a function of the flow velocity U.

$$f_{max} = f(\tau_w) = f(h(U))$$

It is of course not possible to find a universal value for the maximum frequency response of the HW anemometer in CC configuration, but it is possible to give an order of magnitude for this parameter, which is around 300 Hz. This value is by far too small to give reliable turbulence measurements, which may have frequencies of the order of tens of kilohertz. The poor frequency response can be improved by the introduction of an amplifier characterized by an increasing gain with frequency. This solution is reported in Fig. 2.7.

2.3.3 Constant Temperature Configuration

The configuration at constant temperature (CT), compared to the constant current one, has one main advantage, which is the higher frequency response. This characteristic is fundamental and it is what makes the instrument suitable for turbulence measurements.

The circuit arrangement is presented in Fig.2.8, where it is made clear that the output voltage is amplified, and such signal is then used to evaluate the voltage needed at the supply diagonal in order to satisfy the constant temperature condition. Such output voltage V is for sure a function of the flow velocity, and the wire temperature is kept constant by the variable resistance of the bridge R. Hence, if the gain of the amplifier K is large enough, the bridge imbalance can be considered as:

$$E' \approx \frac{E}{K}$$

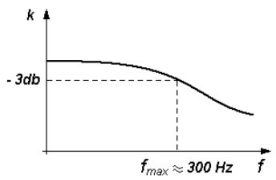

Figure 2.6: CC configuration - Frequency Response

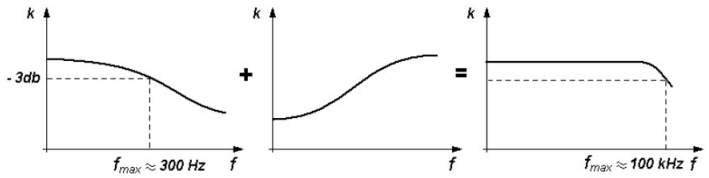

Figure 2.7: CC configuration - Frequency Response with Gain

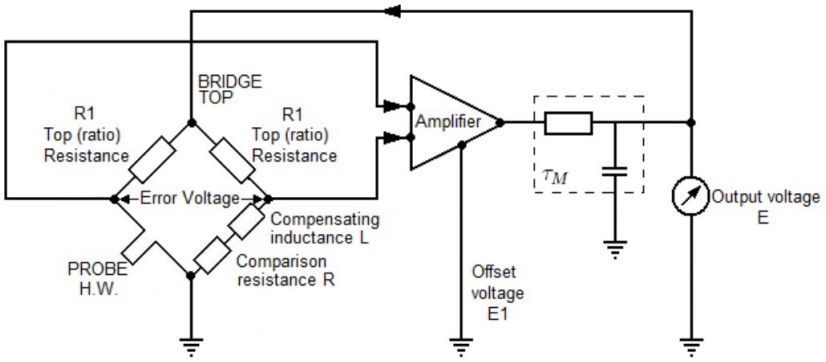

Figure 2.8: Constant Temperature circuit configuration

The wire, then, is kept at constant temperature, or similarly, the temperature fluctuations are $\frac{1}{K+1}$ times smaller than in the constant current configuration. As a consequence, to small fluctuations corresponds a minor role of the thermal inertia in the frequency response limitation. Nevertheless, it is not properly correct to say that the maximum frequency is increased of a factor $\frac{1}{K+1}$. A wider band and a higher frequency response give rise to the need of considering also the dynamic phenomena that may arise is the electronics, which means in the cables and in the amplifier of the anemometer. This makes the problem even more complex and increases the order of the differential equation that governs the dynamic response of the system. It is possible to describe the anemometer as a second order instrument, where the resonance frequency can be written as a function of several parameters:

$$\omega = f\left(\frac{R_w}{R_0}, H, E_1, \tau_M, \tau_w, K, L\right) \tag{2.37}$$

Which are: the time constant of the electric circuit τ_M, the one of the wire τ_w, the inductance L needed to weaken the effect of the transients, and E_1 which is the offset voltage of the amplifier used to damp the system.

Such analysis is of course limited to small oscillations within the system, while to give a deeper understanding of the real system behavior, a third order equation should be written.

The maximum frequency response can be adjusted and eventually increased playing on the compensation inductance L, and on the amplifier offset voltage E_1. This procedure should be done with care, since instabilities may arise in the system. In any case, it is still possible to obtain an over-damped condition, in which the bandwidth is maximum. Nevertheless, it is important to remind that the frequency response of the probe depends on the heat transfer coefficient $h(U)$ and hence directly on the flow velocity U. Hence, the probe response optimization should be evaluated for the specific case in which the sensor will operate, especially in terms of flow velocity. Thanks to this, the HW sensor in a CT configuration will give a good response also for high fluctuations of the flow properties.

With a constant temperature configuration, it is possible to obtain a bandwidth of the order of 30 kHz, which means that turbulent fluctuations typical of a subsonic flow can be caught easily and neatly. No frequency compensation is needed in this case.

In light of the advantages that the CT configuration brings compared to the CC one, for all the applications in which a high readiness is required, such as turbulence measurements, the constant temperature configuration has almost completely overcome the constant current one. Also the HW anemometer used in all the tests reported in this work is built in a constant temperature configuration.

2.4 Angular Sensitivity

One of the greatest advantages of the hot wire anemometer is that it is sensitive both to the flow velocity magnitude and to its direction. The flow velocity can be decomposed in three spatial components in the wire reference frame:

- $U_n \rightarrow$ Normal: axis normal to the wire and parallel to the prongs.
- $U_t \rightarrow$ Tangential: axis parallel to the sensitive element extension.
- $U_b \rightarrow$ Binormal: axis normal to both the wire and the prongs.

The flow direction, instead, is evaluated in terms of yaw and pitch angles:

- $\varphi \rightarrow$ Yaw: angle between the binormal direction and the projection of the flow velocity in the binormal-tangential plane.

- $\vartheta \rightarrow$ Pitch: angle between the binormal direction and the projection of the flow velocity in the normal-binormal plane.

The three velocity components are felt by the wire in a different way one to another, meaning that each velocity component has a different cooling potential, depending on its relative direction in the wire reference frame. The main velocity component that the wire is feeling is the normal one U_n, but all the three of them play a role in the heat transfer between wire and flow. In the following picture, the wire frame of reference is presented, all velocity components and the flow angles taken positive.

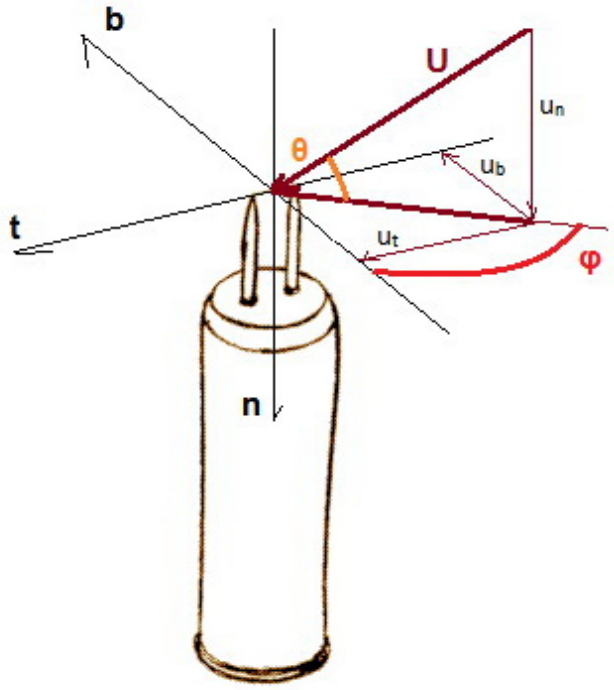

Figure 2.9: Reference Frame

The probe is sensitive both to yaw and pitch angle variations, even if sensitivity to yaw is much higher than the one to pitch. In case of a wire of a very large aspect ratio ($AR > 600$), the so called *cosine law* for a straight wire can be written:

$$U_{eff} = U_n \tag{2.38}$$
$$U_n = U \sin \vartheta \tag{2.39}$$
$$U_{eff} = U \sin \vartheta \tag{2.40}$$

This law is validated by several tests performed by Champagne, Sleicher and Wehrmann (1967). In any case, it is rare to have hot wires of such a high aspect ratio, hence, this law is usually used as a first approximation to approach the problem. For the cases that are considered in this work, a simple modification to eq. 2.38 proposed by Hinze (1959) will be considered. This is known as the Hinze relationship:

$$U_{eff}^2 = U_n^2 + k^2 U_t^2 \tag{2.41}$$

Eq. 2.41 considers the effects of the additional cooling of the wire produced by the tangential component of velocity, and it can be rewritten as:

$$U_{eff}^2 = (U \sin \vartheta)^2 + k^2 (U \cos \vartheta)^2 \tag{2.42}$$
$$= U^2 (\sin^2 \vartheta + k^2 \cos^2 \vartheta) \tag{2.43}$$

Since in the Hinze equation the factor k^2 is used to account for the tangential component of velocity, it can also be addressed as the yaw factor, which is the flow angle produced by a non-null tangential velocity. This factor has been studied by Webster (1962), and it has been found to be around $k = 0.2 \pm 0.01$ for the most conventional probes. Nevertheless, with a deeper analysis of the problem, such factor is actually a function of several parameters, among which there are the wire aspect ratio, the flow velocity magnitude, and the yaw angle itself. In the following graphs, the dependency of the yaw factor on aspect ratio and yaw angle is presented.

In Fig.2.10 [9] it is evident that k decreases of a factor around four when the aspect ratio increases from 200 to 600. The effect of the yaw angle on the yaw factor k, instead, is shown in the following picture, where two probes with same aspect ratio are compared at different velocities. The picture on the left shows a standard probe with support needles 1.25 mm apart, while the one on the right shows the same probe but with prongs that are 3 mm distant.

From Fig. 2.11 [9], it is evident that the more the needles are far one from another, the smaller is the wire sensitivity to yaw angles variations. This results with a coefficient k that for small yaws is even three times

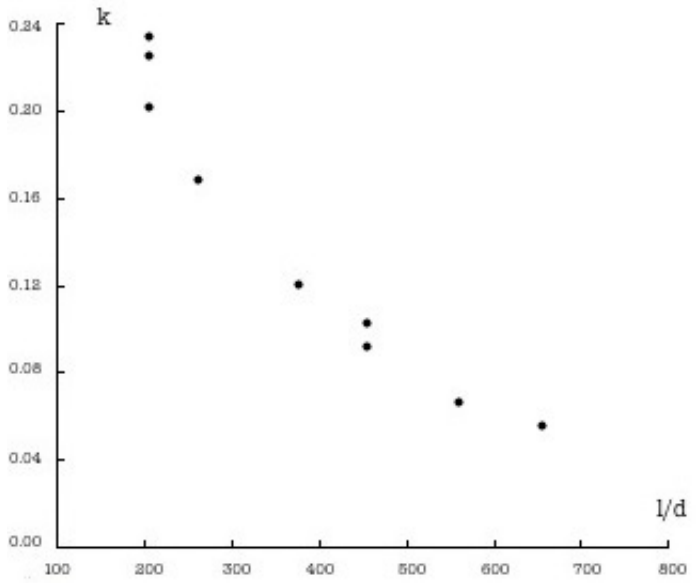

Figure 2.10: Yaw factor dependecy on the aspect ratio.

smaller in the right-hand graph than in the left-hand one, with reference to Fig.2.11.

A further contribution to this topic was given by Jørgensen, who introduced the effect of the pitch flow angle, passing from a 2D to a 3D approach to the problem. An influence of the pitch angle means an influence of the binormal component of velocity on the wire cooling, which leads to the following final formula for the cooling velocity felt by the wire.

$$U_{eff}^2 = Q^2 = U_n^2 + k^2 U_t^2 + h^2 U_b^2 \tag{2.44}$$

Where the term h^2 is a multiplier that has the same function as k^2 for the tangential velocity. The coefficient h is called hence *pitch coefficient* since it accounts for the pitch angle, as previously mentioned. With reference to Fig.2.9, the three velocity components can be then written as:

$$U_n = U \sin\vartheta \tag{2.45}$$

$$U_{bt} = U \cos\vartheta = \sqrt{U_t^2 + U_b^2} \tag{2.46}$$

$$U_t = U_{bt} \sin\varphi = (U \cos\vartheta) \sin\varphi \tag{2.47}$$

$$U_b = U_{bt} \cos\varphi = (U \cos\vartheta) \cos\varphi \tag{2.48}$$

Hence, eq. 5.4 can be rewritten as:

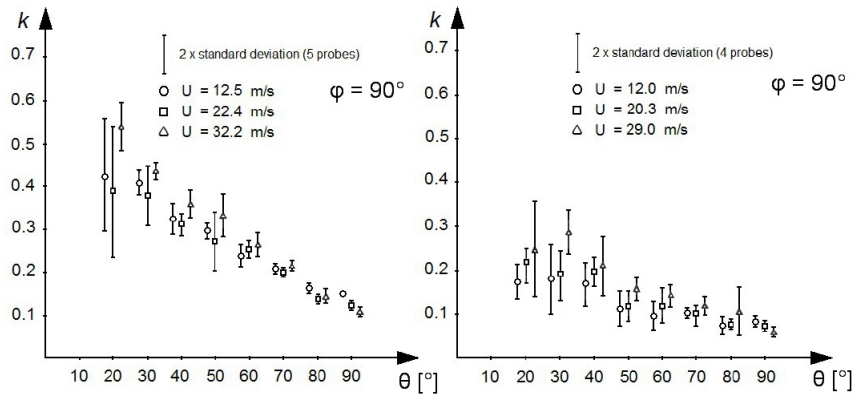

Figure 2.11: Yaw factor dependency on the yaw angle. Standard probe with 1.25 mm distant prongs (left) in comparison with another whose prongs are 3 mm apart (right).

$$Q^2 = (U \sin\vartheta)^2 + k^2(U \cos\vartheta \sin\varphi)^2 + h^2(U \cos\vartheta \cos\varphi)^2 \tag{2.49}$$

$$= U^2(\sin^2\vartheta + k^2 \cos^2\vartheta \sin^2\varphi + h^2 \cos^2\vartheta \cos^2\varphi) \tag{2.50}$$

The pitch coefficient h is represented in the following graphs as a function of the pitch angle for $\varphi = 0°$. Opposite to the yaw coefficient, h is much less sensitive to the aspect ratio and to the pitch angle variations. In analogy to what presented for the yaw coefficient, also h is represented for two different probes with the same aspect ratio and at different flow velocities: the standard probe (left plot) whose needles are 1.25 mm distant, and a probe whose prongs are 3 mm far from each other (right plot).

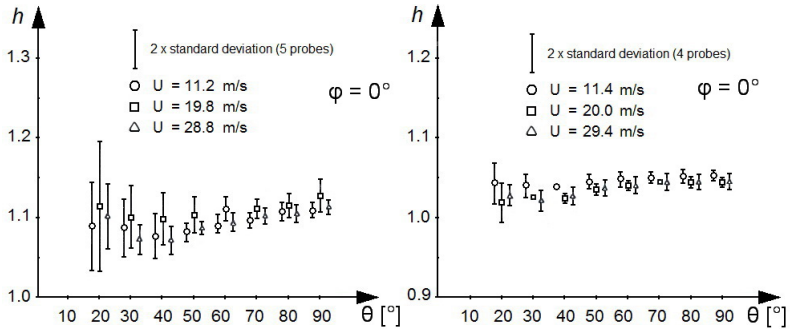

Figure 2.12: Pitch coefficient dependency on the pitch angle. Standard probe with 1.25 mm distant prongs (left) in comparison with another whose prongs are 3 mm apart (right).

From Fig. 2.12 [9] it is clear that h usually assumes values in the narrow range of $h \approx 1.05 \div 1.15$, depending on the probe. Besides, increasing the pitch angle, the change in h is very small.

Finally, what arises from this analysis is that with a 2D probe, it is possible to be sensitive to all the flow directions, and hence to measure the three components of velocity in space. Nevertheless, to achieve this result it is necessary to have a really complicated system for moving the probe along the three spatial directions. Such system is not always available, due to its complexity and cost. Hence, for the cases presented in this work, two strategies have been developed: in the VAWT wind tunnel measurements, a probe slanted by $\alpha = 45°$ was used, while in the axial turbine stage campaign, the flow has been considered two-dimensional, reasonably neglecting the radial component of velocity.

2.5 Life and Aging of the Probe

The HW anemometer is a particularly fragile instrument, due to the delicate structure of its tiny sensitive element. Hence, it is quite common to accidentally break the wire, and here below are listed some of the reasons that can lead to the probe failure.

Wear

Wear is mainly due to the thermal stress that the wire suffers during operation. The hot wire is so small that its measurements can be reasonably considered as punctual, and its temperature uniform along the wire. Nevertheless, in reality, its temperature profile is not constant, but shows a maximum in the center, and a minimum at the extremities where heat is exchanged by conduction through the prongs. Besides, since the probe is made of a real wire, its diameter is not perfectly constant along its length, and this means that hot spots inside the wire may arise, producing further temperature heterogeneity inside the sensitive element. Furthermore, on the wire there can be fouling and dirtiness deposits that penalize heat transfer and hence increase the local temperature of the sensor. Finally, another overheating factor is the metal oxidation in air, which has to be considered as a further cause of hot spots. All these phenomena lead to the wear of the probe, which increases with the total operating hours and with the operating temperature set on the wire. Aging has its indicators, which are drifts of the cold resistance and sensitivity losses expressed by a change in the slope of the King's calibration curve.

Burnout

A burnout is typically produced by a too high temperature of the wire, which is caused of course by a too high overheat set at the beginning of the operation, when the wire is connected to the electronics, for the case of a CT anemometer. To avoid such problem, in modern anemometers a current limitator is adopted to prevent over-currents that may cause the burnout of the wire. This condition may arise also in the case of a region of the wire that is cooled more than the rest. In such situation, the feedback amplifier will tend to give an extra-current in order to compensate the heat dissipated to the surroundings, overheating the sensitive element. Constant current anemometers, instead, suffer from a different kind of burnout, that takes place when the fluid is slowed down all at a sudden, and the wire is not adequately cooled during its thermal transient, and this can burn the wire. This is why burnout is a quite common phenomenon, that can be distinguished from other sources of failure of the probe. Finally, it is easy to detect: using a magnifying glass, in the absence of aerodynamic forces on the wire, it is possible to notice that a small portion of the wire is missing, and the console voltage output is zero.

Breakage

As mentioned already, the probe is particularly delicate, since it is made of a very thin metal wire. Hence, it is very easy to break it even with the touch of a finger, but it can break also when inserted in holes or even in its protective container, due to unexpected impacts. Another common cause of the wire breakage is the presence of tiny dust particles in air that may collide with the wire at high velocities of the wind tunnel and snap it. Even if the air is completely free of dust, the flow itself generates a fluid-dynamic thrust that if too strong, will bring the wire to breakage. This is why hot wire anemometers cannot operate at too high Mach numbers. Finally, the sensor is more likely to break if it is covered of a large coating of contaminants, which increases the fluid-dynamic drag of the wire without increasing its strength, and if it is not securely welded to the support prongs.

Fouling

The probe fouling is caused by the presence of contaminants that cannot be removed from the flow. These contaminants may be dust, lints,

flakes or dried wax coming from the floor, or small oil droplets from nearby machinery. This condition may make testing impossible, and hence, contaminants have to be removed from the flow as much as possible, otherwise the instrument will experience sensitivity and frequency response reduction in an unpredictable way.

Chapter 3

Calibration

The present work discusses the application of hot wire anemometry (HW) in two situations: in the wake of a Vertical Axis Wind Turbine (VAWT) and downstream of the stator of an axial-flow turbine stage (GT). In this chapter, calibration will be presented in detail and a particular attention will be paid to the differences that arise when calibrating the instrument for one application or the other. These come up as a consequence of the different operating conditions in which the instrument is working during the test. Furthermore, the calibration of the slanted HW will be discussed. This second type of instrument can be useful to increase the sensitivity to pitch angle variations, and it has been used for this purpose during the experimental campaign on the VAWT of Dec. 2016.

Calibration is a fundamental procedure that is necessary in order to have a direct correspondence between the output signal (i.e. voltage) of the probe and the physical quantities that want to be measured. In the specific case, the quantity of interest is the flow cooling velocity, which is then elaborated through a specific software to obtain the velocity components in space. The calibration procedure for VAWT measurements is described separately from the GT one, since the two cases are characterized by different operating conditions and hence the instrument calibration has to be thought in another way. The basic differences between the VAWT and the GT applications stand in the flow velocity, together with the different flow temperature. These two issues are dealt as follows:

- Velocity $\rightarrow$ At high velocities ($U >\sim 25\ m/s$), there is experimental evidence that the yaw coefficient tends to a constant value $k^2 \rightarrow 0.025$. Hence, for the GT application, where the air velocities are typically much higher ($U \approx 120 \div 160\ m/s$), the calculation of this coefficient can be omitted, and the asymptotic value can be con-

sidered. For the VAWT application, instead, the velocities remain far below 25 m/s, and hence both the pitch and the yaw coefficients have to be determined experimentally by means of a proper angular calibration.

- Temperature $\rightarrow$ In a CT HW anemometer, the wire temperature is set by definition. Nevertheless, heat transfer is not based on the wire temperature only, but on the temperature difference between the wire and the cooling flow. This means that the flow temperature plays a role as well as the wire temperature, but a simple correction as the one presented in the following paragraphs is not enough to account for such a big change in the flow temperature as the one occurring in the GT, because also the empirical coefficients of the King's law depend on it. This has been proved by the temperature calibration of the HW probe done in January 2018 for the GT tests, but it was not noticed during the VAWT experimental campaign, due to the fact that the flow around VAWT is nearly isothermal, hence, it is implemented only for the first case.

3.1 The Equipment

3.1.1 Calibration Rig

Before going in the detail of the calibration procedures adopted for the two cases, the test rig and the overall laboratory system will be presented. For both campaigns, the calibration of the probes was carried out in the Laboratory of Fluid Machines (LFM) of the Energy Department at Politecnico di Milano. In the following picture, the schematics of the calibration system is presented.

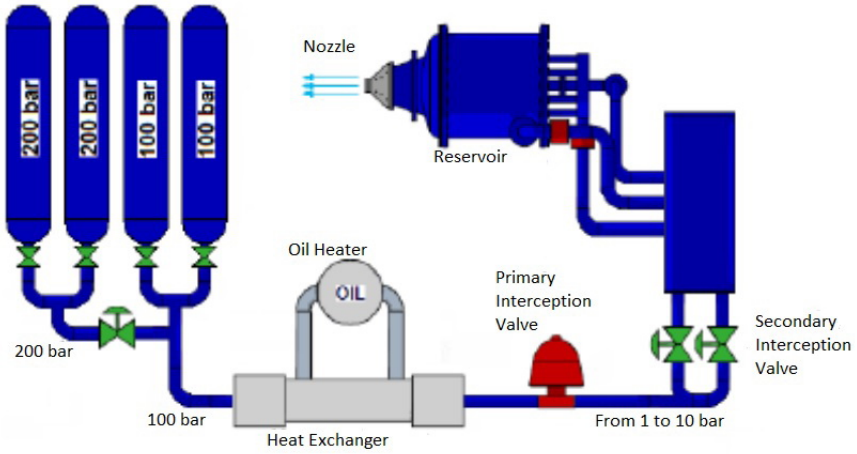

Figure 3.1: The schematic representation of the calibration system.

The air that is used to calibrate the probe comes from the reservoir tanks represented on the left-hand side of Fig.3.1, in which ambient air has been pressurized by a series of reciprocating compressors, and then stocked. These tanks are placed on the outside of the laboratory, at the external temperature and at different pressures, as reported in the picture. Actually, the real pressure inside the tanks is slightly lower than the nominal one for safety reasons, and it goes from 200 nominal bars to 180 actual bars. Through a system of valves, the highly pressurized air is throttled first from 180 to 80 bars, then mixed with the mid-pressure air, and throttled again down to a value set by acting on the primary interception valve, that can stand in between 10 bars and the atmosphere. A more precise regulation is then performed by means of two secondary interception valves, mounted on two parallel lines, that in the end merge into the last reservoir. This way, the velocity of the flow that is running over the wire can be set by defining a pressure ratio over the exit nozzle.

This last throttling is what sets the final Mach number of the calibration flow, and hence the final air flow rate. On this plant, there is also the possibility to heat up the air by means of an oil heat exchanger, working with a maximum temperature of $80°C$. This feature has been actually used for the temperature calibration of the probe for the GT test of January 2018.

3.1.2 Monitoring Equipment

The laboratory system illustrated in the above paragraph is managed by means of a panel located inside the control room. This allows the experimental team to operate on the plant from a remote position, which is a relevant advantage for safety concerns. All the acquisition system is managed by the software LabView©, which displays in real time the flow properties measured inside the piping. These values come from the following probes:

- Pressure probe → Connected to a Rosemount® 3051S transducer, it measures the total pressure upstream of the nozzle.
- Thermocouple → Of the TERSID® T type, it measures the total temperature of the tank.

The ambient conditions, instead, are measured with a barometer for pressure and with another thermocouple for temperature. This information is useful to evaluate the flow rate assuming that the expansion inside the nozzle is adiabatic and isentropic, which means that it takes place at constant total temperature and pressure. The steps to follow are:

$$\frac{p_{T0}}{p_{amb}} = \left(1 + \frac{\gamma - 1}{2}\,\mathrm{Ma}_{0s}^2\right)^{\frac{\gamma}{\gamma-1}} \tag{3.1}$$

$$\mathrm{Ma}_{0s} = \sqrt{\frac{2}{\gamma - 1}\left[\left(\frac{p_{T0}}{p_{amb}}\right)^{\frac{\gamma-1}{\gamma}} - 1\right]} \tag{3.2}$$

$$\frac{T_{T0}}{T_0} = \left(1 + \frac{\gamma - 1}{2}\,\mathrm{Ma}_{0s}^2\right) \tag{3.3}$$

Where the total pressure recorded by the probe upstream of the nozzle is p_{T0}, while p_{amb} is the ambient pressure. The temperatures involved, instead, are T_{T0}, total temperature measured upstream and constant throughout the process, and T_0 static temperature of the same section. Hence, it is possible to compute:

$$a_0 = \sqrt{\gamma R T_0} \tag{3.4}$$
$$v_{0s} = a_0 \, \mathrm{Ma}_{0s} \tag{3.5}$$
$$\dot{m} = \rho_0 v_{0s} A \tag{3.6}$$

Where a_0 is of course the sound speed of the upstream flow, and ρ_0 is the flow density at the same T_0 and p_0 conditions. The nozzle cross-sectional area in the formula is represented by $A = 80 \times 80 = 6400 \; mm^2$.

3.1.3 Capture Device

The voltage signals given as outputs by all the measuring devices installed on the calibration nozzle are first amplified, and then sent to a shared terminal board. This sends the signals to the National Instruments PCI-6052E, a 16 bit capture device located inside the workstation. Finally, the user interface is the software LabView©, which by means of easy-to-use graphics, allows the experimental team to continuously monitor in real time the flow quantities measured by the ancillary probes, together with the voltage signal coming from the hot wire in calibration. Inside the LabView© interface, three main sections appear:

- Zeros → Inside this environment, the user sets the voltage reference condition for the measurement. This is a voltage signal that corresponds to the zero velocity case, and it is identified with E_0. In order to capture the zeros, the operator has to be sure that the air in which the wire is immersed is completely still. This procedure is quite delicate, because the HW anemometer is a particularly sensitive instrument. Hence, the HW is covered with a cap, to ensure no air motion.

- Motors → This is the environment that allows to activate and to monitor the system of motors that moves the probe during calibration.

- Acquisition → Through this environment, the user can program the motors movement during calibration, name the output file, monitor the conditions of the flow coming from the nozzle, which is manually regulated by the control panel nearby, and when the interface shows a stable velocity, start the acquisition. The quality of the acquired signal can be then monitored in this same environment.

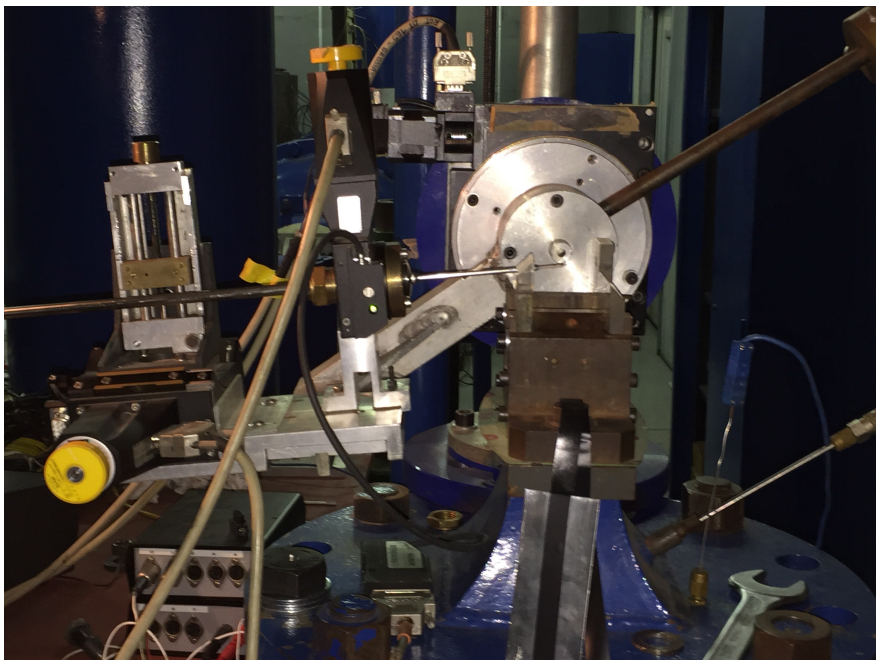

Figure 3.2: Picture of the probe during calibration

3.1.4 Probe Moving System

The HW probe has to be mounted on an aluminum support locked with a mandrel-nut blockage system, placed in order to have the probe directly facing the incident jet. The motors that move the probe are two, in order to give the probe two degrees of freedom: one rotational around the probe axis, indicated by the angle φ, the yaw angle, and one goniometrical, associated to the pitch angle ϑ. In Fig.3.2 the picture of the probe moving system is reported. The rotational motor is the Micos® DT-65N, bounded to the Micos® Goniometer WT-90. They are both stepping motors and their movement can be completely regulated by means of the LabView© software.

3.2 Calibration Procedure

The wires to be calibrated are two:

1. Normal Hot Wire → Needles of the same length and sensitive element perpendicular to them.

2. Slanted Hot Wire → One needle is longer than the other, and the

sensitive element is then inclined of a certain angle α with respect to the stem. In this specific case $\alpha = 45°$.

The normal wire has been used both in the VAWT and in the GT experimental campaigns, while the slanted one was used only in the VAWT test, to investigate the axial velocities inside the wake.

3.2.1 Preparing Calibration

Before placing the anemometer in front of the calibration jet, the experimental apparatus has to be prepared, in the sense that the wire resistance at the ambient temperature, together with the cable and support resistances have to be determined. To do this, the technical datasheet provides the wire resistance at a reference temperature and the linear correlation coefficient α that represents the dependency of the resistance with temperature itself.

$$R_{ref} = R(T_{ref}) \ [\Omega]$$

$$\alpha = \frac{\Delta R}{\Delta T} \left[\frac{1}{°C}\right]$$

For these wires, the data are given for a temperature of $T_{ref} = 20°C$, but the temperature of the room at which the wire is getting prepared for calibration is not the reference one. For instance, during the calibration of 2017/18, the measured ambient temperature was $T_{amb} = 17.4°C$. Hence, the wire resistance is not R_{ref}, but a different one calculated by means of the coefficient α and indicated from here on as R_{amb}, by means of the following linear relationship.

$$R_{amb} = R(T_{amb}) = R_{ref} + \alpha(T_{amb} - T_{ref}) \tag{3.7}$$

The results are then listed in the following table for the two wires. Mind that the normal wire was calibrated twice, once in 2016 for the VAWT campaign, and one in 2018 for the GT tests.

Once the wire resistance at the ambient conditions is known, the resistance of the supports and the one of the heated wire have to be measured. To do this, the HW is mounted on the probe holder with the aid of two pins and the mandrel-nut blockage, and it is connected to the anemometric unit, which is represented in Fig.3.3. Mind that the connection cable

HW	$\alpha[1/°C]$	$R_{amb}[\Omega]$
N('16)	0.0036	3.95
N('18)	0.0036	3.91
S	0.0036	3.91

Table 3.1: Resistance results of the two wires: normal (N), and slanted (S).

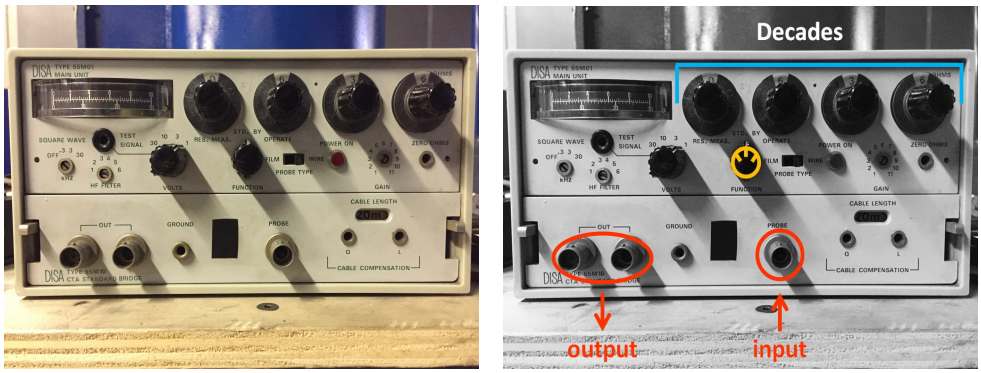

(a) Picture of the anemometric unit **(b)** Description of the equipment

Figure 3.3: The Anemometric Unit.

has to be of a certain pre-determined length to be properly compensated by the system, which is 5 m for the normal wire, and 20 m for the slanted one. Such cable is then plugged to the *probe* BNC connector showed in Fig.3.3.

The next step is then to compensate the resistances of cable, probe holder and needles by means of the short-circuit probe. This is a probe that has zero resistance on the wire, and hence it allows to put in evidence the resistance of all the remaining apparatus. For this purpose, the *function* control knob has to be set on *res.meas.*, which stands for "resistance measurement". With this function active, the anemometric unit enables the reading of the analogical indicator on the upper-left corner of the panel. By turning the control knobs of the potenziometers addressed as *decades*, the cursor moves inside the panel, and when it adjusts on the red notch in the center of the panel, the Wheatstone bridge is balanced and the *decades* report the value of the apparatus resistance (cable, probe holder and needles).

Now, the user has to rotate the *function* knob on *std.by*, and replace the short-circuit probe with the real one to calibrate, then turn again the

function on *res.meas*. This way, before heating up the wire, operating again on the *decades*, the overall resistance R_p can be measured. This is the resistance at ambient temperature of the the sum of the wire and its support apparatus.

$$R_p = R_{amb} + R_l \tag{3.8}$$

Where R_{amb} is again the wire resistance at ambient temperature, R_l is the resistance of the leads, and R_p the sum of the two. Inverting eq. 3.8, the wire resistance at ambient temperature can be calculated to validate the result of eq. 3.7.

Now, the wire temperature has to be chosen according to the manufacturer suggestions for the application of the probe. Hence, for the purpose of both experimental campaigns, an overheat of $\Delta T_w = 200°C$ with respect to the ambient is chosen for both sensors. This means that the wire temperature will be:

$$T_w = T_{amb} + \Delta T_w$$

And the resistance to be set on the *decades* in order to obtain the desired temperature T_w on the wire, can be calculated by means of the same aforementioned linear relationship (eq. 3.7).

$$R_w(T_w) = R_{dec} - R_p == \alpha R_{amb}(T_w - T_{amb}) \tag{3.9}$$

The unknown in eq. 3.9 is the value of the resistance to set in the *decades* potenziometers. Once computed, it can be imposed by changing the same control knobs, and the wire gets heated to T_w [10].

HW	$R_{dec}[\Omega]$
N(‘16)	6.43
N(‘18)	6.37
S	6.36

Table 3.2: Decades resistances of the two wires: normal (N) and slanted (S).

3.2.2 E_0 Temperature Calibration

To the purpose of the GT application, an alternative evaluation of the zero velocity condition is necessary, since in this situation, two issues arise, which are:

- The test temperature of the hot wire is $T_{op} = 35°C$, which is above the ambient. Furthermore, for obvious technical reasons, the air inside the GT test rig has to flow through the plant in order to be heated up to T_{op}, and this means that the zero, that has to be evaluated at null velocity, must be captured before the air starts to flow, at a temperature much colder than the test one. The two things are not consistent, and a proper temperature calibration is needed.

- As described in chapter 3.1.3, the zero capturing procedure is particularly delicate, and the wire has to be encapsulated in order to be sure that no air is moving around it. It is evident that this important precaution cannot be taken inside the test turbine casing, and, furthermore, it is not possible to know precisely the temperature of the air surrounding the wire.

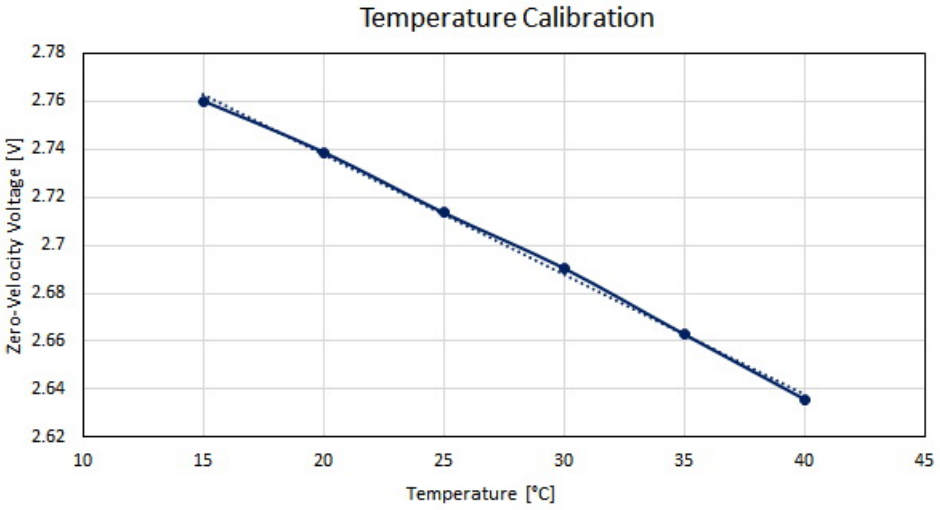

Figure 3.4: Temperature calibration of the zero tension

Due to these two major concerns, a temperature calibration of the zeros was carried out during the experimental campaign of January 2018. The hot wire was placed in a thermostatic oven, set at temperatures going from $15°C$ to $40°C$ with steps of $5°C$. After setting the oven temperature, for each step of the calibration range, the expiry time of the thermal transient should pass before capturing the zero. The result of the calibration is expressed by the graph of Fig.3.4.

When the system reaches the regime conditions, the temperature inside the oven is homogeneous, and hence it is reasonable to assume that natural convection is negligible, and only heat conduction through the gaseous medium shall be considered. Heat conduction is governed by the Fourier's diffusion law.

$$\dot{q}(x_i) = -k_w \frac{dT}{dx_i}$$

Heat transfer by conduction is then proportional to the temperature difference between wire and fluid. Besides, electrical resistivity depends linearly on temperature through the coefficient α, with a reasonable first order approximation, as put in evidence by eq. 3.7. As a consequence, a linear relationship can be considered adequate to fit the temperature calibration data, as the goodness of the R^2 value remarks. On the basis of these results, from here on, for the GT application, the zero will be calculated analytically with reference to the flow temperature upstream of the stator, and not captured at the beginning of the testing session. The equation resulting from the linear fitting presented above is then:

$$E_0[V] = mT[^\circ C] + q \tag{3.10}$$

With:

$$m = -0.00499$$
$$q = 2.83748$$

3.2.3 King's Calibration

The King's law calibration is the procedure through which the flow velocity magnitude is related to a voltage signal, by means of the King's law, which is the following, derived directly from eq.2.24.

$$E^2 = E_0^2 + BQ^n \tag{3.11}$$

Where E is the voltage output of the wire, E_0 is the one of the zero velocity condition, Q is the air cooling velocity, while B and n are coefficients to be determined experimentally, resulting from the calibration. To perform this analysis, the two wires follow two different procedures.

- The normal wire is placed perpendicular to the flow jet, as shown in Fig.3.2, with zero yaw and pitch angles ($\varphi = 0^\circ,\ \vartheta = 0^\circ$). In these

conditions, the only velocity component present is the binormal one, and hence, the Jørgensen law for the cooling velocity becomes:

$$Q^2 = \cancel{U_n^2} + k^2\cancel{U_t^2} + h^2 U_b^2$$

Besides, for $\varphi = 0°$, the flow symmetry condition ensures that $h = 1$, and hence $Q = U_b$, from which it is possible to consider the cooling velocity equal to the actual flow one.

- The slanted wire is placed on a dedicated support, inclined of the same $\alpha = 45°$, in order to keep the sensitive element perpendicular to the flow. This way, only the normal component survives in the Jørgensen equation:

$$Q^2 = U_n^2 + k^2\cancel{U_t^2} + h^2\cancel{U_b^2}$$

And again, the cooling velocity coincides with the velocity magnitude of the jet ($Q = U_n$).

The arrangement of the slanted wire during King's law calibration is made clear in the following pictures.

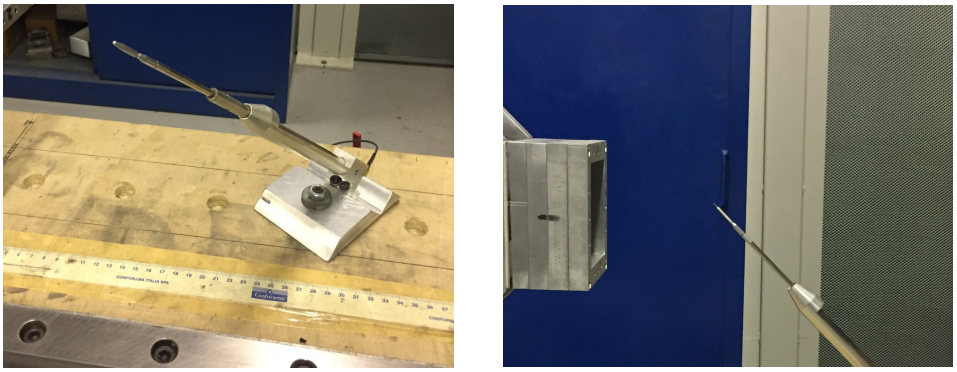

(a) **(b)**

Figure 3.5: The slanted wire during King's law calibration.

Inside the calibration air plant, the valves are regulated in order to cover a range of velocities, or Mach numbers, that is adequate for the values that the wire will experience during operation. For the VAWT application, the calibration velocity range is in between 2 and 20 m/s, and in this case it makes no difference to talk about Mach numbers or velocity magnitudes, since these are so low that the flow is considered

incompressible. In the GT application, instead, the velocities are much higher, and the calibration range is measured in terms of Mach numbers, for similarity reasons. Such Ma range is [0.1 0.2 0.3 0.4] in the ascending calibration sequence, and three other points are captured going down from high to low Mach, at Ma = [0.35 0.25 0.15] to validate the first results.

Temperature is another issue to be considered in this step of the calibration procedure. For the VAWT case, a simple ambient temperature calibration is applied, without turning on the heater, since the test air in the wind tunnel is actually the one of the ambient. Hence, a simple temperature correction will be performed in this case, as presented in the following paragraphs, but no temperature dependence of the King's law coefficients is put in evidence, and hence no temperature calibration is needed. For the GT application, instead, the situation is different, since the test temperature ($T_{op} = 35°$) is higher than the one of the room during calibration, around $T_{cal} \approx 15 \div 17°C$, depending on the day. Given this finding, a temperature calibration is performed for the GT application. For this last case, the oil heat exchanger is turned on, in order to increase the air temperature from T_{amb} to $35°C$, and there is evidence of a temperature dependency of the King's coefficient.

The results of the King's calibration for the VAWT application is represented in the following chart, both for the normal and the slanted wire.

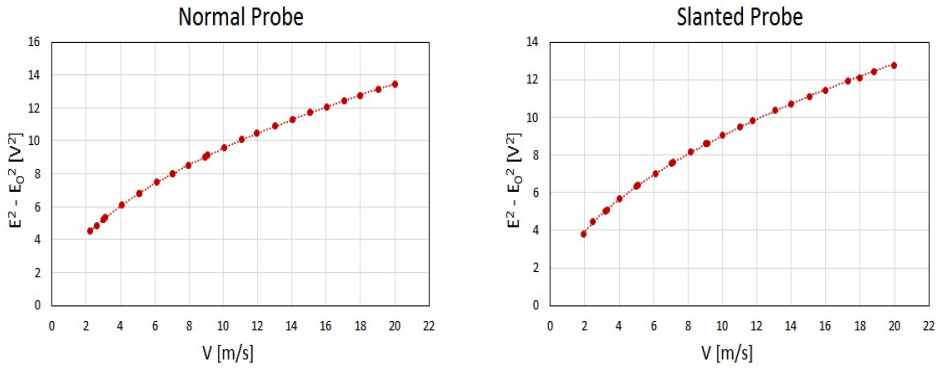

(a) Normal HW King's curve. **(b)** Slanted HW King's curve.

Figure 3.6: King's law for the VAWT application.

For these two cases, it should be noticed that only one curve is enough to represent the experimental dataset of the calibration, and it is the one identified by the following empirical parameters:

The King's law performed on the GT case, instead, gives the results presented in Fig.3.7. Opposite to the VAWT case, for the GT application,

HW	B	n
N	3.0391	0.4973
S	2.7793	0.5116

Table 3.3: Empirical parameters of the King's law for both normal (N) and slanted (S) wires, calibrated for the VAWT.

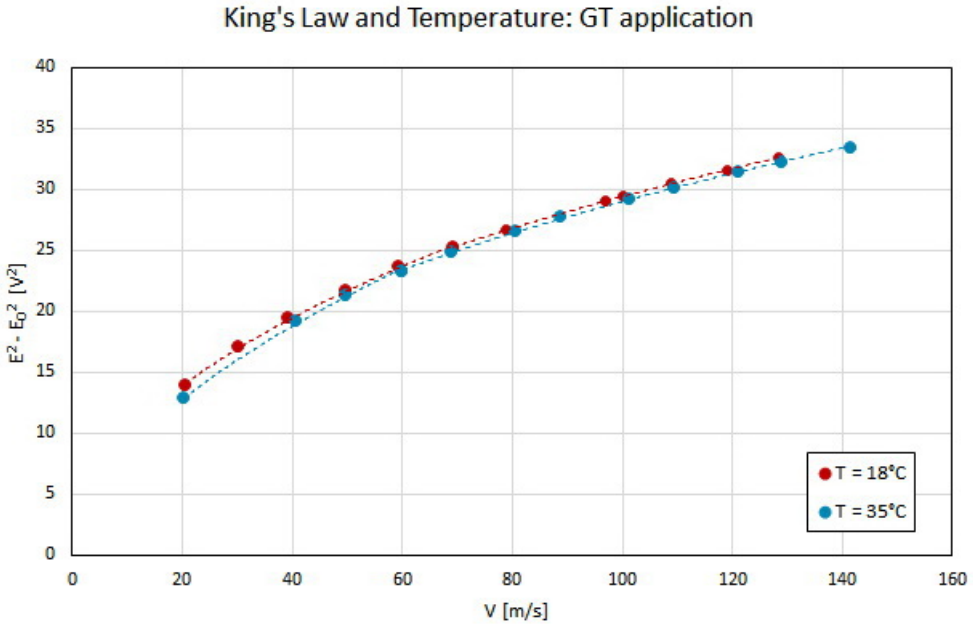

Figure 3.7: King's law for the GT application, with temperature as a parameter.

the King's law has been fitted with two different branches in order to give a better fitting, where the threshold between the two regions is a velocity of 70 m/s. Furthermore, as mentioned above, in Fig.3.7 the influence of temperature is clear, represented by the difference between the two adjacent curves. The empirical parameters that will be used to elaborate the GT data are of course the ones derived at high temperature:

$$B_l = 2.4218 \qquad B_h = 4.1898$$
$$n_l = 0.5552 \qquad n_h = 0.4200$$

Where the l subscript stands for *low* and is referred to the velocities

lower than the threshold one, while, on the contrary, h stands for *high* and is related to velocities that stand above the threshold.

3.2.4 Temperature Correction

The temperatures registered during calibration are not equal to those present during the test. Such drift affects the measurement, and hence, it is necessary to refer to a unique temperature by means of the following correction.

$$E_{corr}^2 = E^2 \frac{T_w - T_{amb}}{T_w - T_{flow}} \tag{3.12}$$

Where T_{amb} is the reference, and for the GT case, for instance, it is equal to $17.4°C$. The temperature T_{flow}, instead, represents the flow temperature upstream of the probe, whatever it is. This correction is the simplest and most effective approach to compensate temperature drifts from calibration to test. No correction was applied to the zero voltage, because for the GT calibation the zeros were already calculated analytically by means of eq. 3.10, while for the other cases, an analogous correction is already applied during the King's law, and hence it is already corrected.

3.2.5 Angular Calibration

The next step is the probe angular calibration, which is the procedure through which it is possible to evaluate the yaw and pitch coefficients k^2 and h^2 of the Jørgensen law reported below.

$$Q^2 = U_n^2 + k^2 U_t^2 + h^2 U_b^2 \tag{3.13}$$

As already mentioned at the beginning of the chapter, the angular calibration for the VAWT differs from the GT one. For the second case, the flow velocities are high enough to consider a constant value of the pitch coefficient, equal for every yaw angle and every velocity, $k^2 = 0.025$, and this makes the calibration procedure easier.

For the VAWT application, instead, both k^2 and h^2 have to be calculated in angular calibration, and to fulfill this task in an intuitive way, the idea is to decouple the dependency of the Jørgensen equation on the two coefficients. In the probe reference frame, in a general form that is valid for both the normal and the slanted wire, the velocity vector can be decomposed as:

$$
\begin{aligned}
U^2 &= U_n^2 + U_t^2 + U_b^2 \\
U_n &= U\big(\sin\vartheta\cos\alpha + \cos\vartheta\sin\varphi\sin\alpha\big) \\
U_t &= U\big(\cos\vartheta\sin\varphi\cos\alpha - \sin\vartheta\sin\alpha\big) \\
U_b &= U\cos\vartheta\cos\varphi
\end{aligned}
$$

Remembering the Jørgensen eq. 5.4, the cooling velocity can be rewritten in terms of flow velocity magnitude and direction, instead of its three spatial components:

$$
\begin{aligned}
Q^2 = &\big(U\sin\vartheta\cos\alpha + \cos\vartheta\sin\varphi\sin\alpha\big)^2 + \\
&+ k^2\big(U\cos\vartheta\sin\varphi\cos\alpha - \sin\vartheta\sin\alpha\big)^2 \\
&+ h^2\big(U\cos\vartheta\cos\varphi\big)^2
\end{aligned}
\tag{3.14}
$$

This equation was used to perform the angular calibration, in the two ways explained in the following paragraphs.

VAWT Probe Angular Calibration

For the normal wire, the sensitive element is not inclined, by definition, and this allows to introduce the first very important simplification, and to reduce the redundant terms of the notation, $\alpha = 0°$, while for the slanted wire, the inclination $\alpha = 45°$ should be maintained.

In order to easily evaluate k^2 and h^2, the idea is to position the probe such that the flow comes from the tangential-binormal direction, thing that cannot be done for the slanted HW, otherwise the longer prong will completely shadow the wire. For this purpose, the pitch calibration range was $\vartheta \in [-16°; +16°]$ with $2°$ steps. In the reference frame proposed in Fig.2.9, this set of positions corresponds to:

$$
\begin{aligned}
&\varphi = 90° \\
&\mathrm{N} \rightarrow \forall\vartheta \in [-16°; +16°] \text{ step: } 2° \\
&\mathrm{S} \rightarrow \forall\vartheta \in [-15°; +15°] \text{ step: } 5°
\end{aligned}
$$

This φ value is then taken as the reference coordinate to turn the probe around its axis and to calibrate it also in yaw. In this central position, substituting the values of φ and ϑ in eq. 3.14, the following simplified form is obtained:

$$Q^2 = U^2\big(\sin^2\vartheta\big) + k^2U^2\big(\cos^2\vartheta \cancelto{1}{\sin^2\varphi}\big) + h^2U^2\big(\cos^2\vartheta \cancelto{0}{\cos^2\varphi}\big) \tag{3.15}$$

$$= U^2\sin^2\vartheta + k^2U^2\cos^2\vartheta \tag{3.16}$$

And the yaw coefficient can be directly derived for this specific position. Since k^2 depends only on velocity and pitch, but it does not depend on yaw, the value of k^2 obtained for $\varphi = 90°$ is the same for every yaw. The yaw range adopted for this angular calibration goes from $\varphi' = -70°$ to $\varphi' = +70°$, where φ' is the reference frame that considers zero the $\varphi = 90°$ position, hence:

$$\varphi' = \varphi - 90° \rightarrow \varphi'(\varphi = 90°) = 0°$$

Hence, a curve of k^2 for every pitch, yaw and velocity can be derived with this method. In the specific case of the probe calibration for the experimental campaign on the VAWT, the velocity range of the normal probe is $[5\ \ 10\ \ 15\ \ 20]\ m/s$, while the one for the slanted probe is $[5\ \ 10\ \ 15]\ m/s$. Once the k^2 is known, the value of h can be directly obtained starting from the same Jørgensen equation (3.14). For:

$$\forall\varphi' \in [-70°; +70°]\ \text{ step: } 2°$$
$$\vartheta = 0°$$

The value of the pitch coefficient can be evaluated by means of the following:

$$Q^2 = U^2\cancelto{0}{\sin^2\vartheta} + k^2U^2\big(\cancelto{1}{\cos^2\vartheta}\sin^2\varphi\big) + h^2U^2\big(\cancelto{1}{\cos^2\vartheta}\cos^2\varphi\big) \tag{3.17}$$

$$= k^2U^2\sin^2\varphi + h^2U^2\cos^2\varphi \tag{3.18}$$

The results of the angular calibration on this probe are shown in the charts below. First, the chart for h as a function of yaw and pitch is shown in Fig.3.8a. The calculation at $U = 10\ m/s$ is presented as an example, but the same charts done for the other calibration velocities are perfectly analogous. The characteristic feature of this graph is that the wire is clearly symmetric, as the curve is. Furthermore, the reader should notice the value of $h \approx 1.1$ when the flow is perfectly tangential, a result aligned with experience.

Both in Fig.3.8 and Fig.3.9, where the yaw coefficient is plot as a function of pitch angle and velocity magnitude, the curves show an almost

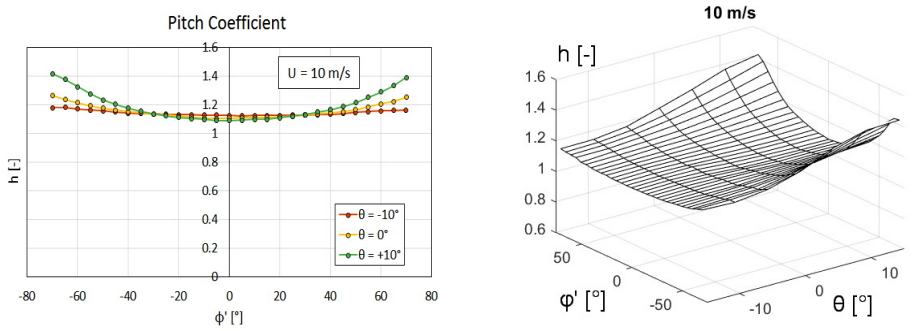

(a) 2D plot (b) 3D plot

Figure 3.8: The coefficient h as a function of pitch angle and yaw angles

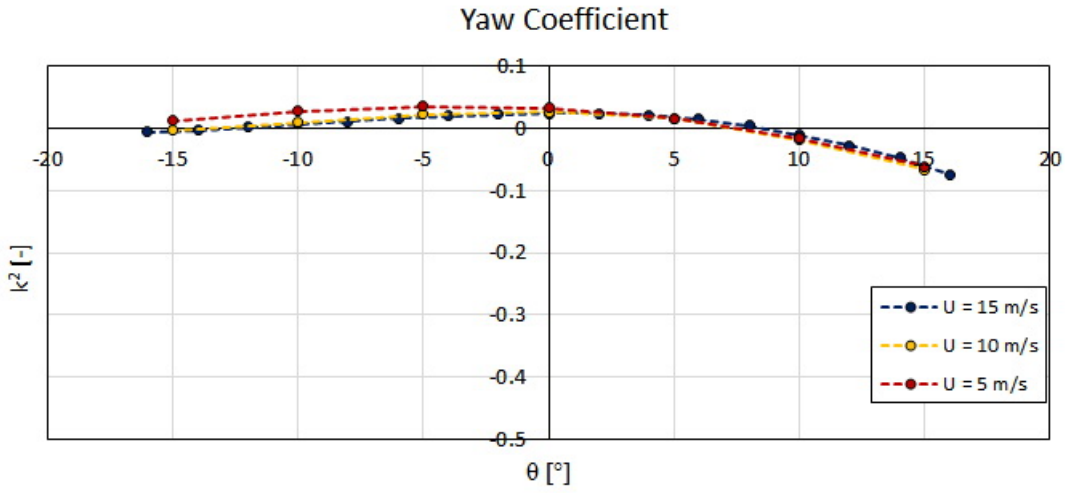

Figure 3.9: The coefficient k^2 as a function of pitch angle and velocity.

flat trend with pitch, especially close to the central position. This is reasonable, since the single wire normal probe is almost insensitive to pitch angle variations. More detailed charts are presented in [7].

GT Probe Angular Calibration

The probe angular calibration for its application in the GT is much simpler. Despite the probe is the same as the VAWT test one, it is not possible to use the same parameters, since the velocity range of operation is much different. For the high velocities at which the GT will be tested, there is no doubt that the yaw coefficient will reasonably have a constant

value $k^2 = 0.025$. Hence, there is no need to pre-rotate the probe of 90° and to switch from one yaw angle reference frame to another, which is a procedure that further complicates the data processing. In addition, for this occasion, the angular calibration was performed with air heated up by means of the oil heat exchanger up to $T_{flow} = 35°C$, and in the following angle and velocity ranges:

$$\begin{aligned}
&\varphi \in [-70°; +70°] \text{ steps: } 2° \\
&\vartheta = 0° \\
&\text{Ma} = [0.1 \quad 0.2 \quad 0.3 \quad 0.4]
\end{aligned}$$

Notice that pitch angle here is kept equal to zero. No pitch angle calibration has been performed, for two reasonable assumptions:

1. The pitch angle in a GT corresponds to a radial component of velocity, which is known to be very small from previous measurements, as already recalled.

2. The normal probe is very little sensitive to pitch.

Hence, the only thing to do is to compute the pitch angle h, once again by means of the Jørgensen equation (eq. 5.4,3.14). With zero pitch angle, eq. 3.14 becomes:

$$\begin{aligned}
Q^2 &= U^2 \cancelto{0}{\sin^2 \vartheta} + k^2 U^2 \left(\cancelto{1}{\cos^2 \vartheta} \sin^2 \varphi\right) + h^2 U^2 \left(\cancelto{1}{\cos^2 \vartheta} \cos^2 \varphi\right) && (3.19) \\
&= k^2 U^2 \sin^2 \varphi + h^2 U^2 \cos^2 \varphi && (3.20)
\end{aligned}$$

From which it is straight-forward to derive the h coefficient for any yaw angle and any flow velocity (directly related to the Mach number). The results of this angular calibration are shown in the chart that follows.

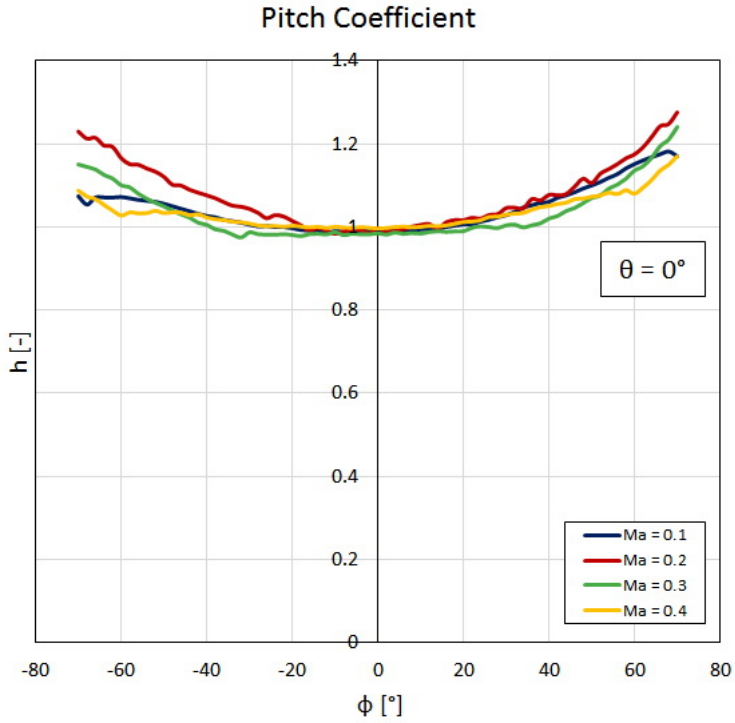

Figure 3.10: The h coefficient as a function of yaw angle and Mach number.

Chapter 4

The Experimental Apparatus

After calibration, described in detail in Ch.3, the probe is placed on the rig for real operation. In the present chapter, a description of such testing apparatus will be provided, which is fundamental to understand the results of the experimental campaign. The chapter is organized in two main sections: one for the VAWT campaign, and the other one for the GT investigation. The two need to be treated separately, due to the profound differences between them. The VAWT was tested in the large-scale low-turbulence wind tunnel of Politecnico di Milano, while the GT is located on the test rig in the Laboratory of Fluid Machines (LFM) of the Energy Department of Politecnico di Milano.

4.1 The VAWT Experimental Apparatus

4.1.1 The Wind Tunnel Building

The VAWT experimental campaign, from which the data elaborated in the present work are extracted, was carried out in December 2016 in the large-scale low-turbulence wind tunnel of Politecnico di Milano. The building hosts a closed loop facility developed on two floors and divided in two sections:

- Low-speed test section (14 m width $\times$ 3.84 m height). Inside it, the air reaches a maximum velocity of around 15 m/s.
- High-speed test section (4 m width $\times$ 3.84 m height). Inside it, the air reaches a maximum velocity of around 55 m/s.

The wind generator is made of two rows of seven fans, where each of them is driven by an inverter controlled electric motor, for an overall

installed electric power of around 1.4 MW. In the wind tunnel, there is the possibility to run tests in two different kinds of environments:

- Closed Chamber configuration (CC) → The testing model is placed inside of a removable room in order to simulate wall effects.
- Open Chamber configuration (OC) → The closed room is removed and the testing model is located directly in front of the upstream tunnel tube.

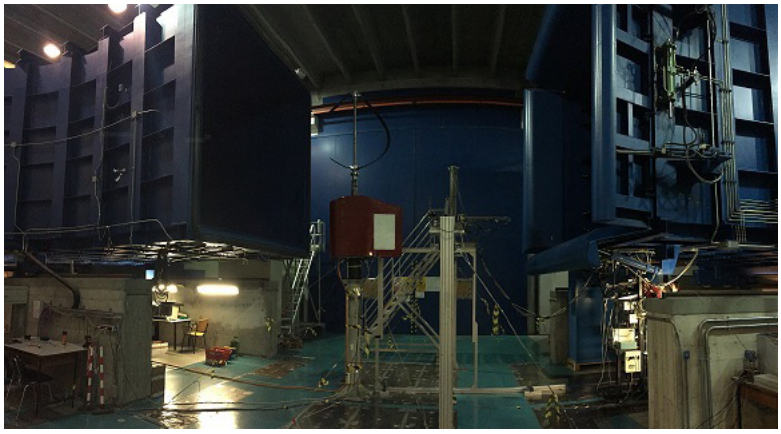

(a) Turbine in front of the fan.

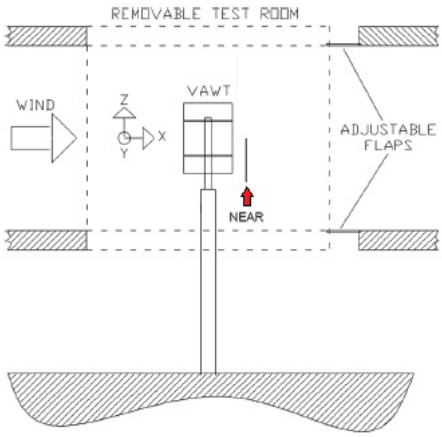

(b) Schematics of the arrangement.

Figure 4.1: The turbine during the testing session in the wind tunnel.

For the campaign carried out on the VAWT of Dec. 2016, the open chamber configuration was chosen, in order to better simulate the real

behavior of the turbine in an unconfined environment. Besides, the test was performed in the high-speed section, located immediately upstream of the diffuser leading to the fans, characterized by a turbulence level $< 1\%$, which is very low. The wind tunnel arrangement used for the campaign is described in Fig.4.1. The wind speed is regulated inside a control room, in which all the flow quantities, together with temperature and atmospheric pressure, are monitored, and the output is registered by the acquisition system [7].

4.1.2 The VAWT Model

Parameter	$H - Darrieus$
Swept area	1.5 m^2
Profile	NACA0021
Chord	0.085 m
Number of Blades	3
Rotor Diameter	1.030 m
Rotor Height	1.457 m
Blade Length	1.457 m
Solidity	0.25
Weight	28 kg

Table 4.1: Turbine features.

Of all the tests done during the campaign of Dec. 2016, the present work discusses only those for the H-Darrieus turbine. The model is a real scale prototype, whose characteristics are listed in table 4.1, it is built with a wooden core, and it has the blades covered with carbon fiber. The turbine shape and a picture of it are reported in Fig.4.2.

4.1.3 The Instrumentation

The probes employed in this test campaign are the normal and the slanted hot wires. These probes were mounted on an aluminum modular structure, provided by ITEM S.r.l., which was able to move in the three spatial directions by means of linear electric motors.

The whole modular structure is moved by means of the following electrical motors, represented in Fig.4.4.

- PK264BE-SG9 stepping motor for the transversal motion (y-direction).

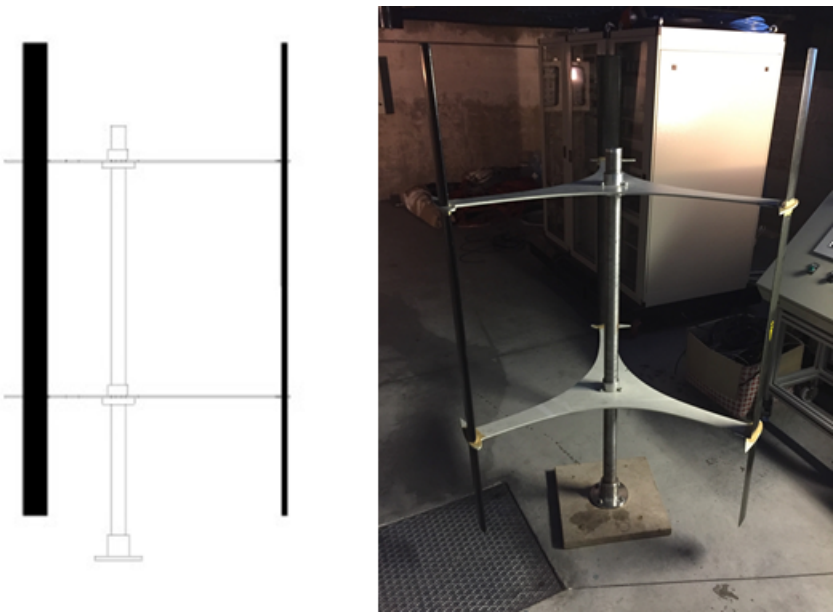

Figure 4.2: The H-Darrieus prototype.

- SUPERIOR ELECTRIC SLO-SYN stepping motors for vertical (z-direction) and streamwise motion (x-direction).
- Two Micos DT-65 electric motors for the rotation of the hot wires around their axes

The modular structure is moved along the three directions of space with the following maximum strokes:

- Streamwise Axial x-direction $\rightarrow$ 3305 mm.
- Transversal Horizontal y-direction $\rightarrow$ 1154 mm.
- Longitudinal Vertical z-direction $\rightarrow$ 805 mm.

The fourth degree of freedom of the probes is the rotation around their axis of $[+45°\ \ 0°\ \ -45°]$, which is required for reasons explained in detail in Chapter 5.

The reference frame for the probe movement was considered centered in the normal hot wire position, a five-hole probe was mounted 80 mm next to it, while the slanted hot wire were standing 50 mm on the other side. These probes are mounted this way for measurement convenience reasons, and this gap is taken into account during data elaboration. The pressure transducers and the anemometric unit for the slanted probe, whose BNC

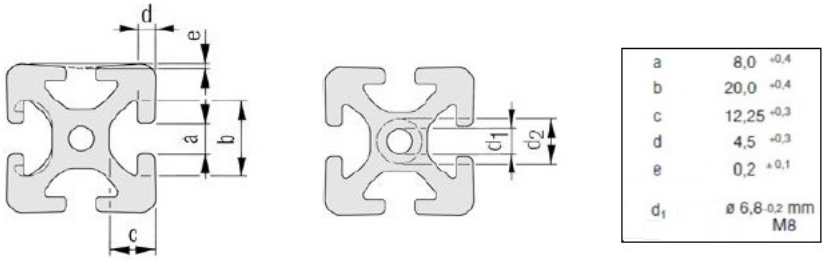

Figure 4.3: The crossbeam and the specifications of the ITEM structure

Tensile Strength	min. 245 N/mm^2
0.2 Rp 0.2 Limit	min. 195 N/mm^2
Specific Weight	2.7 kg/dm^3
Elongation at Break A_5	min. 10%
Elongation at Break A_{10}	min. 8%
Thermal Expansion Coeff.	23.6×10^{-6} $1/K$
Tensile Modulus E	$\approx$ 70 000 N/mm^2
Thrust Modulus G	$\approx$ 25 000 N/mm^2
Hardness	75 $HB - 2.5/187.5$

Table 4.2: Mechanical Characteristics of the ITEM Bar.

cable is 20 m long, were placed on the ground, far from the turbine and the moving system. The anemometric unit for the normal wire, instead, with its 5 m long BNC cable, was secured on a metallic box behind the probes, solidal to the modular structure, and hence moving with it during the test. This latter solution was adopted since the normal HW BNC cable was not long enough to be arranged in a safe position, far from the testing apparatus, as the rest of the acquisition system.

4.1.4 The VAWT Measuring Grid

During tests it is important to be consistent with the reference frame used during calibration, otherwise a correction will have to be implemented during elaboration, and this should be avoided for sake of simplicity. The movement of the probes is then commanded through the LabView software, as for calibration in Chapter 3. Hence, it is useful to introduce the LabView software reference for the spatial coordinates, which is consid-

Figure 4.4: Electric motors adopted for the traversing moment.

ered as an absolute reference frame. In contrast to it, the turbine relative reference frame, shown in Fig.4.5, is the most intuitive way to plot the results. The measurements are taken in the so-called *near wake* measuring plane, which is $1.5R$ downstream of the turbine axis of rotation, while no investigation was carried out on the *far wake* plane, since the most important flow features take place immediately after the flow-blade interaction, in the near-wake, as highlighted in previous experimental campaigns. For symmetry reasons, it is usually assumed that the upper half of the turbine wake behaves as the lower half, and hence only the second half of the turbine trace is covered by the measuring grid. It is important to note that the measuring plane exceeds the wake region in both y and z directions, in order to fully capture the wake evolution and the tip vortex enlargement. This extension covers $2R$ from the turbine axis on both sides, while along the vertical coordinate the mesh exceeds of almost 20% the tip of the blades. Finally, the measuring traverses are positioned in the plane in order to capture as much as possible of the main wake fea-

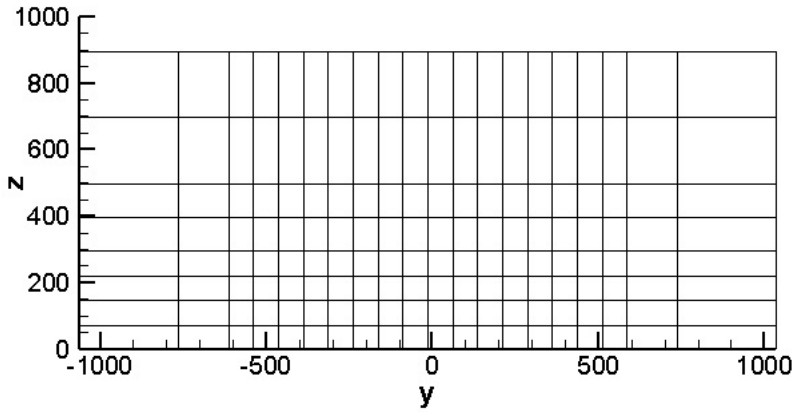

Figure 4.5: The transversal 2D measuring plane.

tures. Hence, they are tighter close to the tip, and located in order to see the flow disturbances generated by the spokes and of the turbine shaft as well. The tests were carried out for different wind velocities, in order to cover a sufficiently wide range in terms of Reynolds numbers (Re) and see the flow field variations with the tip-speed ratio (λ). In this case, velocity magnitude, yaw and pitch angles were investigated, with the aid of the slanted probe.

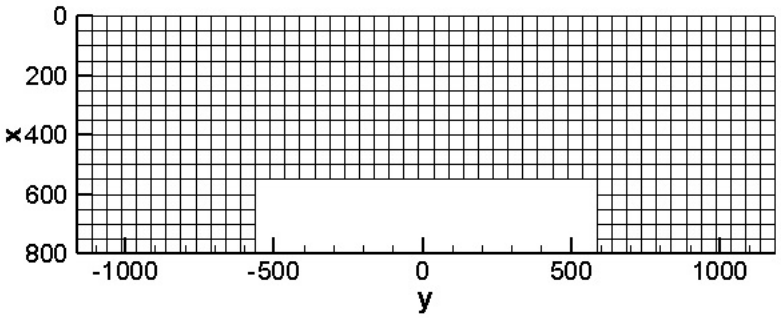

Figure 4.6: The blade-to-blade measuring plane.

Together with the near wake measurements, for the first time, in the experimental campaign of December 2016, the wake was investigated also along its streamwise evolution. This was possible thanks to the adoption of a 2D measuring plane perpendicular to the turbine axis, along the x-

y direction, only for the midspan traverse. Such measuring plane will be addressed as blade-to-blade plane (B2B), represented in Fig.4.6. For safety reasons, the experimental team decided to record the measurements in three different acquisition steps: the right-hand side, the downstream central zone, and the left-hand side. To adjust the three results on a single one, and hence to make them comparable, the velocity has been normalized on the undisturbed wind speed during data elaboration. The two lateral planes surrounding the rotor reach a minimum distance of around 110 mm from the machine blades, corresponding to a streamwise stroke of 800 mm. The central plane, instead, reaches a minimum distance from the rotor blades of 153 mm ($\approx 0.15D$), and 550 mm of streamwise stroke.

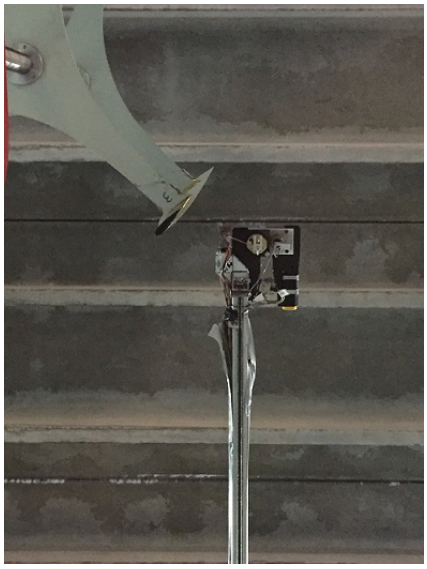

Figure 4.7: Relative position between probe and rotor during blade-to-blade tests.

The mesh transversal extension covers $2R$ on both the windward and leeward sides of the machine. For this second case, only the velocity magnitude and the yaw angles were investigated, since at midspan the pitch angle is reasonably expected to be close to zero. Hence, no slanted wire was used in the blade-to-blade plane measurements.

4.2 The GT Experimental Apparatus

4.2.1 The TC Test Rig

The test rig for the GT experimental campaign of winter 2017/18, was realized in the 1980's to carry out tests on variable geometry axial-flow turbine stage, in order to investigate fluid-dynamics and related phenomena in turbomachinery. The plant and the machine located inside it are designed to work in similarity conditions, to simulate the operation of larger-scale machines. It is interesting to note that the plant design is particularly versatile, in order to represent the widest range of operating conditions possible, without bringing about structural changes. The turbine stage section, where the present measurements wee carried out, was completely re-designed and commissioned in 2000.

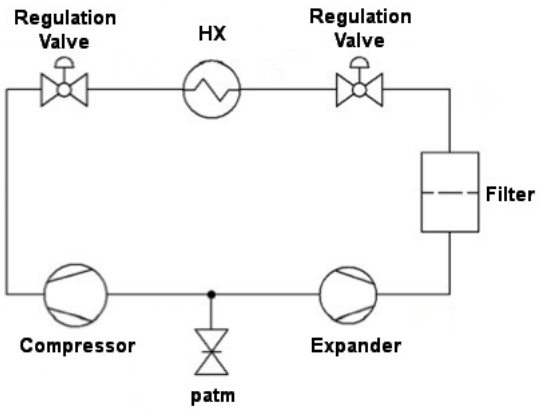

Figure 4.8: Simplified scheme of the TC test rig

A scheme of the main air ducts is reported in Fig.4.9 and 4.8, which is the same circuit in which the testing machines are installed. Already at first sight it is evident that the air is running in a closed circuit, with no fluid make-up, as it is instead for the calibration nozzle described in Ch.3. The plant is made of a centrifugal region, in which the radial compressor is located, and an axial one, in which the testing turbine is mounted. Instead of a turbine, depending on the testing requests, it is also possible to install an operating machine. The centrifugal compressor provides the desired pressure jump, pushing the air inside the S2 air-water heat exchanger. After this, the air mass flow rate is measured by means of a venturimeter, and regulated afterwards through two solenoid valves (EV2 and EV3). Successively, air gets filtered and enters the axial zone passing through

valve VF3. For the specific case of the campaign in question, in the axial region, a single expansion stage is installed, with a stator and a rotor. At the turbine discharge, the ejected air is then redirected again to the compressor intake. More complex configurations are made possible on this test rig without any structural change, and this is a great advantage that allows to study different machines in the axial region, or even the same centrifugal compressor, thanks to a by-pass section that keeps out the axial zone.

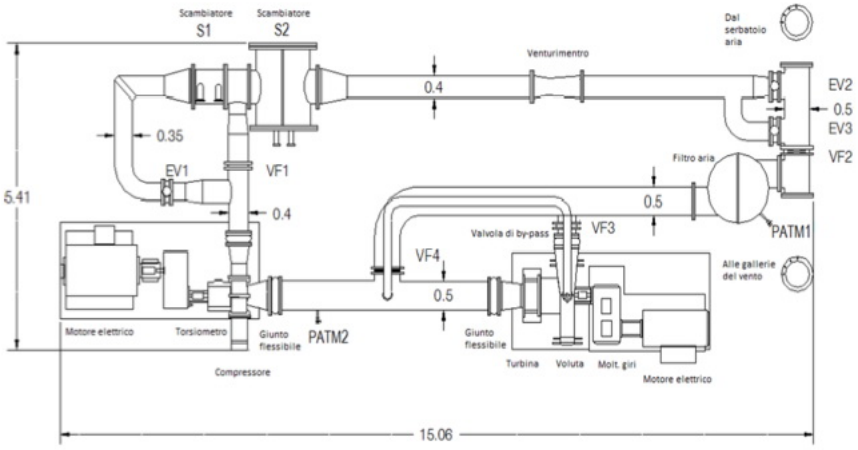

Figure 4.9: Scheme of the TC test rig

4.2.2 The Axia-Flow Turbine Stage

The machine to be tested is moved by a centrifugal compressor, able to run at a maximum speed of 18000 rpm, represented in Fig.4.10. Its aluminum alloy rotor has an external diameter of $D = 400\ mm$, is constituted of 16 blades and it is enclosed in a steel volute, represented in the same picture. Finally, the rotating part is mounted on the steel forged shaft. At the rotor discharge, a bladed diffuser is installed, for a better pressure recovery from the high velocity compressible fluid. The compressor is connected to an electric motor of 800 kW nominal power, and fed in constant current at a voltage of 600 V. The rotational speed of the compressor, as the one of the turbine, is measured by a pick-up placed on the machine shaft and it is commanded manually on the control panel.

On the other side of the plant, a high-pressure (HP) single-stage axial turbine is installed, characterized by a reaction degree of around $\chi = 0.3$, with 25 blades on the rotor and 22 on the stator, of the kind represented

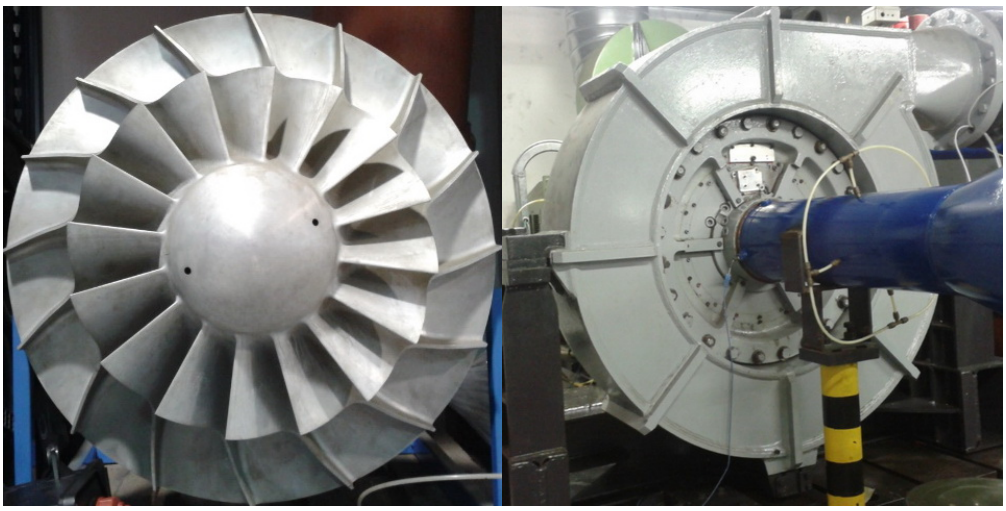

Figure 4.10: The centrifugal compressor.

in Fig.4.12, where the rotor blades twisting is evident. The machine can rotate at a nominal speed of 12 000 rpm, it has an external diameter of $D = 400$ mm and $b = 50$ mm of blade height. The turbine shaft is mounted on plain bearings, where oil leakages are prevented by means of carbon contacting seals. On the turbine casing, a steel tenon allows to insert the probe inside the turbine, and supports the sensor and its moving system.

The expander is finally connected to an electric generator, which applies a braking moment to the turbine shaft, acting then as a rotational speed regulator. The nominal power of such electric machine is 400 kW, fed at the voltage of 600 V. In-between, a four parallel axis gear train is installed (Fig.4.11). The turbine shaft rotational speed is measured by means of a pickup, as for the compressor, while the moment is measured with an interposed torque meter.

4.2.3 The GT Measuring Grid

The experimental campaign on the GT reported in the present work is part of a wider experimental research aimed at characterizing the fluid structures downstream of the statoric cascade of the axial turbine stage. Originally, both conventional five-hole probes and FRAPPs were applied, but HW measurements can be introduced as well, for two main reasons:

- The hot wire sensitive part can run along the blade span down to

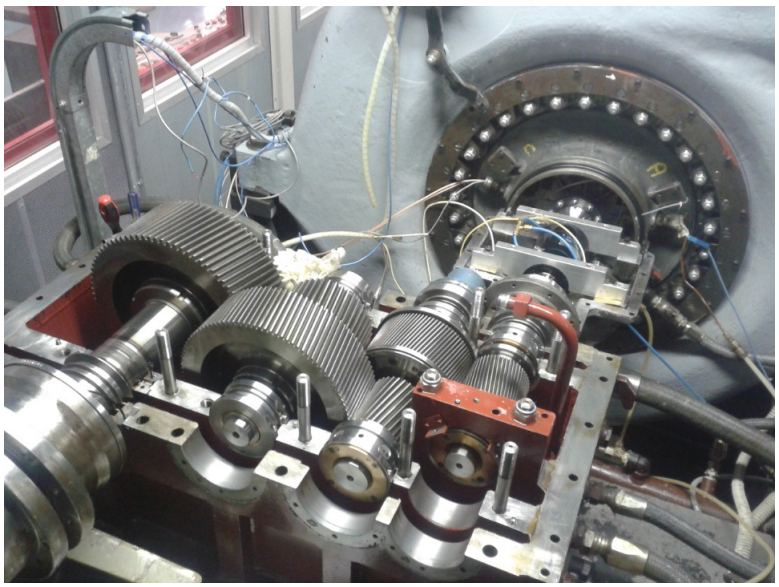

Figure 4.11: The four-axis gear train of the turbine.

the hub, and measure down to $r = 0\ mm$, where r is the radial coordinate that goes from the blade hub to the tip $r = b = 50\ mm$. In any case, this does not happen, since the wire is so delicate that it cannot touch the metal surface. Hence, the minimum radial measurement is taken at $r = 1.5\ mm$, but still it is much closer to the hub rather than the FRAPP measurements, which cannot go below $r = 5\ mm$ for constructive reasons.

- The FRAPP probe as well can be used for turbulence measurements, but the result is given in terms of turbulent fluctuations of total pressure. This means that the FRAPP cannot distinguish between fluctuations of the streamwise and crosswise velocities, and hence the Reynolds stess tensor cannot be derived, which is instead possible for the HW. Hence, it is useful to have an instrument, alternative to the FRAPP, to improve the accuracy of the measuring results.

Hence, in order to preserve a certain comparability between the two testing sessions, FRAPP and HW, the FRAPP measuring grid was maintained during the HW experiments, while three further circumferential traverses were added in the HW campaign, in order to capture the hub vortical structure. The region of interest for the present campaign is the wake that develops downstream of the stator, in the gap between stator and rotor. Hence, the measuring plane looks like the one shown in

Figure 4.12: Prototypes of the rotor blades on the left, and stator blades on the right.

Fig.4.13, covering one statoric pitch along the circumference, and with tighter traverses close to the extremities, tip and hub, where the vortical structures gather.

The probe is moved by two stepping motors, that provide it with two degrees of freedom, which are:

- Linear:
  Along the radial direction in the turbine reference frame.
- Rotational:
  Rotating the probe around its own axis.

The third degree of freedom of the measuring grid, instead, which is the shift along the channel pitch, is not provided by the probe moving system, but it is obtained by the rotation of the stator itself, for simplicity. The grid used in the HW testing campaign is then arranged in:

- Radial direction $\rightarrow$ 23 plunging positions in the range $[1.5 \;\; 50]$ mm from the hub.

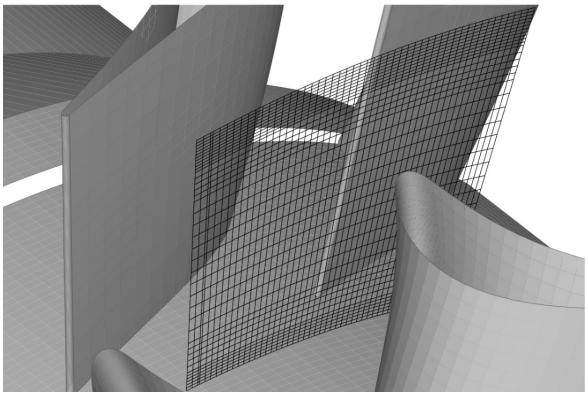

Figure 4.13: Example of a measuring plane in the stator/rotor gap.

- Tangential direction → 17 circumferential positions along one measuring traverse covering the whole channel pitch.

For every point of the measuring grid here above described and identified in Fig.4.14, the probe is rotated around its axis three times with values $[+45°\ \ 0°\ \ -45°]$ centered in the average flow direction.

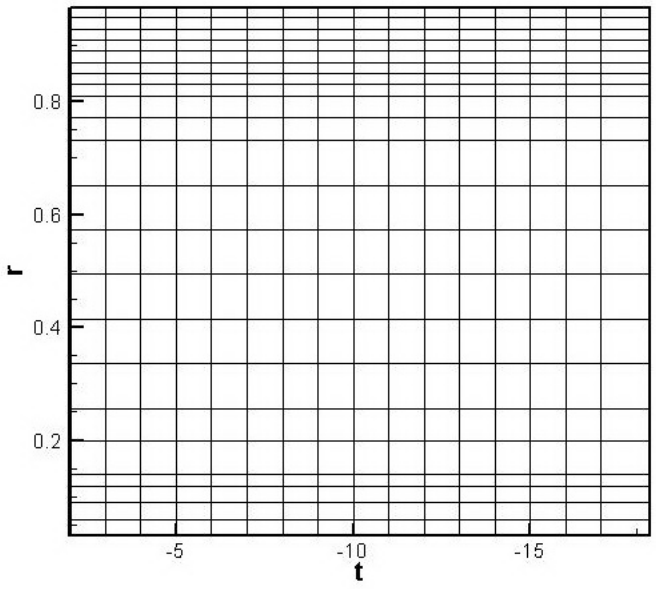

Figure 4.14: The measuring grid of the HW GT campaign.

Chapter 5

Data Processing

Despite the present work involves two different HW applications, the data elaboration procedures are quite similar, this is why they are presented together. Along this chapter, then, differences and analogies of the two cases will be put in evidence. The main topics that will be brought up in this chapter regard the numerical algorithms for:

- Yaw angle and velocity magnitude
- Pitch angle
- Turbulence intensity
- Reynolds stress tensor
- Turbulent length scales

Before starting to describe the numerical methods implemented for the elaboration of the experimental data, the reference frame adopted will be presented. The elaboration was carried out first with Matlab®, the more user-friendly programming language, and then with Fortran 90, in order to have the possibility to implement the codes in a bigger data elaboration software used by the Laboratory of Fluid Machines (LFM) group for experimental investigations in these fields.

5.1 The Reference Frame

Referring to the frame proposed in Chapter 2, where the wire reference system was presented, a correspondence between wire (relative) and machine (absolute) frames of reference has to be derived. Besides, this is

needed at this level of the elaboration in order to simplify the succeeding steps. The wire is in fact rotating around its axis during operation, and this means that the wire frame of reference changes with testing time. This situation, which is required for measuring reasons, as will be explained in the next lines, makes it necessary to work with an absolute frame of reference.

- Wire frame of reference (relative) $\rightarrow n, t, b$
- Machine frame of reference (absolute) $\rightarrow x_1, x_2, x_3$

A picture of the frame of reference is reported in Fig.5.1. It is also possible to address the components as:

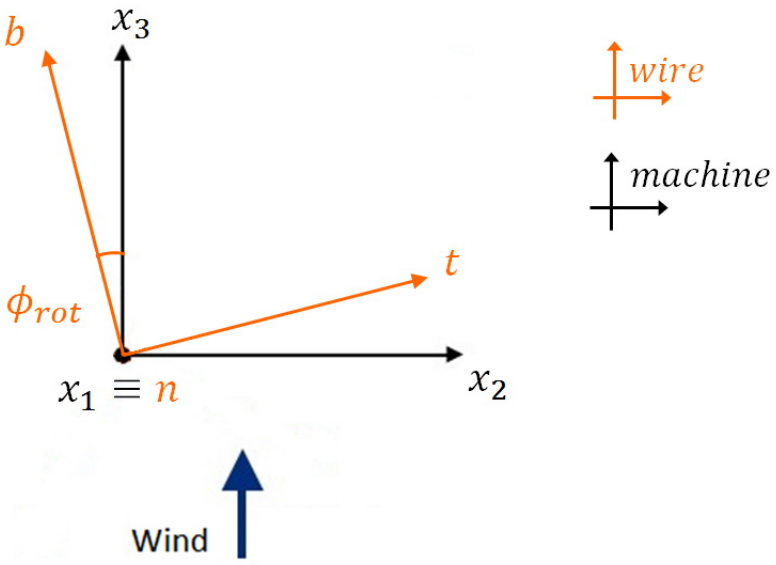

Figure 5.1: The wire and the machine reference frames.

- x-direction $\rightarrow$ Axis x_3, Velocity u_3 $\rightarrow$ VAWT: Streamwise; GT: Axial.
- y-direction $\rightarrow$ Axis x_2, Velocity u_2 $\rightarrow$ VAWT: Transversal; GT: Tangential.
- z-direction $\rightarrow$ Axis x_1, Velocity u_1 $\rightarrow$ VAWT: Longitudinal; GT: Radial.

Then, it is possible to project the absolute components of the velocity vector on the wire axes, to obtain the correlation between the two. The decomposition in the wire frame is the following, as reported in the calibration chapter (3).

$$\begin{aligned} U^2 &= U_n^2 + U_t^2 + U_b^2 == U_1^2 + U_2^2 + U_3^2 \\ U_n &= U\big(\sin\vartheta\cos\alpha + \cos\vartheta\sin\varphi\sin\alpha\big) \\ U_t &= U\big(\cos\vartheta\sin\varphi\cos\alpha - \sin\vartheta\sin\alpha\big) \\ U_b &= U\cos\vartheta\cos\varphi \end{aligned} \tag{5.1}$$

Where φ indicates the yaw flow angle, the one between the flow direction and the machine reference frame. This system of equations is the most complete form that can be derived, and it is the one implemented for the slanted probe in the VAWT campaign. Starting from these equations, some simplifications can be applied to the particular cases, and some terms will be consequently canceled out. These simplifications are the ones that follow:

1. VAWT Normal HW with pitch measurements $\rightarrow \alpha = 0°$.
2. GT Normal HW *without* pitch measurements $\rightarrow \alpha = 0°, \vartheta = 0°$.

To switch from this reference frame to the absolute one considering a possible rotation of the probe of an angle φ_{rot}, it should be noticed that:

$$\begin{aligned} U_n &= U_1\cos\alpha + U_2\sin\alpha\cos\varphi_{rot} + U_3\sin\alpha\sin\varphi_{rot} \\ U_t &= -U_1\sin\alpha + U_3\cos\alpha\sin\varphi_{rot} + U_2\cos\alpha\cos\varphi_{rot} \\ U_b &= U_3\cos\varphi_{rot} - U_2\sin\varphi_{rot} \end{aligned} \tag{5.2}$$

In the simplified form for the normal wire, where $\alpha = 0°$, eq. 5.2 becomes:

$$\begin{aligned} U_n &= U_1 \\ U_t &= U_3\sin\varphi_{rot} + U_2\cos\varphi_{rot} \\ U_b &= U_3\cos\varphi_{rot} - U_2\sin\varphi_{rot} \end{aligned} \tag{5.3}$$

Notice that here φ_{rot} is not the flow yaw angle, but it is the angle of rotation imposed to the probe around its axis during the test. Still, it is indicated with the Greek letter φ to remind that it is an angle in the b-t plane. This angle takes the actual value of the probe rotation for the slanted wire

and for the normal wire in GT operation $\varphi_{rot} = [+45°\ \ 0°\ \ -45°]$, while for the normal wire in the VAWT campaign, 90° should be added to the probe rotation, due to the different position between calibration and operation. Plugging the complete system of equations (eq.5.2) in the Jørgensen equation recalled below (eq.5.4), it is possible to obtain the Jørgensen equation in the machine frame in its most general form (eq.5.5).

$$Q^2 = U_n^2 + k^2 U_t^2 + h^2 U_b^2 \tag{5.4}$$

$$\begin{aligned} &= \Big(U_1 \cos\alpha + U_2 \sin\alpha \cos\varphi_{rot} + U_3 \sin\alpha \sin\varphi_{rot} \Big)^2 + \\ &+ k^2 \Big(-U_1 \sin\alpha + U_3 \cos\alpha \sin\varphi_{rot} + U_2 \cos\alpha \cos\varphi_{rot} \Big)^2 + \\ &+ h^2 \Big(U_3 \cos\varphi_{rot} - U_2 \sin\varphi_{rot} \Big)^2 \end{aligned} \tag{5.5}$$

Developing eq.5.5, it is possible to write the Jørgensen equation in the following wrapped form:

$$Q^2 = A_{11}U_1^2 + A_{22}U_2^2 + A_{33}U_3^2 + 2A_{12}U_1U_2 + 2A_{13}U_1U_3 + 2A_{23}U_2U_3 \tag{5.6}$$

Where the coefficients A_{ij}, addressed as Jørgensen coefficients, assume the values:

$$\begin{aligned} A_{11} &= \cos^2\alpha + k^2 \sin^2\alpha \\ A_{22} &= \cos^2\varphi_{rot}(\sin^2\alpha + k^2\cos^2\alpha) + h^2 \sin^2\varphi_{rot} \\ A_{33} &= \sin^2\varphi_{rot}(\sin^2\alpha + k^2\cos^2\alpha) + h^2 \cos^2\varphi_{rot} \\ A_{12} &= \frac{\sin 2\alpha}{2} \cos\varphi_{rot}(1-k^2) \\ A_{13} &= \frac{\sin 2\alpha}{2} \sin\varphi_{rot}(1-k^2) \\ A_{23} &= \frac{\sin 2\varphi_{rot}}{2}(\sin^2\alpha + k^2\cos^2\alpha - h^2) \end{aligned} \tag{5.7}$$

The unknowns of eq.5.6 are the three velocity components, or alternatively the velocity magnitude and the two flow angles. Hence, to solve the complete problem, at least three equations are necessary. Two of these equations should be provided by the normal wire, since this is sensitive just to the binormal and transversal components U_2 and U_3, while the third equation is obtained by the slanted wire, and solves U_1, the longitudinal velocity. In reality, since the present work is discussing experimental data,

it is in general preferable to over-constrain the problem, and to adopt a least-squared error procedure to elaborate and analyze the data. Hence, three rotations corresponding to three Jørgensen equations were applied to the normal probe, and the same was done for the slanted wire as well. In the next chapters, evidence of the improvement of the over-constrained problem compared to the square system will be given, as well as evidence of no particular improvement of the solution using more than three equations for each probe. Increasing the number of rotations increases a lot the duration of the test, and hence it is important to find a trade-off between testing time and accuracy of the results.

The resolution of the system of Jørgensen equations is in any case not trivial, since also the yaw and pitch factors k and h are functions of the flow angles themselves, which are unknown. Hence, the system is strongly non-linear and requires an iterative procedure. For sake of simplicity, for the VAWT campaign, in which also the pitch angle is of interest, the resolution of the problem was split in two:

1. The flow magnitude and the yaw angle are solved using only the information given by the normal wire and keeping the longitudinal velocity U_1 constant.

2. Keeping constant the results of the normal wire, which are yaw angle and velocity magnitude, the velocity U_1 is derived using the slanted wire measurements. The pitch angle is then computed, and the velocity magnitude updated as a consequence. These latter values will be used to restart the iteration.

This way of proceeding is then explained in detail in sections 5.4 and 5.5. For the GT campaign, instead, zero pitch angle was assumed, no slanted wire was adopted, and hence the resolution procedure stops at the first bullet.

5.2 Velocity Normalization

The aerodynamic tests in the wind tunnel and on the axial-flow turbine test rig have quite a long duration, from one to two hours. During such a long interval of time, the velocity rating conditions are not necessarily respected. On the other hand, it is useful to refer the whole test to a certain fixed undisturbed wind velocity, and hence the instantaneous data have to be normalized in order to be comparable one to another. During VAWT tests, for instance, the velocity has been normalized on the basis of

the dynamic pressure at the wind tunnel nozzle outlet. Hence, any wind tunnel velocity is made non-dimensional with respect to the instantaneous undisturbed wind speed, considering the following formula:

$$V_{i,ad} = \frac{V_i}{V_{i,0}} \tag{5.8}$$

Where V_i stands for any velocity measured during the test, and $V_{i,0}$ is the undisturbed wind speed measured at the same instant of time. On the basis of this definition, in the regions of the measuring grid in which the flow remains undisturbed, and hence outside of the wake, the dimensionless velocity is $V_{i,ad} = 1$. In VAWT wind tunnel measurements, usually, the presence of the turbine alters the flow by reducing its kinetic energy. This means that the turbine wake, in its usual operating point, is expected to present $V_{i,ad} < 1$. Instead, properly speaking, this is not always true. As will be shown in the results discussion section dedicated to the VAWT, there are wake regions close to the turbine trace ($y/R = \pm 1$), in which $V_{i,ad} > 1$. This overspeed zone is due to the presence of the turbine itself, as a consequence of its solid structure and of its fast rotation. This effect is greater as the turbine solidity increases, of course, but also as the turbine rotational speed gets higher with respect to the wind speed, and hence for low wind velocities and for high λ [6].

To give an example of how the undisturbed wind velocity can change during the wind tunnel test, the following example for two different traverses has been reported in Fig.5.2.

5.3 Numerical Methods

For the strong non-linearity of the system of equations involved, the procedure that allows to solve the problem cannot be analytical, but it has to be iterative. Inside the algorithm, the resolution of the system of Jørgensen equations is just a step of the whole iterative procedure, and this can be carried out in several ways, as there are many algorithms that solve systems of non-linear equations. For simplicity, only two methods were chosen to elaborate the data, and a comparison between the two is then carried out.

- Newton-Raphson: Numerical method for the resolution of an iso-constrained square system of equations.
- Levenberg-Marquardt: Numerical method for the resolution of an over-constrained system of equations on the basis of the least-squared

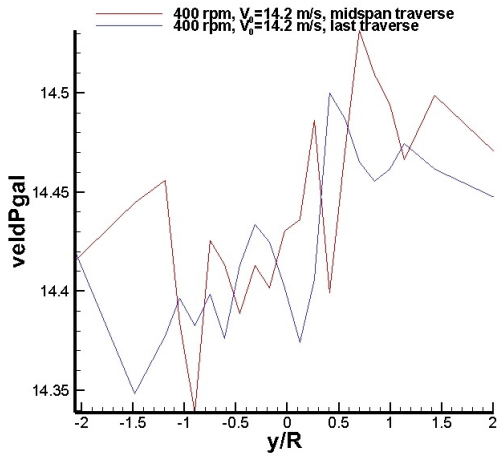

Figure 5.2: The undisturbed wind speed fluctuation on two different traverses of the H-Darrieus turbine during wind tunnel test. Turbine rotational speed is 400 rpm and rated speed is $V_0 = 14.2\ m/s$.

error approach.

5.3.1 Newton-Raphson

The Newton-Raphson (NR) is a numerical method that allows to compute the zeros of a function, but the method can be also extended to systems of equations, which is the core of the numerical procedure presented in this chapter. As every numerical method, also the NR method has to be given a starting point, usually addressed with the notation x_0, and it stops when a tolerance is satisfied. If a single variable function is considered, the solution at the first iteration is:

$$x^{(1)} = x_0 + \frac{f(x_0)}{f'(x_0)} \tag{5.9}$$

Where $f(x_0)$ is the value of the function f at the starting point x_0, and $f'(x_0)$ is the value of its first derivative evaluated again at x_0. In general, eq.5.9 for the k-th iteration becomes:

$$x^{(k+1)} = x^{(k)} + \frac{f(x^{(k)})}{f'(x^{(k)})} \tag{5.10}$$

At the end of each iteration $k+1$, an error is computed, which is the difference in absolute value between the function at iteration $k+1$, and

its value at the previous iteration.

$$\varepsilon = |f(x^{(k+1)}) - f(x^{(k)})| \tag{5.11}$$

The value of the tolerance is decided at the beginning of the iterative procedure, and convergence is reached when:

$$\varepsilon < tol \tag{5.12}$$

If more unknowns are involved in the problem, and the equation becomes a system of equations, as it actually is for the Jørgensen problem, it is still possible to apply the NR method, to a system of functions that are described as:

$$f = f(x_1,\ x_2,\ \dots\ ,\ x_i,\ \dots\ ,\ x_n) = f(\overline{x}) \tag{5.13}$$

From now on, it is necessary to move to the vectorial notation, where $\overline{F}$ represents the vector of functions, and its first derivative is replaced by the Jacobian matrix J, which is the matrix of the partial derivatives of the functions $\overline{F}$ in the n variables.

$$\overline{F} = \begin{bmatrix} f_1 \\ f_2 \\ \dots \\ f_i \\ \dots \\ f_n \end{bmatrix}; \quad J = \begin{bmatrix} \frac{\partial f_1}{\partial x_1} & \frac{\partial f_1}{\partial x_2} & \dots & \frac{\partial f_1}{\partial x_i} & \dots & \frac{\partial f_1}{\partial x_n} \\ \frac{\partial f_2}{\partial x_1} & \frac{\partial f_2}{\partial x_2} & \dots & \frac{\partial f_2}{\partial x_i} & \dots & \frac{\partial f_2}{\partial x_n} \\ \dots & & & & & \dots \\ \frac{\partial f_i}{\partial x_1} & \frac{\partial f_i}{\partial x_2} & \dots & \frac{\partial f_i}{\partial x_i} & \dots & \frac{\partial f_i}{\partial x_n} \\ \dots & & & & & \dots \\ \frac{\partial f_n}{\partial x_1} & \frac{\partial f_n}{\partial x_2} & \dots & \frac{\partial f_n}{\partial x_i} & \dots & \frac{\partial f_n}{\partial x_n} \end{bmatrix}$$

Therefore, the solution to the current iteration is:

$$\overline{x} = \overline{x}_0 + [J]^{-1}\overline{F} \tag{5.14}$$

In the present work, if pitch angle is considered, three velocity components have to be evaluated, and hence the variables are U_1, U_2 and U_3. Otherwise, in case no pitch is considered, only two components are of interest, which are U_2 and U_3, since U_1 is set to zero. In both cases, as it will be explained deeply in the next lines, yaw and pitch angles calculations are decoupled, and hence, in any case, no more than two velocity components are computed at a time. Here below, the vector of functions and the Jacobian matrix are reported for the specific case:

$$\overline{F} = \begin{bmatrix} f_1(U_2, U_3) \\ f_2(U_2, U_3) \end{bmatrix}; \quad J = \begin{bmatrix} \frac{\partial f_1}{\partial U_2} & \frac{\partial f_1}{\partial U_3} \\ \frac{\partial f_2}{\partial U_2} & \frac{\partial f_2}{\partial U_3} \end{bmatrix}$$

The solution to the current iteration is then:

$$\overline{U} = \begin{bmatrix} U_2 \\ U_3 \end{bmatrix} = \overline{U}_0 + [J]^{-1}\overline{F}$$

The subscripts 1 and 2 of the functions f indicate the two Jørgensen equations written for the two different angular positions in which the HW data are collected. These two positions can be either $\varphi_{rot} = [+45° \quad 0°]$, $\varphi_{rot} = [+45° \quad -45°]$ or $\varphi_{rot} = [0° \quad -45°]$. Among the three different combinations, the second one seems to give the best results, if compared with the least-squared methods carried out in the following chapter.

Notice that the NR method cannot be run if the Jacobian is a singular matrix. Besides, if the starting point x_0 is too far from the actual solution, the method may not converge. For this reason, during elaboration, a variant of the NR method was used, already implemented in the Matlab® library, called the Trust-Region Dogleg method. This solution is pursued by adopting a non-linear equation solver of Matlab®, called *fsolve*, by correctly adjusting the routine options.

5.3.2 Levenberg-Marquardt

The non-linear over-constrained system of equations is solved by means of the Levenberg-Marquardt algorithm (LMA). This is a method used to solve over-constrained problems with the least-squared approach. This kind of procedure is recommended since, typically, experimental sets of data are elaborated solving over-constrained systems of equations. The objective of the algorithm is to fit the experimental data on a well known function, that in our case is the Jørgensen equation, and to calculate its functional parameters, A_{ij} in the case of the HW tests, such that the squared distance of the data points from the fitting curve is minimum. This procedure as well is iterative and it recomputes the function parameters A_{ij} iteration by iteration until the summation of the squared errors is minimized.

The LMA is actually the combination of two minimization methods: the gradient descent algorithm and the Gauss-Newton algorithm. In particular, in the gradient descent method the sum of the squared errors

is continuously reduced by updating the parameters going towards the steepest descent direction. When a lot of parameters are involved in the system of equations, the gradient descent method is one of the most robust algorithms, meaning that it is one of the few approaches that lead to convergence and find out the solution not depending on the starting point. The Gauss-Newton method, instead, works on the principle of minimizing the sum of the squared errors assuming that the function is locally quadratic, and looking for its minimum.

Moreover, when the parameters are far from the real solution, the LM algorithm seems to behave more as a gradient descent algorithm. When the parameters, instead, are closer to the real optimized ones, the LMA behaves more as a Gauss-Newton method. This flexibility of the LMA makes the method definitely more robust than the Gauss-Newton, which means that it will find a solution to the problem more easily than implementing the Gauss-Newton method alone, even if the starting point is far from the solution.

As already mentioned in the previous lines, the least-square problems consists in minimizing a function f that is the sum of the squared errors:

$$\min_x f(x) = ||F(x)||_2{}^2 = \sum_i F_i^2(x) \tag{5.15}$$

The LMA looks for the minimum in a precise direction, which is a solution of the following set of equations:

$$(J(x_k)^T J(x_k) + \lambda_k I)d_k = -J(x_k)^T F(x_k) \tag{5.16}$$

Where λ_k controls both magnitude and direction of d_k. Small values of it result in the update of the Gauss-Newton, while large values correspond to an update of the gradient descent method. The parameter λ_k is initialized large in such a way that the first updates are small in the steeper descent direction. When $\lambda_k = 0$, the direction d_k is identical to that of the Gauss-Newton method. As $\lambda_k \to +\infty$, the direction d_k tends to the steepest descent direction, while the magnitude tends to zero. This means that there is a sufficiently large value of λ_k, for which the relation $(x_k + d_k) < F(x_k)$ holds true.

5.4 The Algorithm for Velocity Magnitude and Yaw Angle

In the present section, the algorithm for the data elaboration of the normal probe is presented. The results of this procedure are the velocity

magnitude and the yaw angle, or, alternatively, the two velocity components U_2 and U_3, while the velocity U_1 is kept constant. The code was wrote first in Matlab®, and then transposed in Fortran 90 to be implemented in the LFM software. The starting point of the iterative procedure is the following:

$$U_1 = 0$$
$$U_2 = 0$$
$$U_3 = Q$$

Which, rewritten in terms of velocity magnitude and flow angles is:

$$Q = V$$
$$\vartheta = 0$$
$$\varphi = 0$$

Where Q is the cooling velocity felt by the wire, and V is the real velocity magnitude. This combination of the three velocity components corresponds to a situation in which the velocity is laying just along the streamwise direction. This is a good starting point for the iterative procedure, since it is intuitive that with a first approximation the main velocity component is the streamwise one. This holds true both for the VAWT and for the GT, even if the flow in axial turbomachinery can be strongly deflected towards the tangential. In any case, to improve the measurement sensitivity also in the GT case, during the test, the probe was pre-rotated of 75° in order to directly face the main flow direction. As a matter of fact, the 75° value was already known from previous campaigns, before the use of the HW. The whole elaboration is carried out with the wire voltages as they are, the pre-rotation angle is then added to the result a posteriori. In any case, this is just a first attempt approximation, that allows the iterative procedure to positively lead to the expected solution. Moreover, the conditions on U_1 and U_2 make the third equation more reliable, since Q is calculated with the King's law, and this is defined for both yaw and pitch angles equal to zero. This is just the problem initialization procedure, and it has been repeated for every point of the measuring grid, at the beginning of every yaw angle elaboration.

The following is the loop procedure itself, which involves three phases:

- Interpolation. By means of the first attempt values of velocity and flow angles, the pitch and yaw coefficients can be computed for the specific iteration. The computation is done interpolating on the

closest values in the calibration matrix, derived in the calibration chapter (Ch.2). In this phase, for the calculation of the yaw coefficient k^2 a double interpolation is needed, on velocity and pitch, while the calculation of h requires a triple interpolation, since this coefficient depends also on yaw, together with velocity and pitch. For both cases, a linear interpolation in sufficiently accurate for the purpose.

- Jørgensen coefficients calculation. In the second step, the coefficients A_{ij} described in section 5.1 are calculated as reported in the same chapter. Six coefficients are computed for every Jørgensen equation involved, and hence for every probe rotation around its axis. For the normal HW, eq.5.6 can be simplified setting $\alpha = 0°$. Please notice that the coefficients A_{ij} are functions of h and k^2, and hence they change iteration by iteration, but within the single step of the procedure they act as constants.

- Jørgensen system of equation solving. The third and last phase is the resolution of the system of Jørgensen equations by means of either of the two numerical methods described in section 5.1. The NR method was solved by means of the function *fsolve*, while the LMA was implemented with the *lsqnonlin* function, both already present in the integrated Matlab® library. For the Fortran 90 transposal, instead, only the overconstrained problem was implemented, since it was proved to be by far more accurate. The unknowns of this system of equations are the two velocity components U_2 and U_3, while U_1 is kept constant and equal to its initial value.

The resolution of the system of Jørgensen equations ends up with two values of U_2 and U_3, and plugging them together it is possible to compute the yaw angle, but also the velocity magnitude:

$$\varphi = \arctan \frac{U_2}{U_3}$$
$$V = \sqrt{U_2^2 + U_3^2}$$

Then, the deviation from the previous iteration value is computed just for the yaw angle, since the ratio of the components is more significant than the one of the two velocity terms alone. This is then compared to a tolerance, set at the beginning of the iterative procedure, and if the condition is respected, the method has reached convergence.

$$\varepsilon = |\varphi - \varphi_0| < tol$$

Usually, to help convergence, a relaxation factor is adopted. In this case the relaxation is $\xi = 0.1$, and convergence is reached with a tolerance of $tol = 10^{-2}$. The starting point of the next iteration is then:

$$U_{i,0}^{(k+1)} = \xi U_i^{(k+1)} + (1 - \xi) U_i^{(k)}$$

The convergence of the iterative method is proved by the progressive reduction of the error ε down to values lower than the imposed tolerance.

5.5 The Algorithm for Pitch Angle

The second part of the flow components algorithm is the one that determines the pitch angle, or alternatively, the U_1 velocity term, which is the longitudinal velocity for the VAWT case. This part of the algorithm was implemented just for the VAWT by means of the slanted probe measurements, while in the GT the radial component of velocity is neglected ($U_1 = 0\ m/s$). Thanks to this further information, a fully time-resolved characterization of the three velocity components should be made possible. The algorithm is structured in a way that strongly resembles the one for yaw angle and velocity magnitude discussed in Sec.5.4. This procedure uses the results of the yaw and velocity magnitude algorithm as constants.

The reader should recall that for testing time reasons, the normal and the slanted probe measurements were taken simultaneously, but in a different spatial position. Hence, the velocity corresponding to the slanted probe position is not properly the one measured by the normal wire, and to approximate that value, a linear interpolation in space is performed on the two velocity components U_2 and U_3. This operation allows to pass from the normal to the slanted hot wire reference, and also to compute again the velocity magnitude and the yaw angle in the new frame.

$$\varphi = \varphi_S = const_1$$
$$V = V_S = const_2$$

On the basis of these, the coefficients k and h are computed by means of double and triple interpolation, exactly as described in Sec.5.4. Then, these factors are used to compute the A_{ij} coefficients of the Jørgensen equation, for which the general case with $\alpha = 45°$ has to be considered now. For this case as well, three rotations are applied to the slanted probe, and hence three different equations are available for only one unknown, which is the velocity component U_1. Since it can be shown that an overconstrained problem gives more accurate results, all the three equations have been used, and hence the LMA algorithm implemented in the

lsqnonlin Matlab function is the only way to solve the problem. The result obtained by the solution of this algorithm is a velocity component, that allows to calculate the pitch angle and to update also the value of the velocity magnitude.

$$\vartheta = \arctan \frac{U_1}{U_3}$$
$$V = \sqrt{U_1^2 + U_2^2 + U_3^2}$$

Notice that the algorithm described in this chapter until now, is not an iterative procedure if considered alone, but it is part of a greater iterative cycle that runs in sequence the yaw and velocity iterative algorithm, and the slanted data elaboration. The reader should in fact notice that the output results of this algorithm, end up updating the first attempt values of the yaw elaboration, which are zero longitudinal velocity component which means zero pitch angle.

On this algorithm, improvements have been applied to the original procedure [7]. It is in fact possible to set up an external iterative loop, whose first attempt hypotheses are those of the yaw algorithm, and the final output is that of the pitch algorithm. A check is then made on the pitch angle, and the starting point of the succeeding iteration will be the yaw angle coming from the algorithm in sec.5.4, and the pitch angle together with the velocity magnitude resulting from the procedure discussed in this section. The error is still evaluated the same way, and in this case as well a relaxation factor is recommended to help convergence.

$$\varepsilon = |\vartheta - \vartheta_0| < tol$$
$$\vartheta_0^{(k+1)} = \xi\vartheta^{(k+1)} + (1-\xi)\vartheta^{(k)} \qquad \text{where} \quad \xi = 0.1$$

5.6 Turbulence Basic Statistics

In the present section, the basic statistics to investigate turbulence are presented. Turbulence measurements are interesting on the GT side to be compared with the FRAPP, while for the VAWT they are useful to achieve a higher knowledge of the wake aerodynamics, which is rather complex for this kind of turbine. For this reason, a deeper description on the turbine flow unsteadiness is required. Periodicity is a core characteristic of turbomachinery flows, and for the specific case, this applies to both the VAWT and the GT stator, even if in two radically different ways:

- VAWT: The wake downstream of a rotor is being considered. Hence, periodicity will develop in time. Periodic unsteadiness is fairly high.

- GT: The wake downstream of a stator is being considered. A steady state flow is running over a stationary component. Hence, in the stator flow, there is no precise source of eterministic unsteadiness. The rotor, instead, gives rise to a periodic pressure distribution that in subsonic flow conditions is able to propagate also upstream of the rotor blade leading edge itself. Hence, there is a time-periodic trend in the axial stage stator wake as well, but this is definitely much weaker.

To have a deeper understanding of the wake characteristics, the unsteady data elaboration was performed. In the present paragraph, several statistics on the instantaneous data are applied. The first step is represented by a phase-lock elaboration. This consists in matching together the measured data on the basis of the encoder circumferential position at which they have been captured. The "phase" in question regards hence the angular position of the pick-up encoder with respect to a reference. This instrument is required exactly for this purpose, it is able to detect when the shaft passes a certain position with high precision, and hence it is considered a reference for the phase-lock analysis. This instrument is essentially an eddy current proximity sensor which detects a variation of the distance between a sensitive element located on the blade, and a metallic plate positioned on the shaft, producing an output voltage. To perform the phase-lock analysis, this time only for the VAWT, the first step is to divide the signal over the revolution in n segments as the number of blades of the machine, which are 3 in this case. This first procedure allows to assign a revolution phase to each measurement. The measured signals are necessarily characterized by electrical noise. Hence, a validation procedure based on the rated rotational speed should be implemented, to avoid that electrical spikes are mistaken with a blade passage. Besides, the flow is not homogeneous inside a single rotor phase, and hence, to obtain a good trade-off between results accuracy and computational effort, each phase was discretized in 40 sub-intervals per Blade Passing Period. As a matter of fact, the blade circumferential extension of the VAWT is around 10°, while one of the forty intervals of one blade period covers only 3°. This means that the discretization is particularly accurate, since the same blade is captured three times during the same period. After the phase-lock procedure, the next step is the triple decomposition [5]. This allows to split the unsteady velocity in three components:

- $V_{TM}(\overline{X}) \rightarrow$ Time mean velocity component.
- $V_{PER}(t, \overline{X}) \rightarrow$ Periodic phase-resolved velocity component.
- $V_{TU}(t, \overline{X}) \rightarrow$ Turbulent velocity component.

Where $\overline{X}$ represents the vector of the spatial position. These three velocity components are combined as follows to form the instantaneous velocity measurement:

$$V(t, \overline{X}) = V_{TM}(\overline{X}) + V_{PER}(t, \overline{X}) + V_{TU}(t, \overline{X}) \tag{5.17}$$

The periodic component is computed by means of the concept of ensemble averaging, while for the time mean, a simple time average is required. Notice that each revolution period is divided into a number of intervals that it is justified by the fundamental period of periodic unsteadiness, namely the Blade Passing Period (BPP).

$$BPP = \frac{60}{nN} \tag{5.18}$$

Where n is the rotor angular speed, and N is the number of blades of the machine in question. During one sampling record, a certain number of Blade Passing Periods is registered (N_{BPP}). Then, a certain time resolution Δt is defined in order to discretize each BPP in a N_{PER} number of intervals, such that $BPP = \Delta t \times N_{PER}$. Hence, the sampling can be reformulated as:

$$t = t(i, j) = \left(\frac{j}{N_{PER}} + (i - 1) \right) BPP \tag{5.19}$$

Where i spans all the BPPs from 1 to N_{BPP}, while j is the index of each phase within a certain BPP, going from 1 to N_{PER}. Hence, it is possible to rewrite eq.5.17 in a form in which time t is discretized, and expressed with the coordinates (i, j):

$$V(i, j, \overline{X}) = V_{TM}(\overline{X}) + V_{PER}(j, \overline{X}) + V_{TU}(i, j, \overline{X}) \tag{5.20}$$

The time-mean velocity component is simply computed as an arithmetic average of all the available measurements:

$$V_{TM}(\overline{X}) = \frac{\sum_{i=1}^{N_{BPP}} \left(\sum_{j=1}^{N_{PER}} V(i, j, \overline{X}) \right)}{N_{BPP} N_{PER}} \tag{5.21}$$

The phase-resolved periodic component of velocity, instead, depends only on the time interval related to a BPP, which means that it is periodic with the passing period alone as a fundamental period. For this reason, it is independent of the index i, and it is computed as an ensemble average among the values belonging to the same phase measurement, and hence with the same j index for all BPPs, to which the time-mean value is subtracted:

$$V_{PER}(j,\overline{X}) = \frac{\sum_{i=1}^{N_{BPP}} \left(V(i,j,\overline{X}) - V_{TM}(\overline{X}) \right)}{N_{BPP}} \tag{5.22}$$

Finally, the turbulent component of velocity, which varies instantaneously and hence depends on both indices (i,j), can be derived simply subtracting the periodic and the time-mean terms from the instantaneous measurement, as described in eq.5.20.

$$V_{TU}(i,j,\overline{X}) = V(i,j,\overline{X}) - \left(V_{TM}(\overline{X}) + V_{PER}(j,\overline{X}) \right) \tag{5.23}$$

The flow statistics can be applied then to the velocity components resulting from the triple-decomposition described above, in order to extract information of the wake character. First, the periodic unsteadiness is computed as the root-mean-square (RMS) of the periodic component of velocity (V_{PER}). This is the unsteadiness caused by the blade revolution, made dimensionless with respect to the undisturbed incoming wind velocity:

$$I_{PER}(\overline{X}) = \frac{1}{V_0} \sqrt{\frac{\sum_{j=1}^{N_{PER}} (V_{PER}(j,\overline{X}))^2}{N_{PER}}} \tag{5.24}$$

This quantity I_{PER} carries all the information regarding how deterministic unsteadiness impacts on the wake. Finally, turbulent intensity is defined as the ratio between the standard deviation of the velocity fluctuations and the incoming flow velocity. Such standard deviation is also called root-mean-square value (RMS), and it is computed as: [8]

$$V_{RMS}(j,\overline{X}) = \sqrt{\frac{\sum_{i=1}^{N_{BPP}} \left(V(i,j,\overline{X}) - V_{PER}(j,\overline{X}) \right)^2}{N_{BPP}}} \tag{5.25}$$

And hence the turbulence intensity is the following, usually expressed as a percentage.

$$I_{TU}(j,\overline{X})\ [\%] = \frac{V_{RMS}(j,\overline{X})}{V_0(\overline{X})} \times 100 \tag{5.26}$$

Please note that the RMS value addressed in eq.5.25 is not so straightforward to obtain. It is easy to derive the fluctuation of the cooling velocity, but to obtain the one for the flow velocity magnitude it is necessary to pass by the Reynolds stress tensor, which is discussed in the next section.

5.7 The Algorithm for the Reynolds Stress Tensor

To describe the determination of the Reynolds Stress tensor, a step backwards has to be made. Turbulence can be investigated only by splitting the flow quantities in an ensemble-average component and the fluctuation around such average. This is the so called *Reynolds decomposition*. Please note that with reference to the algorithms reported in the previous section, such average is the sum of the time-mean and the periodic component.

$$X = \overline{x} + x'$$

Where X is a generic quantity, $\overline{x}$ represents the ensemble-average term, and x' is the fluctuation around it.

The cooling velocity is related to the flow directions by means of the Jørgensen equation, reported here below in the wire reference frame:

$$Q^2 = U_n^2 + k^2 U_t^2 + h^2 U_b^2 \tag{5.27}$$

As already mentioned in sec.5.1, the Jørgensen equation (eq.5.27) can be rewritten as a function of the three velocity components in the machine absolute frame of reference (eq.5.6). In this section a further step is proposed, which is the introduction of the Reynolds decomposition of the three velocity components. Recall the reference frame:

- $U_1 \rightarrow$: radial/longitudinal velocity for GT/VAWT respectively
- $U_2 \rightarrow$: crosswise tangential velocity
- $U_3 \rightarrow$: streamwise velocity, main flow direction

Then, recall the Jørgensen equation in the machine reference frame:

$$Q^2 = A_{11}U_1^2 + A_{22}U_2^2 + A_{33}U_3^2 + 2A_{12}U_1U_2 + 2A_{13}U_1U_3 + 2A_{23}U_2U_3 \quad (5.28)$$

Where the A_{ij} coefficients are reported in eq.5.1, which depend on the slant angle α, on yaw and pitch coefficients k^2 and h, and on the angle of rotation of the probe around its axis φ_{rot}. Introducing in eq.5.28 the Reynolds decomposition, isolating the purely streamwise velocity term $\overline{u_3}^2 A_{33}$ and extracting the square root of both members, with a few algebraic passages, the Jørgensen equation can be rewritten in the form that follows:

$$\begin{aligned} Q = \sqrt{A_{33}}\overline{u_3}\Bigg[1 &+ \frac{2u_3'\overline{u_3} + u_3'^2}{\overline{u_3}^2} + \frac{A_{11}}{A_{33}}\frac{\overline{u_1}^2 + 2u_1'\overline{u_1} + u_1'^2}{\overline{u_3}^2} + \\ &+ \frac{A_{22}}{A_{33}}\frac{\overline{u_2}^2 + 2u_2'\overline{u_2} + u_2'^2}{\overline{u_3}^2} + 2\frac{A_{13}}{A_{33}}\frac{\overline{u_1u_3} + u_1'\overline{u_3} + \overline{u_1}u_3' + u_1'u_3'}{\overline{u_3}^2} + \\ &+ 2\frac{A_{12}}{A_{33}}\frac{\overline{u_1u_2} + \overline{u_1}u_2' + u_1'\overline{u_2} + u_1'u_2'}{\overline{u_3}^2} + \\ &+ 2\frac{A_{23}}{A_{33}}\frac{\overline{u_2u_3} + u_2'\overline{u_3} + \overline{u_2}u_3' + u_2'u_3'}{\overline{u_3}^2}\Bigg]^{0.5} \end{aligned} \quad (5.29)$$

Introducing the probe in such a way that the axis x_1 is perpendicular to the main flow direction, and the axis x_3 corresponds to the main flow direction itself, the time-mean velocity components $\overline{u_1}$ and $\overline{u_2}$ are very small compared to those in the main flow direction $\overline{u_3}$. It is then possible to perform a binomial series expansion at the second order, neglecting hence the quadratic velocity fluctuations terms, and the result is:

$$\overline{q} + q' = \sqrt{A_{33}}\overline{u_3}\left[1 + \frac{u_3'}{\overline{u_3}} + \frac{A_{13}}{A_{33}}\frac{u_1' + \overline{u_1}}{\overline{u_3}} + \frac{A_{23}}{A_{33}}\frac{u_2' + \overline{u_2}}{\overline{u_3}}\right] \quad (5.30)$$

This is evidently a linear equation, and for this reason it can be decomposed in two other equations, containing respectively the time-mean velocities and their fluctuations. The one for velocity fluctuations is the following:

$$q' = \sqrt{A_{33}}\overline{u_3}\left[\frac{u_3'}{\overline{u_3}} + \frac{A_{13}}{A_{33}}\frac{u_1'}{\overline{u_3}} + \frac{A_{23}}{A_{33}}\frac{u_2'}{\overline{u_3}}\right] \quad (5.31)$$

Raising eq.5.31 to the square and extracting its time average, it is possible to obtain a relationship that links the fluctuation of the cooling

velocity to the six components of the Reynolds stress tensor. The term $\overline{q'^2}$ is nothing but the square of the cooling velocity root-mean-square (RMS) value. Hence, the solving equation is the following:

$$\overline{q'^2} = \frac{A_{13}^2}{A_{33}}\overline{u_1'^2} + \frac{A_{23}^2}{A_{33}}\overline{u_2'^2} + A_{33}\overline{u_3'^2} + \frac{A_{13}A_{23}}{A_{33}}\overline{u_1'u_2'} + 2A_{13}\overline{u_1'u_3'} + 2A_{23}\overline{u_2'u_3'} \quad (5.32)$$

Finally, eq.5.32 can be rewritten defining new coefficients C_{ij} in order to simplify the notation in the following way:

$$\overline{q'^2} = C_{11}\overline{u_1'^2} + C_{22}\overline{u_2'^2} + C_{33}\overline{u_3'^2} + C_{12}\overline{u_1'u_2'} + C_{13}\overline{u_1'u_3'} + C_{23}\overline{u_2'u_3'} \quad (5.33)$$

Where the coefficients C_{ij} introduced in eq.5.33, depend only on h, k^2, on the rotation φ_{rot} and on the slant α angle. Hence, eq.5.33 represents a system of N linear equations, one for each rotational position addressed by φ_{rot}, whose unknowns are the components of the Reynolds stress tensor.

The procedure described up to now, assumes that the constant term of the Jørgensen equation rewritten in the form of eq.5.33 can be derived from the anemometer measurements. This term represents the square of the RMS of the wire cooling velocity, and it is evaluated for every sub-interval over 40. For the VAWT data elaboration, this was computed rigorously, as:

$$\overline{q'^2} = Q_{RMS}^2(j, \overline{X}) = \frac{\sum_{i=1}^{N_{BPP}} \left(Q(i, j, \overline{X}) - Q_{PER}(j, \overline{X})\right)^2}{N_{BPP}} \quad (5.34)$$

Where the terms of eq.5.34 represent:

- $Q(i, j, \overline{X})$: Instantaneous cooling velocity of the measuring point $(\overline{X})$, function of the number of sub-intervals N_{PER} over a BPP and of the whole number of blade passing periods (N_{BPP}) over the whole testing time.

- $Q_{PER}(j, \overline{X})$: This term represents the periodic component of cooling velocity, since it is a time-dependent quantity that varies within the blade passing period, but does not change from one BPP to the other, because it is an averaged value. It is a cooling velocity of a BPP that is representative of the whole testing session.

For the VAWT, this Q_{RMS} value can be then computed and it can be used to solve eq.5.33. For the GT application, instead, the situation is quite different. Since periodic unsteadiness downstream of a statoric

cascade is nearly zero, as discussed in the previous paragraphs, it is possible to simplify the problem, and consider the periodic ensemble average equivalent to a simple time average. This way, the Q_{RMS} calculation can be further simplified. The Reynolds decomposition can be applied to the output voltage and to the cooling velocity.

$$E = \overline{e} + e'$$
$$Q = \overline{q} + q'$$

Recalling the King's law, it is possible to rewrite it according to the Reynolds decomposition of the output voltage alone.

$$E^2 = E_0^2 + BQ_n^2$$
$$Q = \left(\frac{\overline{e}^2 - E_0^2}{B}\right)^{\frac{1}{n}} \left(1 + \frac{e'^2 + 2\overline{e}e'}{\overline{e}^2 - E_0^2}\right)^{\frac{1}{n}} \tag{5.35}$$

Rewriting eq.5.35 in a binomial expansion series, stopping at the third order term, it is possible to obtain the following:

$$Q = \left(\frac{\overline{e}^2 - E_0^2}{B}\right)^{\frac{1}{n}} \left[1 + \frac{1}{n}\frac{e'^2 + 2\overline{e}e'}{\overline{e}^2 - E_0^2} + \frac{1}{2n}\left(\frac{1-n}{n}\right)\left(\frac{e'^2 + 2\overline{e}e'}{\overline{e}^2 - E_0^2}\right)^2\right] \tag{5.36}$$

It is possible to obtain an expression for the time-mean cooling velocity by averaging eq.5.36 and neglecting the terms $\overline{e'^3}$ and of higher order. The time-mean term $\overline{q}$ is then written as a function of the time-mean tension $\overline{e}$ and of the squared average voltage $\overline{e}^2$.

$$\overline{q} = \left(\frac{\overline{e}^2 - E_0^2}{B}\right)^{\frac{1}{n}} \left[1 + \frac{1}{n}\frac{\overline{e'^2}}{\overline{e}^2 - E_0^2} + \frac{2}{n}\left(\frac{1-n}{n}\right)\frac{\overline{e}^2\overline{e'^2}}{(\overline{e}^2 - E_0^2)^2}\right] \tag{5.37}$$

Moreover, it is also possible to substitute the Reynolds decomposition of both output voltage and cooling velocity inside the King's law, expand in a binormal series the term

$$B\overline{q}^n\left(1 + \frac{q'}{q}\right)^{\frac{1}{n}}$$

and neglect the terms

$$\left(\frac{q'}{q}\right)^2$$

and of higher orders. The result is the following equation:

$$\overline{e}^2 + e'^2 + 2\overline{e}e' = E_0^2 + B\overline{q}^n \left[1 + n\left(\frac{q'}{\overline{q}}\right)\right] \tag{5.38}$$

On a time average, eq.5.38 becomes:

$$\overline{e}^2 + \overline{e'^2} = E_0^2 + B\overline{q}^n \tag{5.39}$$

Subtracting eq.5.39 to 5.38, neglecting the terms $e'^2 - \overline{e'^2}$, raising to the square the resulting expression and averaging it on a time basis, another relation is obtained, linking the terms $\overline{q'^2}$ and $\overline{e'^2}$. This relation is the following:

$$\overline{q'^2} = \left[\frac{2\overline{e}}{nB(\overline{q})^{n-1}}\right]^2 \overline{e'^2} \tag{5.40}$$

This second procedure was applied to the axial-flow stage, considering the "average" as the time mean measurement, simplifying thus the problem, but introducing the approximation of not considering any periodic unsteadiness [11].

The system of equations expressed by eq.5.33 allows to determine the six velocity components of the Reynolds stress tensor. To solve it, at least six equations are necessary, one for each of the components of the Reynolds stress tensor, which is a 3×3 symmetric matrix in its general form. Hence, at least six rotations of the probe around its axis, identified as φ_{rot} are required to solve the problem. Anyway, this is the most complete case that could arise, in which all the three velocity components are made available. For both cases presented in this work, instead, the longitudinal/radial velocity measurements along x_1 have not been considered. Hence, for the specific purpose of this data elaboration, the Reynolds stress tensor is just a 2×2 matrix, and the unknown terms of eq.5.33 are just two diagonal terms $u_{22} = \overline{u_2'^2}$, $u_{33} = \overline{u_3'^2}$ and one extra-diagonal term $u_{23} = \overline{u_2' u_3'}$. This choice is suggested by the high uncertainty of the normal probe regarding U_1 measurements, and its result is coefficients C_{11}, C_{12} and C_{13} going to zero. The procedure for the Reynolds stress calculation used in the present work is then the following:

1. Signal Acquisition. The probe was mounted on its support for data acquisition, and different testing sessions are carried out with a different number of rotations. For the GT tests, some acquisitions were carried out with 3 rotations, leading to an iso-constrained problem resolution, while other records were performed with 9 rotations, in

order to test the accuracy of the over-constrained problem in comparison with the iso-constrained one. The VAWT campaign, instead, has only three probe rotations available.

2. Fluctuating cooling velocity calculation. For each rotational position, the average of the fluctuating cooling velocity to the squared was computed either by means of eq.5.34 for the VAWT, or through eq.5.40 for the GT. This allows to have a proper input value for eq.5.33.

3. Coefficients Calculation. The Jørgensen coefficients C_{ij} for the velocity fluctuations are computed starting from the coefficients for the Jørgensen equation A_{ij} taken from the yaw angle algorithm.

4. System Resolution. A system of N equations in three unknowns is resolved in two ways: as an iso-constrained system of equations and as an over-constrained one. The iso-determined system of three equations in three unknowns was resolved in matrix notation, while the over-determined system was resolved using a least-squared algorithm suitable for systems of linear equations. [9]

The sampling frequency of the HW anemometer, which is of 500 kHz, is actually reduced when elaborating the signals, due to the N_{PER} averaging, in which each of the 40 sub-intervals in which the blade passing periods are discretized is actually a time average of many more signals. The result is a sampling frequency that is reduced to $400 \div 800$ Hz in the VAWT application. This means that with such elaboration procedure, fluctuations characterized by a maximum frequency of $200 \div 400$ Hz can be properly captured, according to the Nyquist-Shannon theorem.

All the procedure was carried out in Fortran 90. A dedicated routine was written to be then implemented in the LFM software. This is rapidly launched by running the executable file since it is able to read directly the binaries given as outputs by the LabView® software. The routine gives itself an output, which is a text file in which the Reynolds stress tensor 2×2 components derived through the aforementioned procedure are printed: $u_{22} = \overline{u_2'^2}$, $u_{33} = \overline{u_3'^2}$ and $u_{23} = \overline{u_2' u_3'}$.

5.8 The Algorithm for the turbulent integral length scale

The final part of the data elaboration is represented by the calculation of the turbulent integral length scale, which has been evaluated for the

VAWT alone. This computation is fairly simple, once the theoretical basis reported in chapter 1 are clear. The first step is the extraction of the velocity fluctuation described in eq.5.23. This will be a zero-average signal that varies in time all over the acquisition period, made by few revolutions of the turbine around its axis. Starting from this signal, the Eulerian autocorrelation coefficient is computed for every point of the measuring grid in a discretized form:

$$r_E(i, \overline{X}) = \frac{1}{N} \frac{\sum_{j=1}^{N} u'(j, \overline{X}) u'(j+i, \overline{X})}{e_k(\overline{X})} \tag{5.41}$$

In this case, i represents the time lag (τ) from a generic instant of time j. The constant N, instead, is the number of time intervals over which the correlation of velocity fluctuations with themselves is investigated. This means that for how the formula for $r_E(i)$ is made, of the whole number of time intervals available, only a half of them can be really used to evaluate the autocorrelation. In any case, the results show that this is not an issue, because the velocity fluctuations cease to be correlated with themselves much earlier. Hence, if 800 time steps are available, N will be equal to a half of it ($N = 400$). The term e_k, finally, indicates the average turbulent kinetic energy, calculated as:

$$e_k(\overline{X}) = \frac{1}{2N-1} \sum_{j=1}^{2N} \left(u'(j, \overline{X}) - \overline{u'(\overline{X})} \right)^2 \tag{5.42}$$

And again the average fluctuation is for sure:

$$\overline{u'(\overline{X})} = \frac{1}{2N-1} \sum_{j=1}^{2N} u'(j, \overline{X}) \tag{5.43}$$

Thanks to these three simple equations, it is possible to compute the Eulerian autocorrelation coefficient, and hence the turbulent integral time scale by definition.

$$T_E(\overline{X}) = \int_0^{\infty} r_E(\tau, \overline{X}) d\tau \tag{5.44}$$

This expression can be then reported in a discretized form, by computing the Riemann sum of the autocorrelation coefficient. Please notice that such expression is valid only if any periodic component has been preliminarily eliminated, and hence if the autocorrelation coefficient goes rapidly

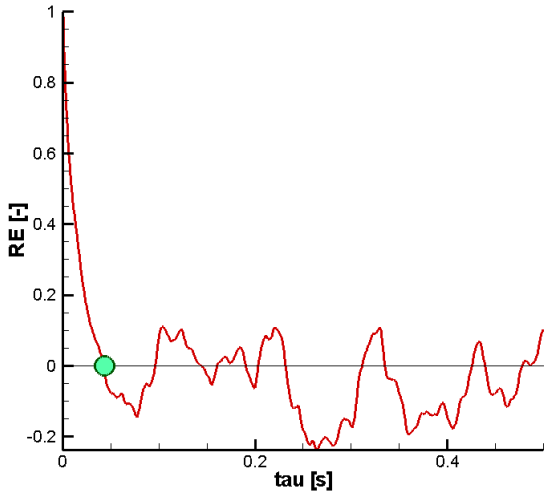

Figure 5.3: The autocorrelation coefficient computed for a sample point in the VAWT wake.

and monotonically to zero. This is of course not true in the VAWT case, where the wake is inherently unsteady and periodic. Hence, eq.5.44 will be considered valid only up to the point in which R_E reaches zero and it will not be considered afterwards where more or less periodic fluctuations arise in real flows. An example of the autocorrelation coefficient is represented in Fig.5.3, and the integral for T_E will be hence computed not up to infinity, but up to the time value corresponding to the green dot.

The integral length scale is then computed in its discrete form as:

$$T_E(\overline{X}) = \frac{1}{N} \sum_{i=1}^{N_{sig}-1} \left(\frac{r_E(i, \overline{X}) + r_E(i+1, \overline{X})}{2} \right) \tag{5.45}$$

Where N_{sig} is the number of significant intervals of time for the calculation of T_E, that means up to the point at which $R_E(\tau, \overline{X})$ goes to zero, called *correlation time*. Finally, to pass from the integral time scale to the integral length scale, to have an idea of the largest vortex dimensions in the wake, the Taylor's hypothesis shall be applied.

$$X_E[m](\overline{X}) = T_E[s](\overline{X}) \times V_{TM}(\overline{X}) \tag{5.46}$$

Chapter 6

Results and Discussion

In this chapter, the results of the data elaboration will be presented in detail, first for the VAWT and then for the GT. The starting point of this discussion will be the measurements regarding the phase-average flow quantities, while the unsteady properties will be presented afterwards. Then, a further insight in the unsteadiness of the phenomena will be given by means of the study on turbulence, in the specific case the results for turbulence intensity, the Reynolds stress tensor and the turbulent integral length scale for the whole measuring plane will be commented.

6.1 Operating Conditions

6.1.1 VAWT

The VAWT has been tested in several operating conditions, identified by the tip-speed ratio λ, which is the main similarity parameter that characterizes the performance of a wind turbine. This parameter is defined as the ratio of the peripheral speed of the machine and the incoming wind velocity:

$$\lambda = \frac{\omega R}{v_0} \tag{6.1}$$

It is always a good idea to test the machine in operating conditions close to its optimum, but it is also interesting to investigate its behavior at the other side of the efficiency curve, for $\lambda < \lambda_{opt}$. The optimum, for a wind turbine, is typically identified with the point of maximum power coefficient (c_p). For the specific case, the tested conditions for the H-Darrieus turbine are listed below. These were chosen on the basis of the $c_p - \lambda$ curve of the machine, presented in Fig.6.1 in comparison with a

troposkien rotor. The maximum c_p condition is interesting since it is the one in which the machine is operating most of the time, due to its design. The low loading condition ($\lambda < \lambda_{opt}$), instead, is interesting since it is the one in which the machine has to work at every start-up and regulation.

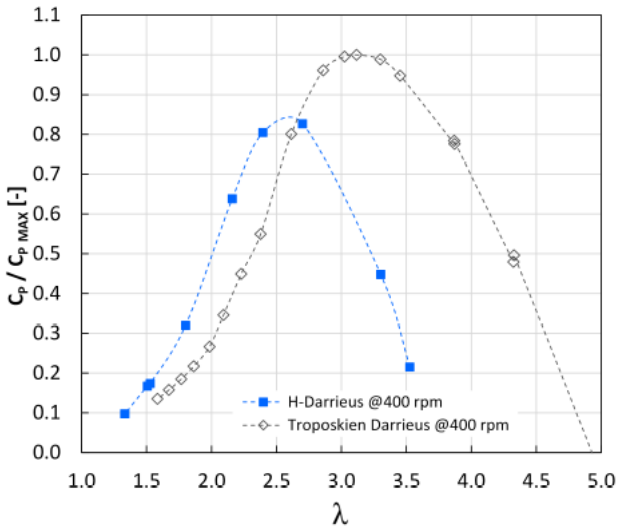

Figure 6.1: Performance curve of H-Shaped vs. Troposkien turbines as a function of λ.

The operating conditions in which the machine has been tested are the one listed below, that can be summarized in two points belonging to the $c_p - \lambda$ curve, one at optimum λ, and one for $\lambda < \lambda_{opt}$.

H-Darrieus:

$$v_0 = 9.0\ m/s;\ \omega = 400\ rpm \rightarrow \lambda = 2.4$$
$$v_0 = 14.2\ m/s;\ \omega = 400\ rpm \rightarrow \lambda = 1.5$$

$$v_0 = 10.7\ m/s;\ \omega = 300\ rpm \rightarrow \lambda = 1.5$$
$$v_0 = 7.1\ m/s;\ \omega = 200\ rpm \rightarrow \lambda = 1.5$$

6.1.2 GT

The operating points of the axial turbine stage are just two, and they are only a part of all the working conditions investigated with the FRAP

probe, which are the same operating points as the RECORD campaign. Due to its delicate structure, in fact, the hot wire anemometer should not be used at Mach numbers greater than around 0.4, otherwise it will possibly break. The operating conditions of interest for the GT are then the following:

Axial-Flow Stage OP4:	Axial-Flow Stage OP5:
$\omega_T = 5510\ rpm$	$\omega_T = 4008\ rpm$
$\omega_C = 9710\ rpm$	$\omega_C = 7120\ rpm$
$\beta_T = 1.206$	$\beta_T = 1.103$
$T_{Tup} = 35°C$	$T_{Tup} = 35°C$

6.2 Numerical Methods Validation

As it was discussed in section 6.2, two different procedures are available to solve a system of non-linear equations, depending on whether the system is iso or over-determined. For the iso-constrained system, the Newton-Raphson (NR) method was chosen, while for the over-constrained one, a least-square approach was preferred, implemented by means of the Levenberg-Marquardt Algorithm (LMA). Both methods were applied to the same set of data, in order to test their accuracy, just for the algorithm of the normal probe (sec.5.4), for sake of simplicity. In Fig.6.2, for instance, the comparison between the three possible iso-determined systems of equations is presented. For this purpose, the velocity magnitude and yaw angle algorithm was launched in its iso-constrained form and solved with the NR method. Three solutions have been derived, one for each combination of the probe rotations φ_{rot}, and they have been compared one to each other. Three are as well the combinations of the three solutions in groups of two, and each combination is treated as a different series of data. The three series, thus, contain the relative velocity difference between the combined solutions, and the purpose of the box-plot is to show where the most frequent values are distributed. The comparison of the three combinations is facilitated putting them one next to the other. Each box-plot for each series of data is made of two adjacent boxes containing each 25% of the data, while the whiskers enclose a range up to $\pm 2.7\sigma$, where σ is the dataset standard deviation. What stands out is that the measurements with the $\varphi_{rot} = -45°$ rotation are more or less the same as those corresponding to the opposite rotation $\varphi_{rot} = +45°$, with

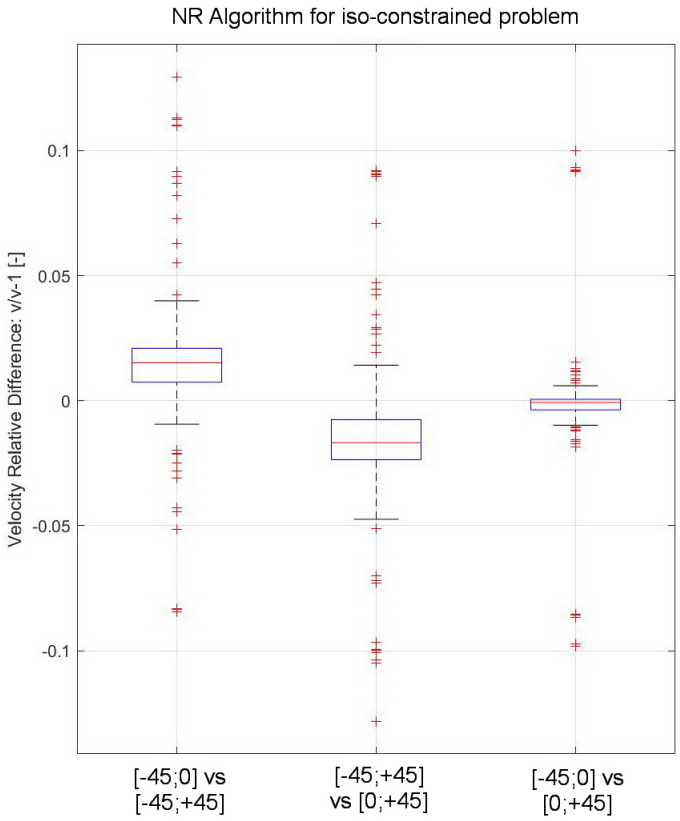

Figure 6.2: Comparison between the three possible solutions of the iso-constrained system for velocity magnitude.

the opposite sign. As a matter of fact, the first and the second series of the box-plot differ more or less of a minus sign, and the third series of the plot looks symmetric around the zero, with a very thin box and short whiskers. This trend demonstrates the consistency of the flow measurements acquired for the three rotations around the probe axis. In any case, the three solutions differ one from another of the order of 3% more or less, with peaks of 10%, which is not little for the accuracy required in this set of measurements.

The next step for the validation of the numerical methods is the comparison between the two algorithms, the NR and the LMA, which means a comparison between an iso-constrained solution and an over-constrained one. Hence, the *lsqnonlin* Matlab function was implemented as well in the same dataset, and it was compared to the three NR solutions, this time both in terms of velocity magnitude and yaw angle. The result is

reported in Fig.6.3. For this case, it is possible to notice that the velocity magnitude does not show any particular trend varying the NR system to whom the LMA is compared. The two methods differ of a quantity that is lower than 3% for most of the cases, with some outliers reaching peaks of 10% difference. The symmetry of the measurements derived by a symmetric probe rotation, is instead visible in the yaw angle results. As a matter of fact, in this case, it is clear that the system solved using $\varphi_{rot} = [-45°;\ +45°]$ resembles the LMA solution, while the other two are symmetric one with respect to the other.

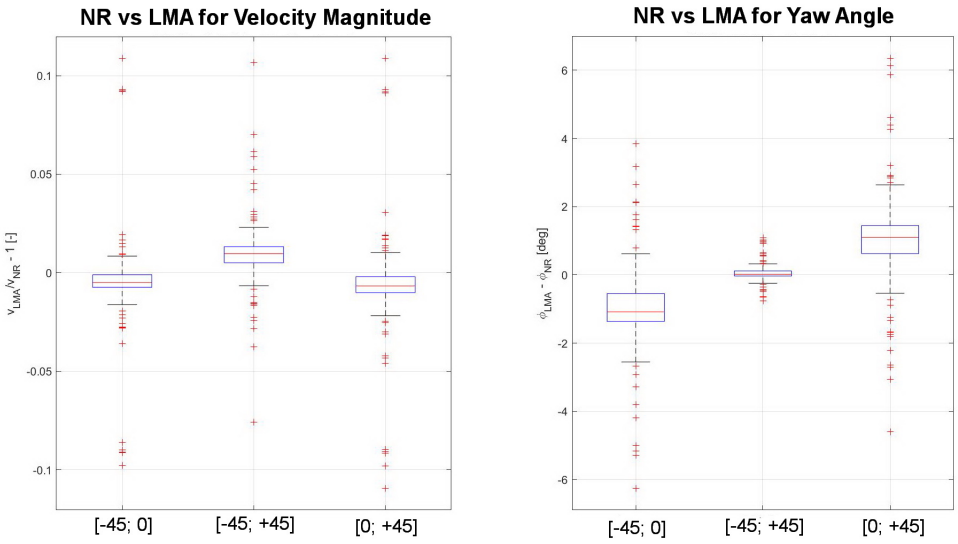

Figure 6.3: Comparison between LMA and the three NR solutions.

In conclusion, the comparative charts shown in the present section proof the consistency of the two numerical methods. Nevertheless, since the present work deals with experimental measurements, it is preferable is to implement an over-constrained system of equations, and solve it by means of a least-squared approach (LMA), as reported in previous works [12]. This is the reason why from here on, the NR method is abandoned, and all the probe rotations will be used to solve the problem.

6.3 The VAWT H-Shaped Turbine

The results for the VAWT H-Shaped machine are discussed first. Here, two measuring planes were adopted, a near-wake plane in the y-z direction, transversal to the turbine wake, that will be addressed as 2D plane, and

a plane in the x-y direction that will be called from here on the blade-to-blade plane (B2B). The discussion of the results will be carried out comparing first the same measuring planes for the same machines in the two different λ conditions, and then the departures from similarity, meaning the same λ condition but different Reynolds numbers. Before starting, some further considerations will be made on the midspan traverse.

6.3.1 The Midspan Traverse

The very first approach to the VAWT measurements was performed on the midspan traverse. As a matter of fact, 1D measurements are much easier to handle from a computational point of view than 2D ones. For this reason, these data were used to investigate the sensitivity of the problem to the number of rotations, to compare the results with another steady probe, and to test the robustness of the pitch angle algorithm. The results of the midspan traverse are not just the extract of the results of the 2D plane corresponding to $z = 0$, they have been recorded in a different acquisition session and at precise operating conditions.

6.3.1.1 The Midspan traverse for the numerical method investigation

The machine was rotating at 400 rpm, and the incoming wind velocity was 9 m/s and 12 m/s, corresponding respectively to a tip-speed-ratio λ of 2.4 (optimal) and 1.8 (low loading). For both operating conditions, two sets of data are available: one with three probe rotations, and another one with nine probe rotations.

$$\varphi_{rot}^{(3)} = [-45°;\ 0°;\ +45°]$$
$$\varphi_{rot}^{(9)} = [-55°;\ -45°;\ -35°;\ -10°;\ 0°;\ +10°;\ +35°;\ +45°;\ +55°]$$

These two datasets have been elaborated with the LMA approach, and the results are compared both for velocity magnitude and yaw angle. What comes out is reported in Fig.6.4 for dimensionless velocity, and in Fig.6.5 for yaw angle.

For velocity magnitude, the results are almost completely overlapping. The two different resolutions of the problem give the same velocity values, which are particularly consistent with previous investigations [6]. As the loading reduces and goes farther from the optimum, the energy extraction process becomes less effective, and the wake velocity gets higher, especially in the leeward portion of the machine ($y > 0$). Furthermore, as the

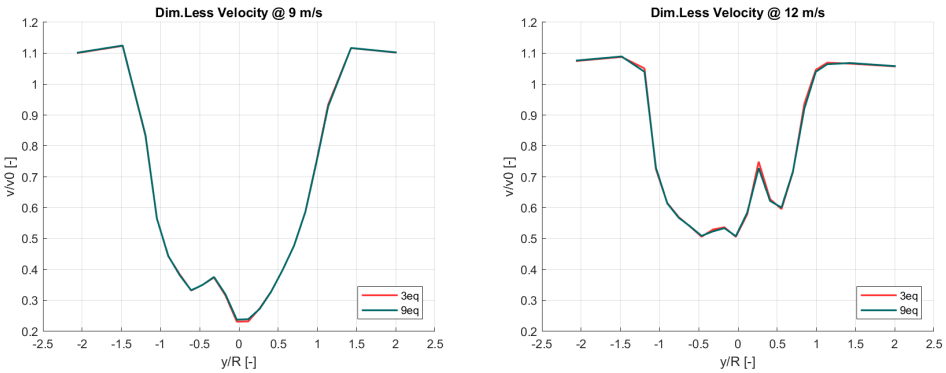

Figure 6.4: Dimensionless Velocity. A comparison between 3 and 9 equations.

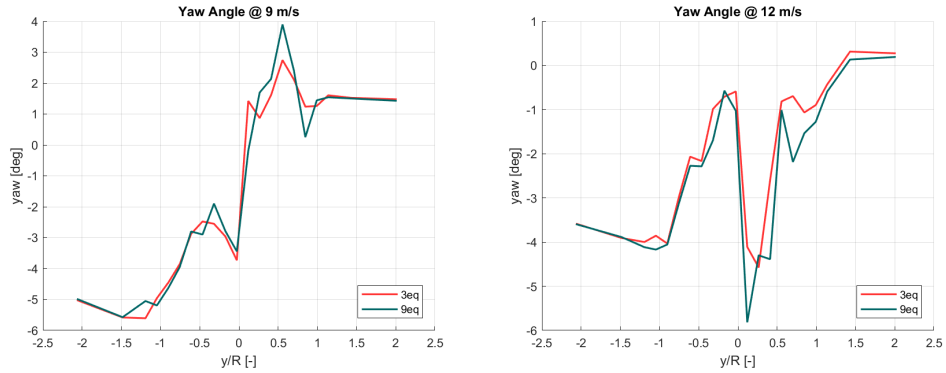

Figure 6.5: Yaw Angle. A comparison between 3 and 9 equations.

machine velocity becomes smaller with respect to the incoming wind ($\lambda \downarrow$), the freestream overspeed reduces much faster going far from the wake.

On the other hand, the yaw angle profiles are not perfectly matching between three and nine equations resolution. In spite of this, two important features can be put in evidence on these outcomes, showing the consistency of the two methods. The first is that the trends of the two cases are the same, even if the results show some differences, and display the same phenomena with the same magnitude. The other is that both systems of equations correctly capture the freestream condition in the leeward ($y > 0$) region, which is that of an undisturbed wind, with almost null yaw angle ($\varphi \approx 0°$).

A quantitative comparison can be finally drawn, reported in the boxplot of Fig.6.6, where a relative difference is presented for velocity values, while an absolute difference is reported for yaw angles. From such graph it is possible to remark what previously stated on a qualitative basis, the

two resolutions are almost equivalent, and the difference between them is not related to the operating condition being tested.

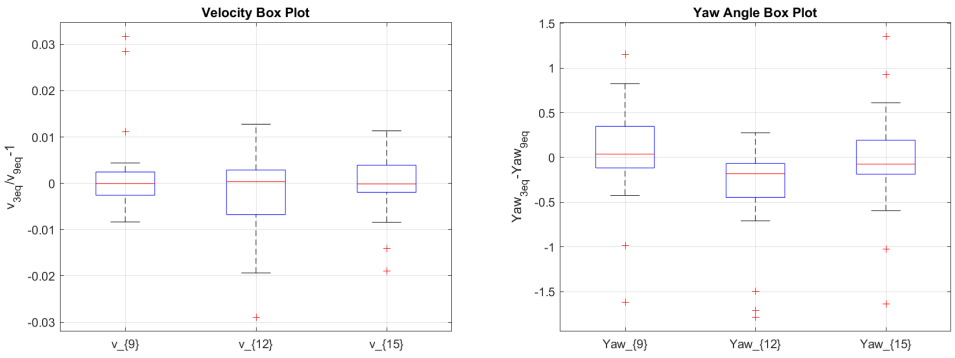

Figure 6.6: Quantitative comparison between three and nine equations resolution.

In conclusion, depending on what kind of datasets are made available and evaluating the accuracy-computational and testing cost trade-off for every case, three rotations or nine rotations can be used to solve the problem, knowing that both methods will give reliable results.

6.3.1.2 The Midspan traverse for the five-hole probe comparison

The measurements carried out at the midspan traverse have also another function, they can be used to remark the importance of hot wire anemometry for the VAWT wake measurements against the five-hole probe. The hot wire becomes particularly useful for the measurement campaigns analyzed in this work, for two reasons:

- The HW is an unsteady probe, and hence it allows to measure unsteady flow properties. The five-hole probe, instead, is a slow response device, and cannot be used for this purpose.

- The HW is particularly accurate even in those regions at very low velocity, in which the five-hole probe loses sensitivity, for instance in the core of the wake of the λ_{opt} condition. The problem of the steady probe is that for very low velocities, the pressure difference between the five different holes is below the probe sensitivity, and no pressure gradient is revealed.

The second issue has been investigated through the midspan traverse measurement, and it is reported in the following pictures. In Fig.6.7, in the specific case, this phenomenon is particularly clear. In the wake region of the optimum λ condition, where the velocities are too small, the five-hole probe gives unrealistic results, while in the velocity profile is well captured in the freestream region and in the low loading case. The same discussions can be repeated for the yaw angle measurements, as reported in Fig.6.8.

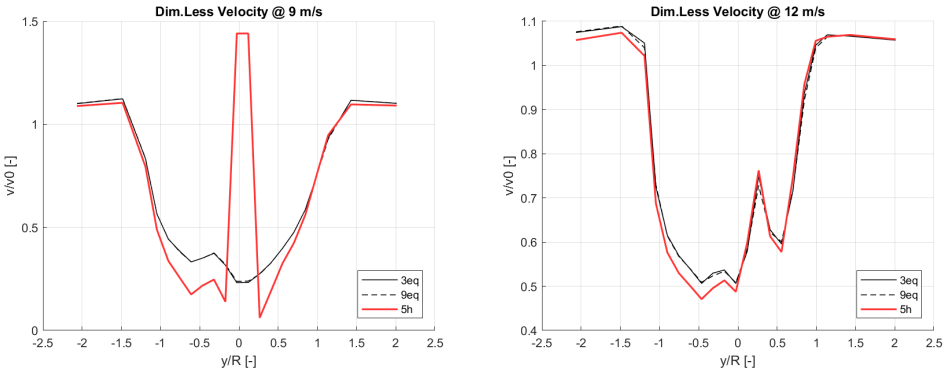

Figure 6.7: HW anemometer compared to 5-hole probe for velocity measurements.

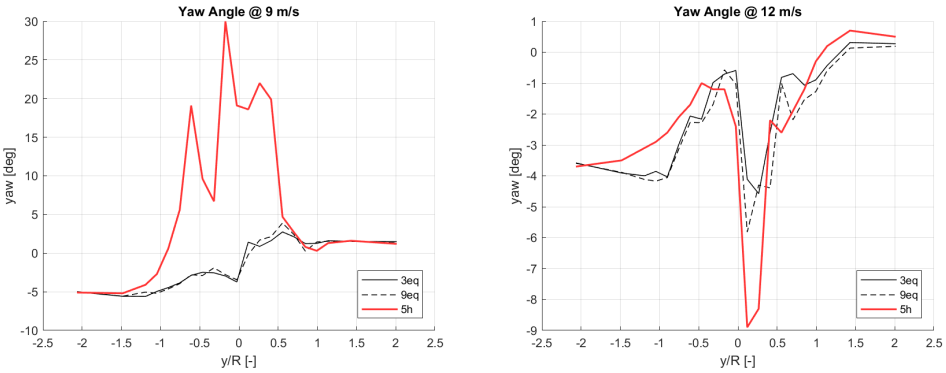

Figure 6.8: HW anemometer compared to 5-hole probe for yaw angle measurements.

6.3.1.3 The Midspan traverse for the pitch angle calculation

Pitch angle shall be computed by means of the algorithm introduced in section 5.5, and it requires the measurement of a slanted hot wire to be

implemented. As discussed in the previous chapters, a precise calibration was necessary to pursue the accuracy of the results.

Also in the previous work on the 2016 VAWT experimental campaign [7], the slanted wire measurements were implemented to calculate the pitch angle, but with poor results. In the present work an improvement was brought about to the original algorithm, and the robustness of the enhanced procedure was tested on the midspan traverse only. Both operating conditions available for the midspan traverse were analyzed for this purpose, and all the nine rotations were used in different combinations to investigate the numerical differences. The yaw angle algorithm was run together with the pitch angle one for the following probe rotations:

$$\varphi_{rot}^{(9)} = [-55°;\ -45°;\ -35°;\ -10°;\ 0°;\ +10°;\ +35°;\ +45°;\ +55°]$$

Organized in the following combinations:

Comb. $1 = [+55°;\ +45°;\ +35°;\ +10°]$	All Positive
Comb. $2 = [-10°;\ -35°;\ -45°;\ -55°]$	All Negative
Comb. $3 = [+55°;\ +35°;\ -10°;\ -45°]$	4 Rot. Alternated
Comb. $4 = [+45°;\ +10°;\ -35°;\ -55°]$	4 Rot. Alternated Inverted
Comb. $5 = [+45°;\ -10°;\ -55°]$	3 Rot. Alternated
Comb. $6 = [+55°;\ 10°;\ -45°]$	3 Rot. Alternated Inverted
Comb. $7 = \varphi_{rot}^{(9)}$	9 Rot.

In Fig.6.9, the results of the elaborations are presented and compared to the five-hole probe. Even at first sight, it is possible to notice that these results are definitely not reliable.

The conclusion is that not even the enhanced pitch angle algorithm is able to improve the results, and no combination of the probe rotations seems to give better outcomes than the others. As a matter of fact, at midspan, for symmetry reasons, the pitch angle should be close to zero, and the five-hole probe captures well this feature in low loading condition, showing a pitch angle of few degrees. This occurs because, at low λ, the flow velocity increases thus increasing the accuracy of the five-hole probe. Results as the one given by the slanted wire $\vartheta < -10°$ in the wake are definitely not acceptable. From now on, only the yaw and velocity magnitude will be considered, while the longitudinal velocity U_1 is set to zero, and pitch as well, as a consequence. The results on velocity magnitude, instead, are matching with those for the sole yaw angle algorithm, but they

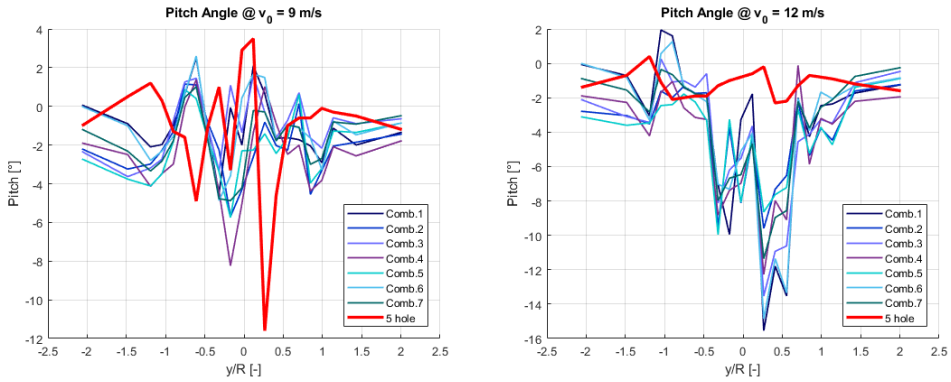

Figure 6.9: Pitch measured by the HW in the seven combinations vs. five-hole probe masurements.

are not reported here, since only the yaw procedure will be implemented in the rest of the work.

6.3.2 The 2D Plane

For symmetry reasons, the upper half and the lower half exhibit the same phenomena and hence, only one of the two parts is actually useful to investigate the wake. Moreover, using only one of the two portions, the testing time gets halved. Hence, in the campaign of 2016, only the lower half of the 2D near wake was sampled. To the purpose of this discussion, the machine and its wake can be split in two significant zones. A windward region, in some cases also addressed as upstream region ($y < 0$), and a leeward one ($y > 0$), also called downstream region sometimes. This frame of reference is described in Fig.6.10.

Both the phase-average and the unsteady results of the VAWT aerodynamics will be presented, putting in evidence the periodic structures that arise at every blade passage. In the maps reported from here on, the coordinates are made non-dimensional with respect to the geometry of the machine, in terms of rotor radius and height. Furthermore, to have clear the location of the machine in the maps, the rotor trace is superimposed to the graphs.

6.3.2.1 The 2D Plane comparison of phase-averaged quantities at different λ and fixed rotational speed ω

First, a comparison of the same H-Shaped machine at the same rotational speed ($\omega = 400\ rpm$) but in the two different operating conditions

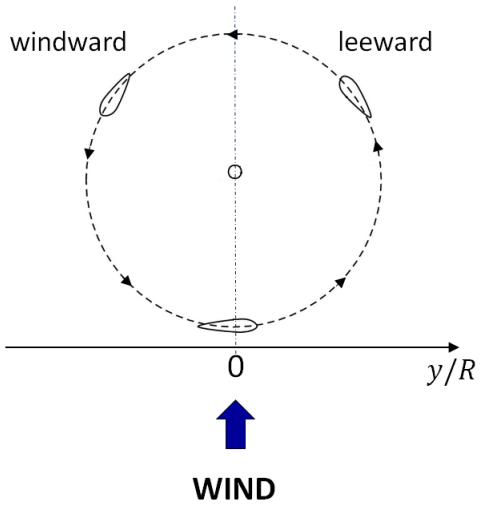

Figure 6.10: Machine frame of reference.

($\lambda = [1.5\ \ 2.4]$) is carried out. The results of the phase-average for the two operating points are reported in Fig.6.11, where the dimensionless velocity contour is plotted, together with the periodic and unresolved turbulence components.

Velocity magnitude, as it is for the rest of the maps from here on, is made non-dimensional with respect to the incoming wind speed, evaluated point by point on the basis of the static pressure, as discussed in Sec.5.2. This is important because it makes different operating conditions comparable one to another, but also as it allows to compare the single points of the measuring grid. As a matter of fact, the acquisition does not take place all at a time, but one point after the other, and upstream wind velocity fluctuations during the test are a common issue. Besides, the periodic turbulence and the unresolved one, presented in percentages, are computed as reported in Sec.5.6. Here too the same upstream velocity component is employed for a proper calculation.

From the maps presented in Fig.6.11, it is evident that the one at $\lambda = 2.4$ is the optimal loading condition, since the velocity defect that its wake experiences is much stronger than in the $\lambda = 1.5$ case. A deeper velocity reduction means indeed a better energy conversion. In the low loading case (6.17a), moreover, the low performance leeward region is put in evidence by a higher velocity zone on the right-hand side of the map, painted in yellow. Furthermore, the worse aerodynamic performance of the leeward region can be seen also from the turbulence maps, for the low loading case in particular, where it is clear that periodic structures of

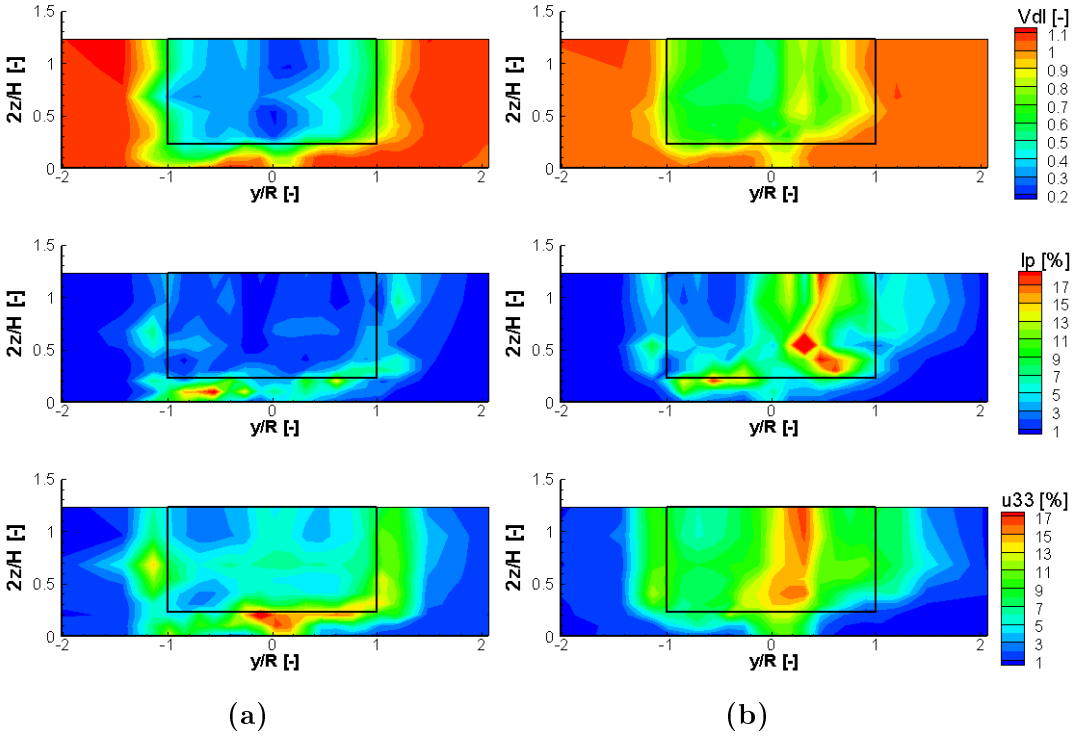

Figure 6.11: Comparison between the optimal loading case for $\lambda = 2.4$ (a), and the low loading case for $\lambda = 1.5$ (a). From the top: dimensionless velocity, periodic turbulence intensity and unresolved turbulence intensity.

higher strength are being shed, and non-resolved turbulence arises with a certain intensity and characterizes the whole wake. The leeward region has a poor aerodynamic performance also for the optimal loading condition (6.11a), of course, but the phenomenon is not so evident in the map, since it has a lower intensity. For this case, the turbulence maps do not present particular structures in the wake, at least not so clear as it is for the low loading condition, meaning that most of the vortical structures are already smeared out on the near-wake.

Moreover, the higher the loading, the stronger is the pressure gradient between pressure side and suction side of the VAWT blade, and hence the higher will be the tip vortex. It is interesting to note that this aspect, that has been observed also in previous works [5][1], arises from this campaign as well. It should be noticed that at both loading conditions, the velocity reduction is stronger in the windward region, where the performance of the machine is higher, and hence the force exchange is higher. Also periodic

unsteadiness increases in correspondence of the lower-left corner of the turbine trace, as to remark the formation of periodic structures in the windward tip region. On the leeward side, instead, they are still present, but with a lower intensity. Besides, the flow disturbances at the tip, both leeward and windward, are more important for $\lambda = 2.4$ (6.11a), than for $\lambda = 1.5$ (6.17a), to underline again the difference between the optimal and the low loading condition.

As expected again from a comparison with previous experimental investigations [6], it is important to notice that in both loading conditions velocity gradients arise at the wake margins. This means that in those regions, the fluid is organized in shear layers, giving rise hence to important turbulence zones. It is indeed here that turbulence intensity reaches its peaks. This phenomenon occurs more for the optimal loading case, where the higher velocity deficit necessarily brings to deeper gradients, and turbulence gets higher at the wake edges. In the not optimal low loading case, instead, velocity gradients are not so steep, and hence turbulence does not dominate the border of the wake, but it affects more the core and the leeward region of the flow, which is subject to vortical structures on its overall.

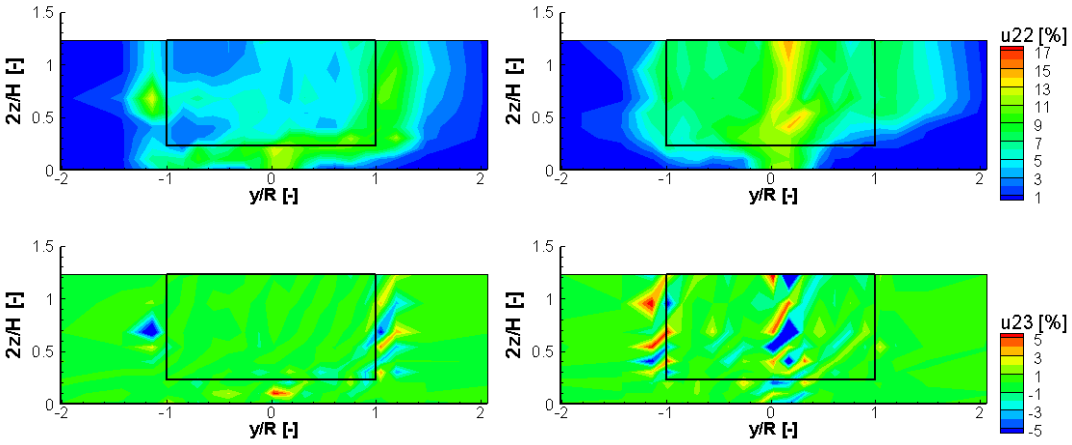

Figure 6.12: Comparison between the Reynolds stress tensor components in the optimal loading case for $\lambda = 2.4$ (a) vs. the low loading case for $\lambda = 1.5$ (b).

The conclusions drawn looking at the basic turbulence statistics are remarked by the results obtained with the evaluation of the Reynolds stress tensor components, reported in Fig.6.12. Here, the crosswise and

the cross-stream components are reported, as percentages over the upstream wind velocity. The streamwise component, instead, coincides with turbulence intensity, and it is already mapped in Fig.6.11. By comparing this with Fig.6.11, it is evident that where turbulence intensity is high, the crosswise velocity fluctuation is high as well. Besides, in the regions of wider vortical structures, the extra-diagonal term of the tensor is different from zero and alternates its signs frequently. This is exactly what is expected, an anisotropic turbulence field is the sign of a certain polarity of the turbulent fluctuations, and hence stronger counterrotating vortices. Moreover, the same conclusions can be drawn looking at the contour of the integral length scale of the turbulence spectrum, shown in Fig.6.14, where the larger eddies are again at the borders of the wake in the optimal loading case, and in the whole low velocity region for the low loading condition. The vortex shedding in the leeward region is essentially due to the dynamic stall occurring on the turbine blades. This phenomenon is illustrated in Fig.6.13, taken from the paper [5] in which the topic was investigated. Notice how the eddies detached in the leeward part of the turbine affect the wake instability.

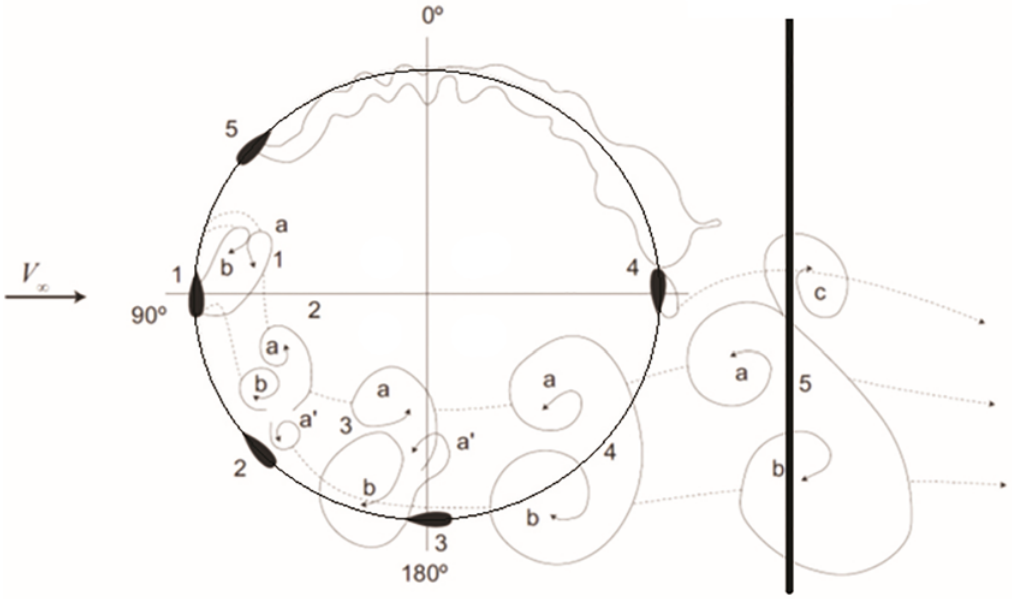

Figure 6.13: CFD simulation of dynamic stall.

Recalling what observed for the midspan traverse (Sec.6.3.1.1), it is possible to notice that in these measurements as well, there is a certain overspeed at the two sides of the wake, that dissolves going in the deep

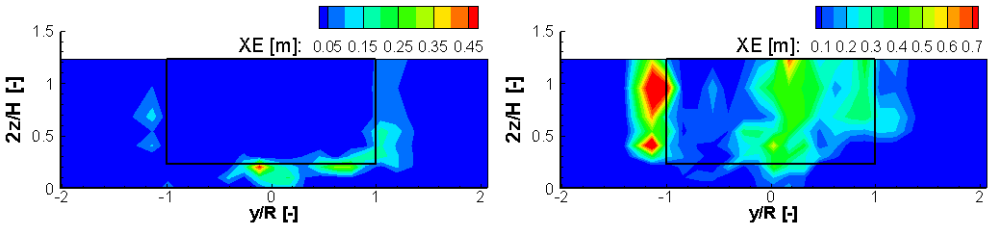

(a) (b)

Figure 6.14: Comparison between the integral lengthscales in the optimal loading case for $\lambda = 2.4$ (a) vs. the low loading case for $\lambda = 1.5$ (b).

freestream. This is an effect produced by the machine rotation, as its angular speed increases compared to the incoming wind, the trace of its blades can be approximated more and more as a continuous surface from the wind point of view. Hence, this behavior can be explained in analogy with that of a fluid impacting a cylindrical body, giving rise to an overspeed at the $y/R = \pm 1$ extremities of the domain.

Finally, a last interesting observation on the velocity field regards the presence of the struts. As a matter of fact, a measuring traverse close to $2z/R = 0.5$ was placed in order to capture the flow perturbation produced by the struts. The result is a bulge of the velocity profile corresponding exactly to that traverse, putting in evidence an important feature of a real machine wake. Notice that the turbulence maps as well show higher intensity zones corresponding to the struts position.

Another relevant property is the flow yaw angle. This has been derived thanks to the Fortran implementation of the dedicated algorithm explained in Sec.5.4, here shown in Fig.6.15 for the phase-averaged data.

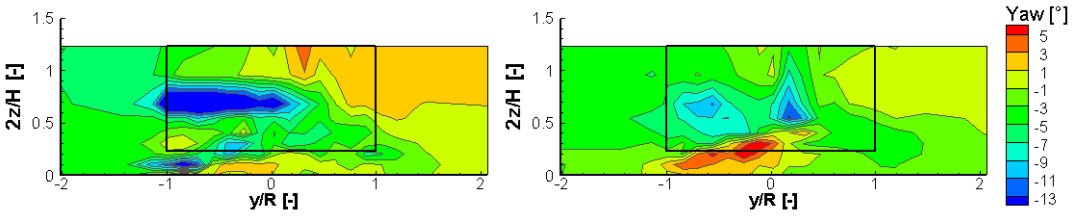

(a) (b)

Figure 6.15: Comparison of the yaw angle distribution between the optimal loading case for $\lambda = 2.4$ (a), and the low loading case for $\lambda = 1.5$ (a).

In this picture it is made clear what already commented for the turbulence contours. Large scale structures are forming at the tip region of the windward section of the machine. From this kind of picture, furthermore, it is made clear that the tip vortex is rotating in anticlockwise direction with respect to the observer. Moreover, the presence of the struts is particularly evident in the optimal loading case, where a big negative angle region arises in correspondence of the struts height. This can be explained thinking of the wake velocity distribution. As a matter of fact, the wake produced by the struts represents a strongly low momentum region, that is pushed to the left by the high momentum wake of the leeward side.

6.3.2.2 The 2D Plane comparison of phase-averaged quantities at fixed λ and variable rotational speed ω

The present section focuses on the departures from similarity produced by changes of the Reynolds number. In order to investigate such effect, the rotational speed was changed according with the incoming wind velocity in order to give the same tip-speed ratio. From this point of view, the velocity and turbulence fields are definitely the most interesting ones. In Fig.6.16, the situation at the optimal loading is first presented.

Looking carefully at the plot, it is evident that passing from 400 rpm to 300 rpm, the two contours are very similar one to another. Anyway, it is possible to note that the performance of the energy extraction process is decreasing as Reynolds number reduces.

When the original case is compared to a condition at even lower Reynolds number, instead, as reported in Fig.6.17, the changes in the core of the wake and in turbulence intensity are much more evident. As the rotational speed of the machine decreases, even at the same tip-speed ratio, the performance of the turbine reduces. This is a direct consequence of the aerodynamic performance reduction of the blade profiles, that depends on the Reynolds number. As a matter of fact, the as Re reduces, stall is anticipated on the profile, in terms of incidence angle. This means that the blade will stall during a higher portion of the revolution, shedding stronger periodic vortical structures, and giving rise to higher turbulence intensity in the whole wake.

6.3.2.3 The 2D Plane comparison of unsteady quantities at different λ and fixed rotational speed ω

A deeper understanding of the machine aerodynamics comes with the evaluation of the instantaneous flow properties, since the VAWT is charac-

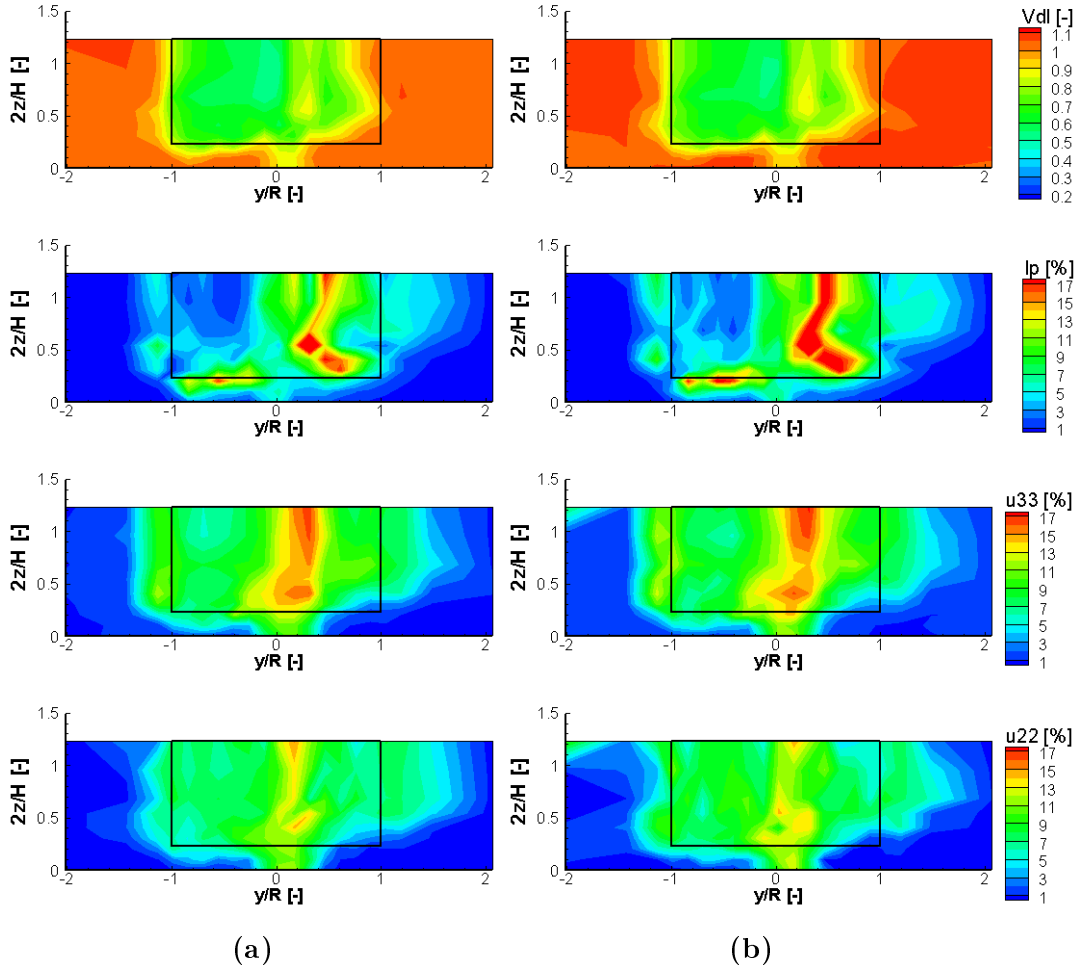

Figure 6.16: Comparison between the 400 *rmp* (a) and the 300 *rmp* (b) for $\lambda = 1.5$. From the top: dimensionless velocity, periodic turbulence intensity, unresolved turbulence intensity and crosswise Reynolds stress.

terized by a strong inherent unsteadiness. In the present section, the main flow quantities discussed above on a phase-average basis are reported in their instantaneous value for both loading conditions. The velocity magnitude, the yaw flow angle and the streamwise diagonal component of the Reynolds stress tensor will be described in the next lines, for four time instants only within a blade passing period (BPP). Recall from the previous chapters that one BPP has been discretized into 40 intervals, giving 120 time steps over the whole machine revolution.

The dimensionless velocity in the optimal loading condition is reported

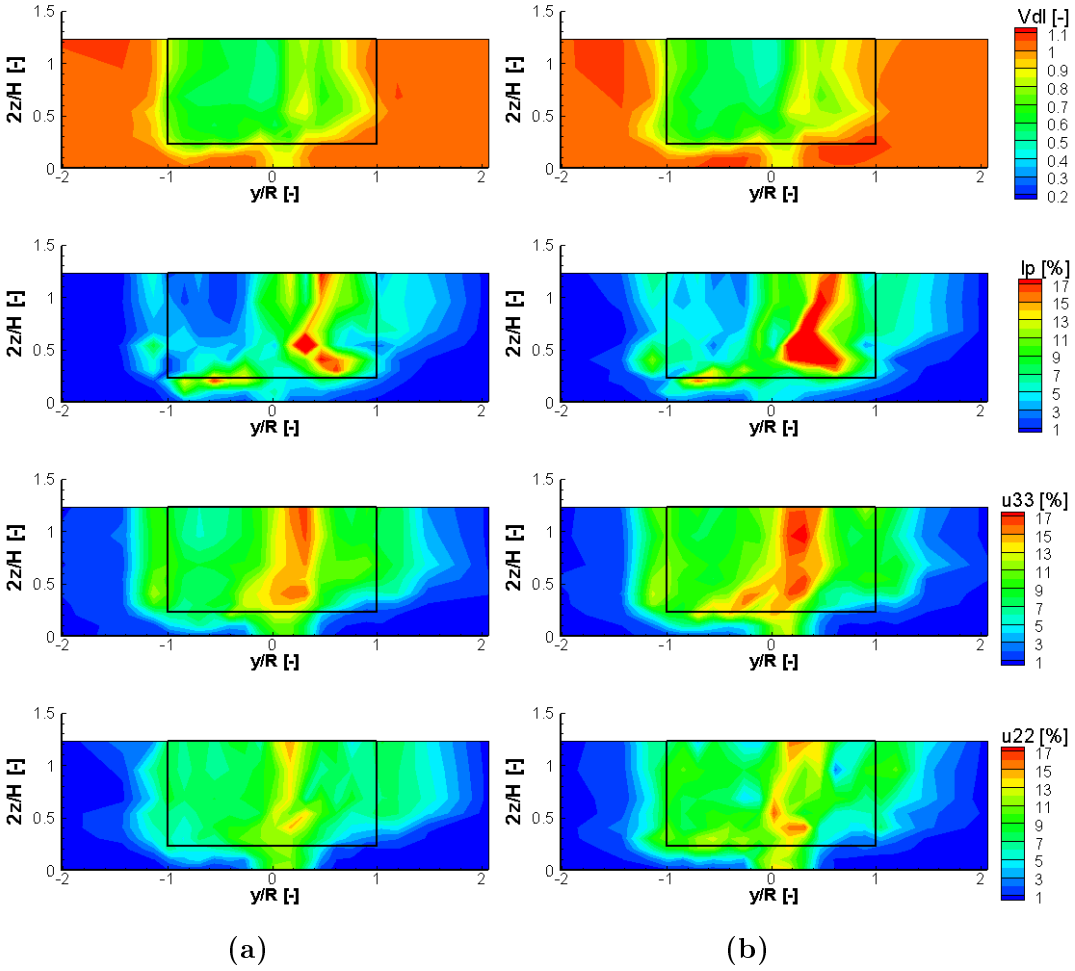

Figure 6.17: Comparison between the 400 *rmp* (a) and the 200 *rmp* (b) for $\lambda = 1.5$. From the top: dimensionless velocity, periodic turbulence intensity, unresolved turbulence intensity and crosswise Reynolds stress.

in Fig.6.18. Here it is evident that the machine wake is almost stable, and this is for sure due to the fact that the maximum performance condition has been chosen. The low loading condition represented in Fig.6.19, instead, has a very different time evolution. The wake is strongly asymmetric, and continuously changing in shape, due to the vortex shedding in the leeward region.

An even more interesting flow property to show, is the yaw angle evolution with time. Up to now, only the phase-average flow angle was calculated, but thanks to the Fortran translation of the Matlab algorithm, it is

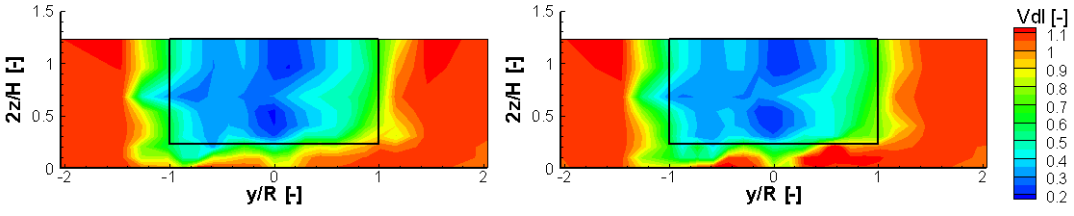

(a) Frame 01 **(b)** Frame 10

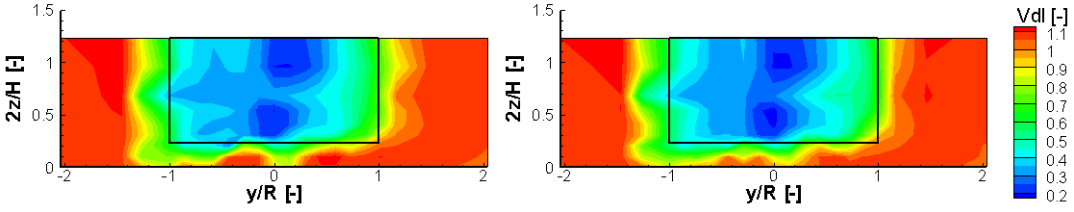

(c) Frame 20 **(d)** Frame 30

Figure 6.18: Instantaneous dimensionless velocity at $\lambda_{opt} = 2.4$ ($v_0 = 9\ m/s$; $\omega = 400\ rpm$), represented for four frames in sequence.

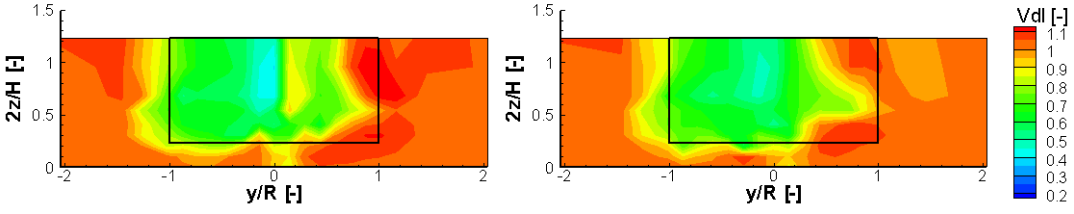

(a) Frame 01 **(b)** Frame 10

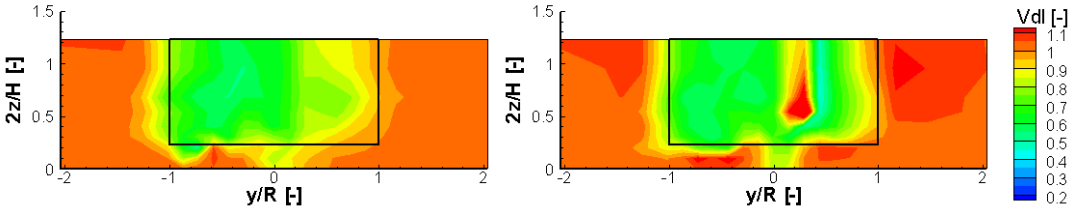

(c) Frame 20 **(d)** Frame 30

Figure 6.19: Instantaneous dimensionless velocity at $\lambda = 1.5$ ($v_0 = 14.2\ m/s$; $\omega = 400\ rpm$), represented for four frames in sequence.

possible to apply the routine also to the unsteady signals of the anemometer. The results of this data elaboration are presented in Fig.6.20 for the optimal loading case, and in Fig.6.21 for the low loading one. It is interesting to notice that for the yaw angle, opposite to what happens for the

velocity filed, even at maximum c_p condition, the flow is strongly unsteady.

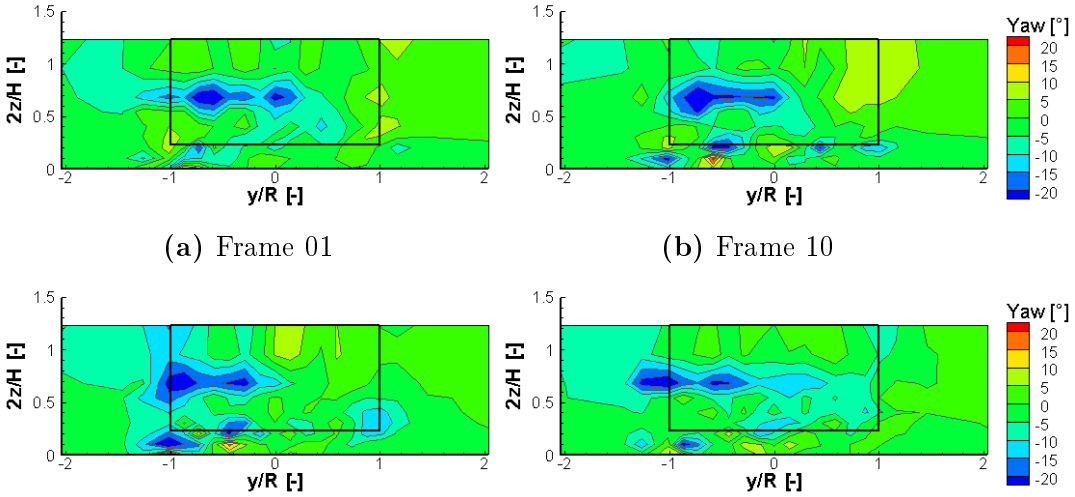

(a) Frame 01 (b) Frame 10

(c) Frame 20 (d) Frame 30

Figure 6.20: Instantaneous yaw angle at $\lambda_{opt} = 2.4$ ($v_0 = 9\ m/s$; $\omega = 400\ rpm$), represented for four frames in sequence.

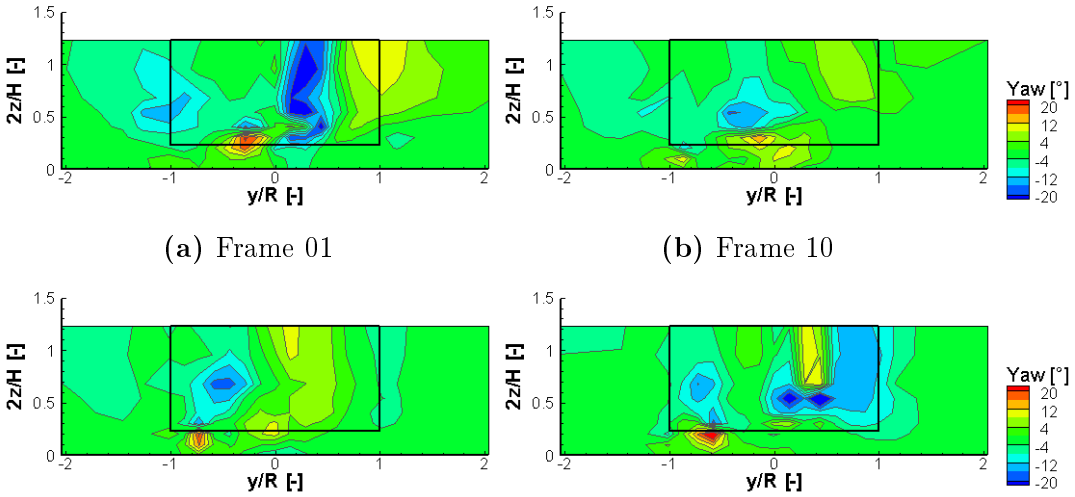

(a) Frame 01 (b) Frame 10

(c) Frame 20 (d) Frame 30

Figure 6.21: Instantaneous yaw angle at $\lambda = 1.5$ ($v_0 = 14.2\ m/s$; $\omega = 400\ rpm$), represented for four frames in sequence.

Moreover, thanks to the symmetric levels, the distinction between positive and negative angles is straight-forward. This way, it is possible to

see clearly the formation of the tip vortex and its advection to the outside of the wake. This is visible for both loading conditions, but the measurements for the low loading case are much clearer, without the strong disturbance of the struts. Concerning Fig.6.20, it is indeed interesting to notice that the flow deviation produced by the struts is particularly stable, since these alter the flow during the whole turbine revolution. On the other hand, the vortices shed at the tip are produced by a blade passage, and hence they have a typical pulsating character.

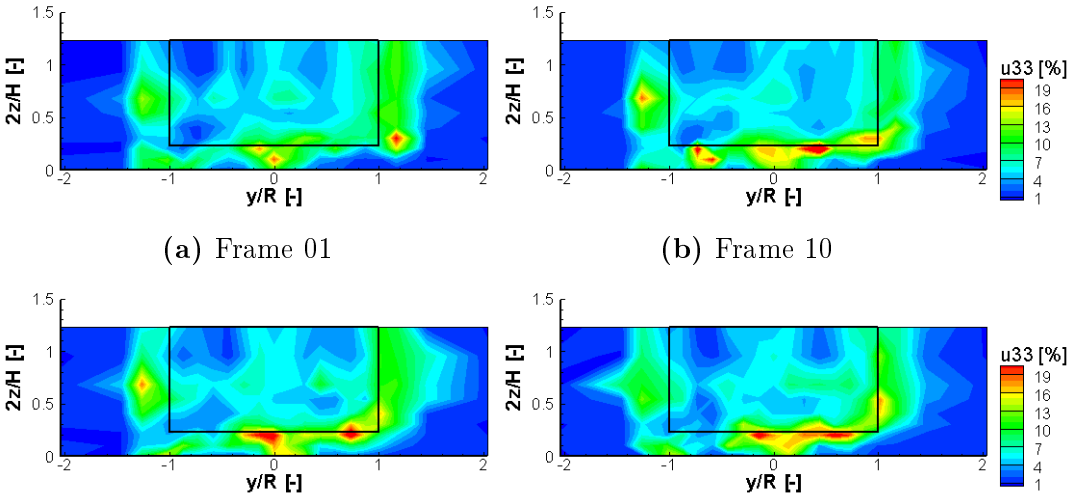

(a) Frame 01 **(b)** Frame 10

(c) Frame 20 **(d)** Frame 30

Figure 6.22: Instantaneous turbulence at $\lambda_{opt} = 2.4$ ($v_0 = 9\ m/s$; $\omega = 400\ rpm$), represented for four frames in sequence.

Finally, also periodic evolution of turbulence intensity is presented, evaluated as the streamwise component of the Reynolds stress tensor. The results are shown in Fig.6.22 for the optimal loading and in Fig.6.23 for the low loading case. As it was for velocity, the optimal efficiency case presents a much more steady wake than the low loading condition. In particular, as it was already clear from the phase-averaged results, turbulence interests the whole wake region for the worse efficiency case. Therefore, the aerodynamic is poor not only in the leeward zone, where dynamic stall is witnessed, but the whole wake suffers from severe flow detachment.

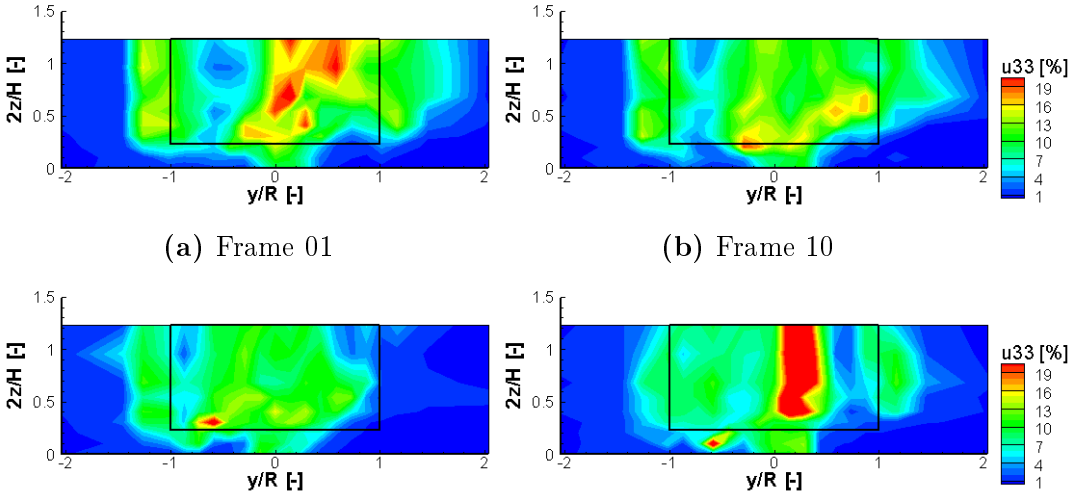

(a) Frame 01 (b) Frame 10

(c) Frame 20 (d) Frame 30

Figure 6.23: Instantaneous turbulence at $\lambda = 1.5$ ($v_0 = 14.2\ m/s$; $\omega = 400\ rpm$), represented for four frames in sequence.

6.3.3 The Blade-To-Blade Plane

The VAWT aerodynamics described by means of the 2D plane measurements, is further investigated in the blade-to-blade plane (B2B), in which only the midspan traverse is sampled on the z-axis, but more traverses are instead placed along the x-direction, to observe the streamwise evolution of the flow quantities, and to see clearly the vortex shedding mechanism at midspan. For the B2B plane description, the present section will focus only on the two operating conditions at constant rotational speed ($\omega = 400\ rpm$).

$$\text{Opt. Load.} : v_0 = 9.0\ m/s \rightarrow \lambda = 2.4$$
$$\text{Low Load.} : v_0 = 14.2\ m/s \rightarrow \lambda = 1.5$$

Again, the results are presented in a dimensionless reference frame, in this case, both the x and y axes are made non-dimensional with respect to the machine radius. First the phase-average flow quantities will be presented, and then their time evolution will be discussed in detail.

6.3.3.1 The Blade-To-Blade Plane comparison of phase-averaged flow quantities at different λ

In the present section, the phase-average quantities will be presented. In Fig.6.24 the dimensionless velocity and the yaw angle are reported for

the two operating conditions. Here, the wake is perfectly analogous to the one measured in the 2D plane (6.11), with a much deeper velocity deficit and steeper velocity gradients at the wake borders for the optimal loading case. The leeward region is particularly visible for the low loading case. Here, thanks to the B2B plane measurements, it is possible to see the streamwise evolution of the high momentum leeward wake, which tends to push the high momentum region towards the left. As expected from the momentum theory, the wake tends to expand transversely as it proceeds along the streamwise, and this is visible not only from the velocity contours, but also from the yaw angle ones. As a matter of fact, thanks to the symmetric yaw angle contour legend, it is possible to appreciate the bulk flow moving towards the positive y-direction on the leeward region, and towards the negative y-direction in the windward part. Looking carefully at the yaw contours of Fig.6.24, it is also possible to notice regions in the core of the wake where the flow angle is alternated in sign. These parts are the evidence of the presence of a vortex, whose kernel follows the opposite gradient lines. Recall that the B2B plane refers only to the midspan traverse, which means that here the tip region is not visible, and so its vortex shedding.

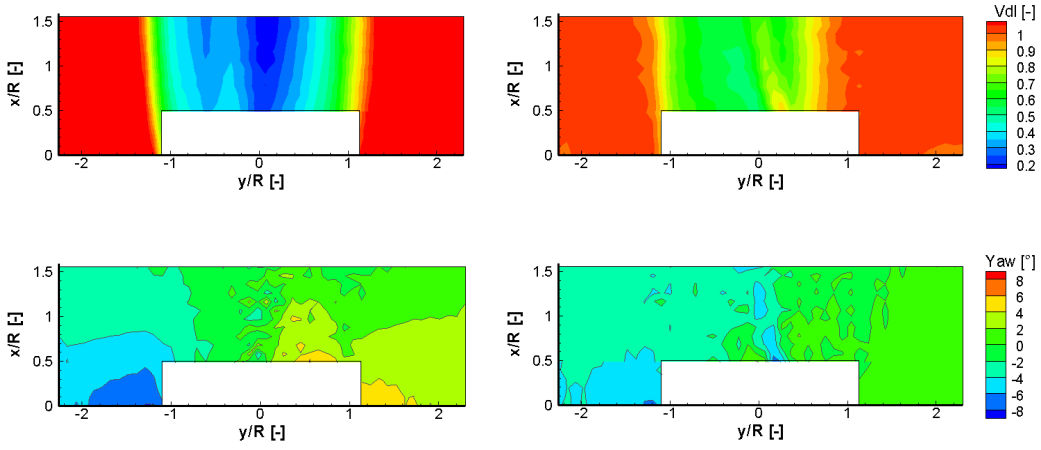

Figure 6.24: Dimensionless velocity and Yaw angle in the B2B plane at $\omega = 400\ rpm$ for $\lambda = 2.4$ (a) and for $\lambda = 1.5$ (b).

Another fundamental topic is turbulence. The deterministic structures and the Reynolds stress tensor are reported in Fig.6.25. Recall that the Reynolds tensor components have the units of a velocity squared, which is

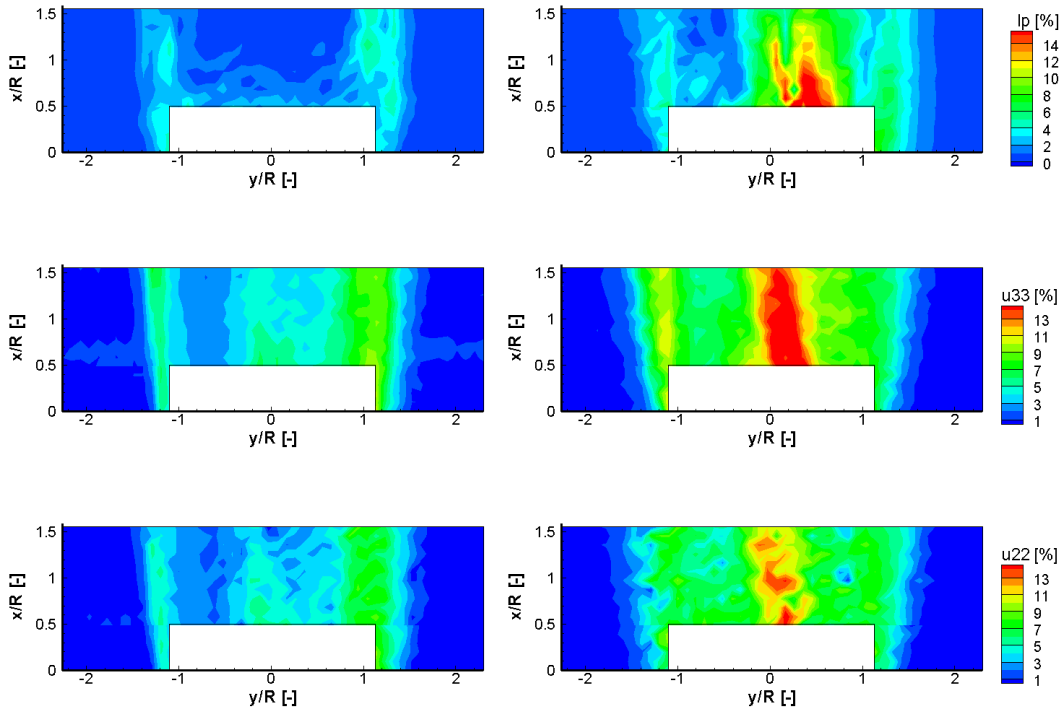

Figure 6.25: Turbulence intensities and Reynolds stress tensor in the B2B plane at $\omega = 400\ rpm$ for $\lambda = 2.4$ (a) and for $\lambda = 1.5$ (b).

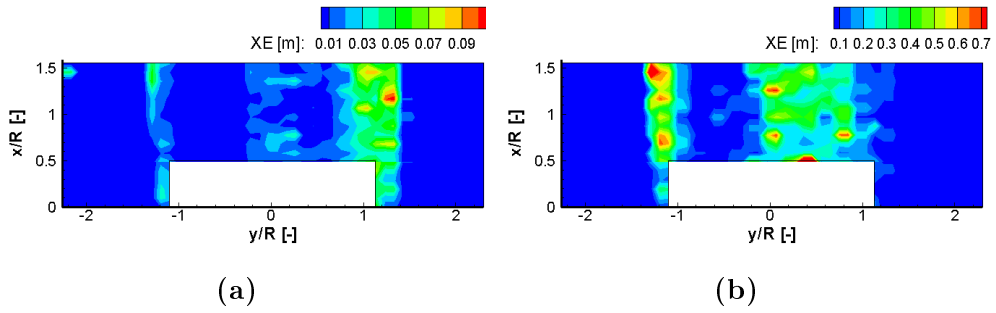

Figure 6.26: Turbulent integral length scale in the B2B plane at $\omega = 400\ rpm$ for $\lambda = 2.4$ (a) and for $\lambda = 1.5$ (b).

a stress divided by density. The differences between the two loading conditions are evident, the low loading case is affected by particularly intense periodic structures, shed mainly in the leeward region, which are much weaker in the optimal loading condition. Furthermore, in the low loading

case, the whole wake witnesses a strong unresolved turbulence, together with high Reynolds stresses, while for the optimal working condition, the regions of higher turbulence correspond to the wake margins, where velocity gradients are steeper. It should be noticed that the outcomes reported in Fig.6.25, are in line with the measurements of the 2D plane in Fig.6.11 and 6.12. Together with turbulence statistics and the Reynolds stress tensor components, the other parameter that has been computed for the B2B plane is the turbulent integral length scale. The result of the elaboration is reported in Fig.6.26. Please notice that in this picture, the two contours have a different scale, and notice that the vortical structures arising in the low loading condition are much larger than those produced by the optimal one, with a different distribution. As expected from the results of the Reynolds stresses, the optimal loading case evidences small vortices and concentrated mainly at the edges of the wake, larger ones on the leeward side and smaller ones on the windward side. On the other hand, the low loading condition is affected by larger scale vortices triggered by dynamic stall and distributed also in the core of the wake.

6.3.3.2 The Blade-To-Blade Plane comparison of unsteady flow quantities at different λ

Even more interesting is the elaboration of the unsteady data for both loading cases. In Fig.6.27 and in Fig.6.28, four velocity time frames are reported for both the optimal and the low loading case.

The unsteady data elaboration for the B2B plane puts in evidence the same features commented for the 2D plane. Once again, the optimal loading condition looks almost steady, since its velocity fluctuations are hard to notice. On the other hand, the wake of the low loading operating point is strongly unsteady, and the flow detachment at the leeward region is clearly visible also from the velocity contours. Notice how different is the time evolution from the simple phase-average map. Even from these first results it is evident how important it is to evaluate the time evolution of the wake of the VAWT machines, which have inherently a strong unsteady character. The additional advantage that is difficult to catch when looking at the wake in the 2D plane is the streamwise extension of the low momentum structures, and how they interact with the freestream region.

What can be foreseen from the unsteady velocity contours, is instead much clearer looking at the yaw distribution with time on the B2B plane. In Fig.6.29 the unsteady flow angle at optimal loading is reported, while the one for low loading is represented in Fig.6.30. The yaw angle distribution is indeed of crucial importance, and this is why eight frames are

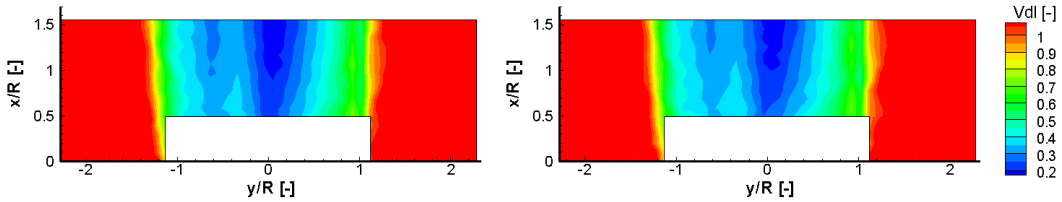

(a) Frame 01 (b) Frame 10

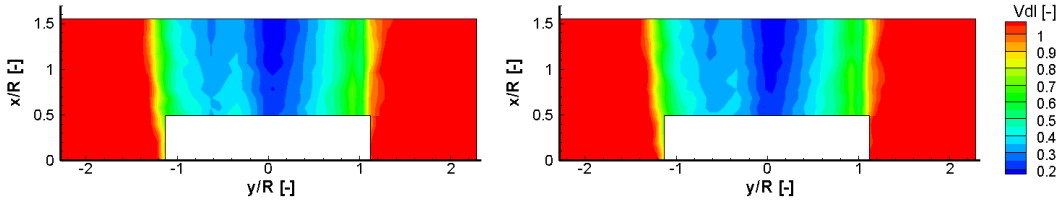

(c) Frame 20 (d) Frame 30

Figure 6.27: Instantaneous dimensionless velocity at $\lambda_{opt} = 2.4$ ($v_0 = 9\ m/s$; $\omega = 400\ rpm$), represented for four frames in sequence.

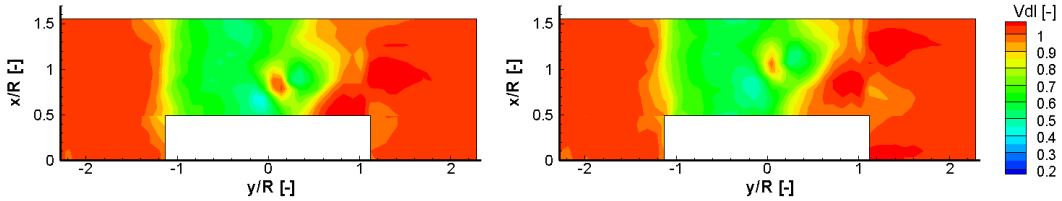

(a) Frame 01 (b) Frame 10

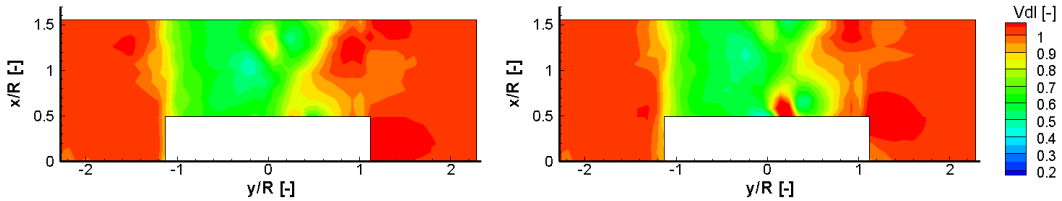

(c) Frame 20 (d) Frame 30

Figure 6.28: Instantaneous dimensionless velocity at $\lambda = 1.5$ ($v_0 = 14.2\ m/s$; $\omega = 400\ rpm$), represented for four frames in sequence.

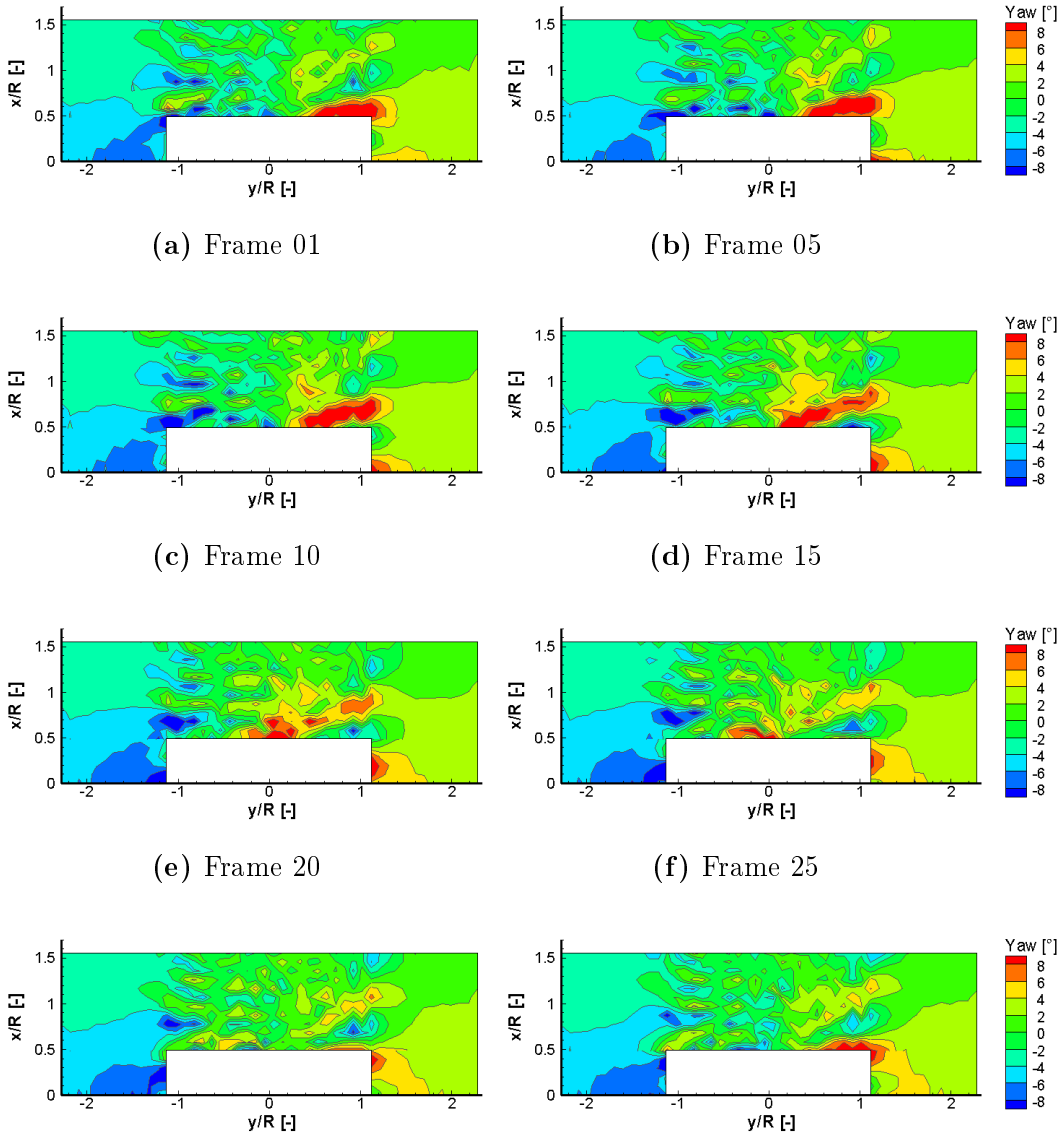

(a) Frame 01 (b) Frame 05

(c) Frame 10 (d) Frame 15

(e) Frame 20 (f) Frame 25

(g) Frame 30 (h) Frame 35

Figure 6.29: Instantaneous yaw angle at $\lambda_{opt} = 2.4$ ($v_0 = 9\ m/s$; $\omega = 400\ rpm$), represented for eight frames in sequence.

reported.

Please notice that the two series of contours are plotted at a different scale, to make the phenomena more evident in each case. Even if in the optimal loading case the velocity looks particularly steady, the direction

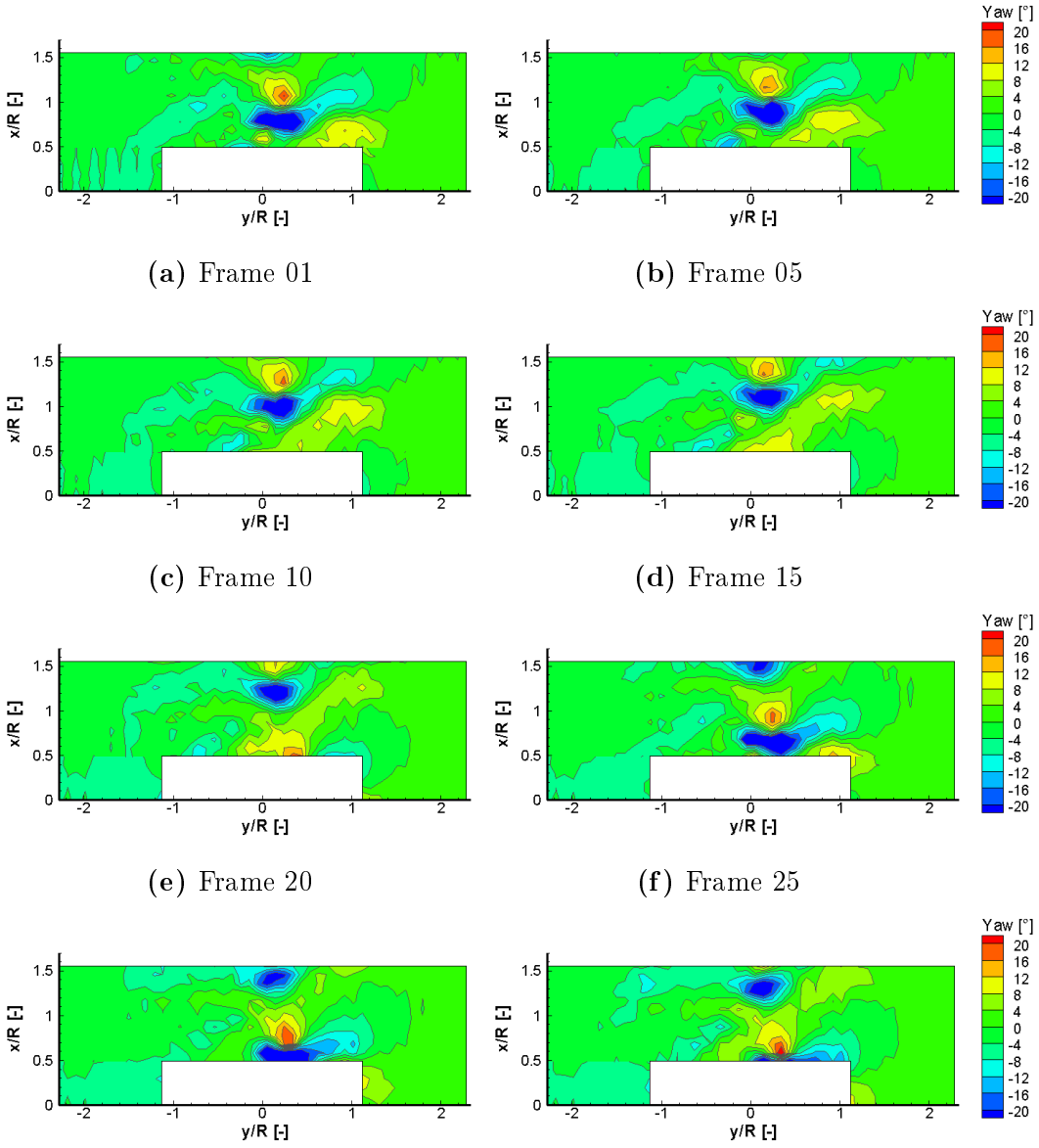

(a) Frame 01 (b) Frame 05

(c) Frame 10 (d) Frame 15

(e) Frame 20 (f) Frame 25

(g) Frame 30 (h) Frame 35

Figure 6.30: Instantaneous yaw angle at $\lambda = 1.5$ ($v_0 = 14.2\ m/s$; $\omega = 400\ rpm$), represented for eight frames in sequence.

of the flow is really unsteady. Fig.6.29 puts in evidence the formation of structures that are periodically shed on both sides of the machine. Those on the leeward part are stronger and rotating counterclockwise, while those on the windward side are weaker and rotating clockwise with

respect to the observer. This observation highlights again that, for optimal loading, unsteadiness affects mainly the edges of the wake. On the other hand, for the low loading case, the situation is different. The largest vortices are shed in the leeward region and are convected streamwise with a slight inclination towards the windward half of the wake. Compared to this vortex, the structures produced by the shear layers at the borders of the wake become negligible. This last observation is remarked again in the CFD studies in [5], in particular, with reference to Fig. 6.13. In this case, the experimental data are in line with the CFD simulation, and the structures in Fig. 6.30 are counterrotating, which is due to the simultaneous detachment that may take place at the same turbine phase.

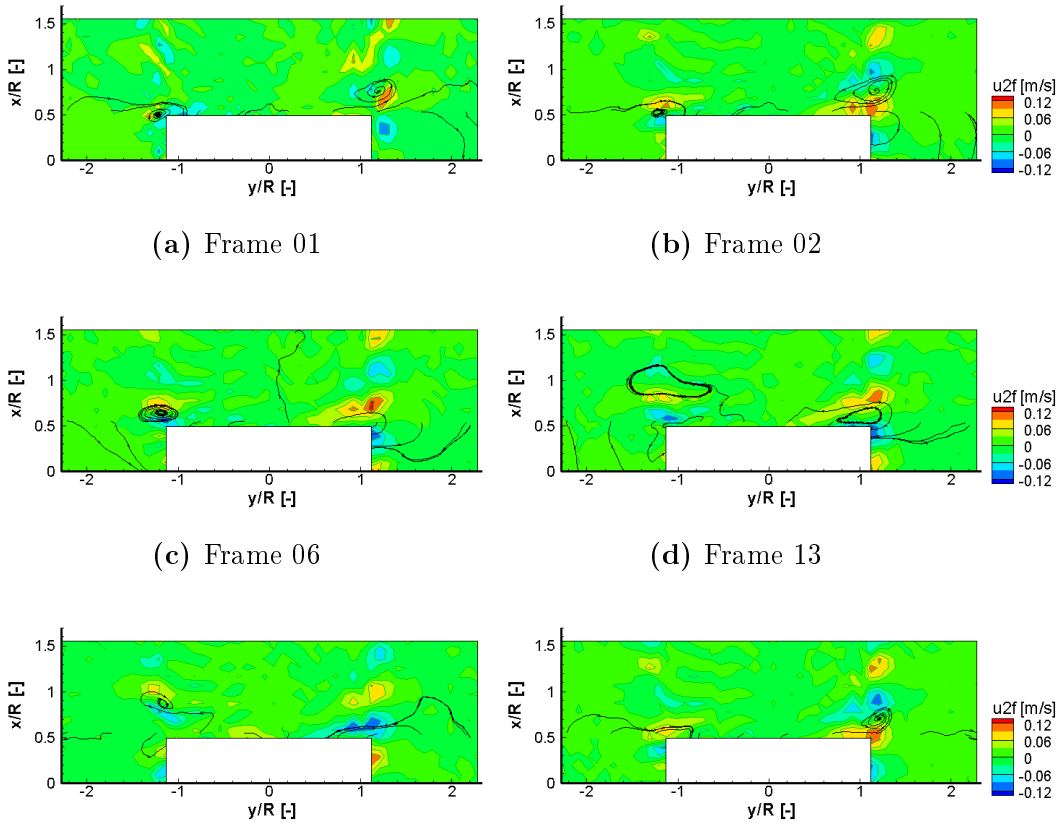

(a) Frame 01 **(b)** Frame 02

(c) Frame 06 **(d)** Frame 13

(e) Frame 24 **(f)** Frame 38

Figure 6.31: Fluctuating transversal velocity at $\lambda_{opt} = 2.4$ ($v_0 = 9\ m/s$; $\omega = 400\ rpm$), represented for four frames in sequence and with the fluctuating streamlines superimposed.

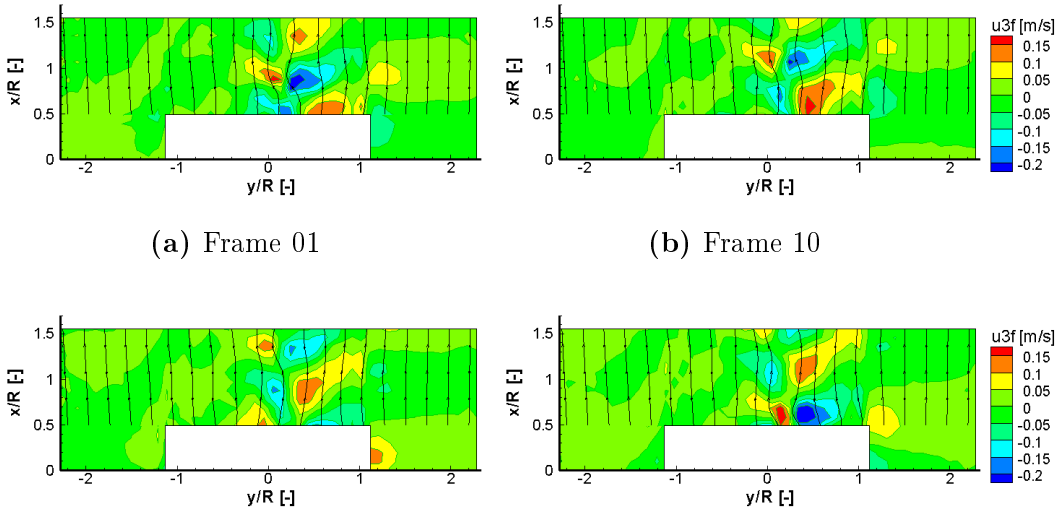

(a) Frame 01 (b) Frame 10

(c) Frame 20 (d) Frame 30

Figure 6.32: Fluctuating streamwise velocity at $\lambda = 1.5$ ($v_0 = 14.2\ m/s$; $\omega = 400\ rpm$), represented for four frames in sequence and with the main flow streamlines superimposed.

These results, even more than the velocity one, proof how the phase-average study on the VAWT wake is not sufficient to have a complete understanding of the fluid-dynamic phenomena. A way to visualize even more clearly the vortical structures shed by the turbine, is to plot the periodic part of the two velocity components. These fluctuations are obtained by subtracting the time-mean term to the phase-averaged value. The result is the deterministic unsteadiness, and this helps visualize the periodic shedding of counterrotating vortices, as reported in Fig.6.31 and 6.32.

Besides, in these pictures, the streamlines are superimposed to the two fluctuating velocity components. For the optimal loading case, the velocity along y is represented, while the low loading one shows the streamwise component. If the purpose is to put in evidence the vortical structures over the mean flow, the two velocities can be then considered equivalent. For the purpose of putting in evidence the vortical structures, to Fig.6.31 it is more effective to couple the streamlines of the periodic velocities themselves, this way it is possible to see the trace of the vortex formation. In the sequence of Fig.6.31, the reported frames are not equidistant, but they have been chosen with the intention of focusing on the most relevant moments of the blade passage. Notice that there are instants of time close

to the beginning and the end of the period, in which the streamlines are more likely to curl up on the right-hand side of the wake. These shall be the points of time when the blade passes through the leeward region. To the purpose of the low loading condition reported in Fig.6.32, instead, it seems more effective from a graphical point of view to represent the streamlines of the main flow.

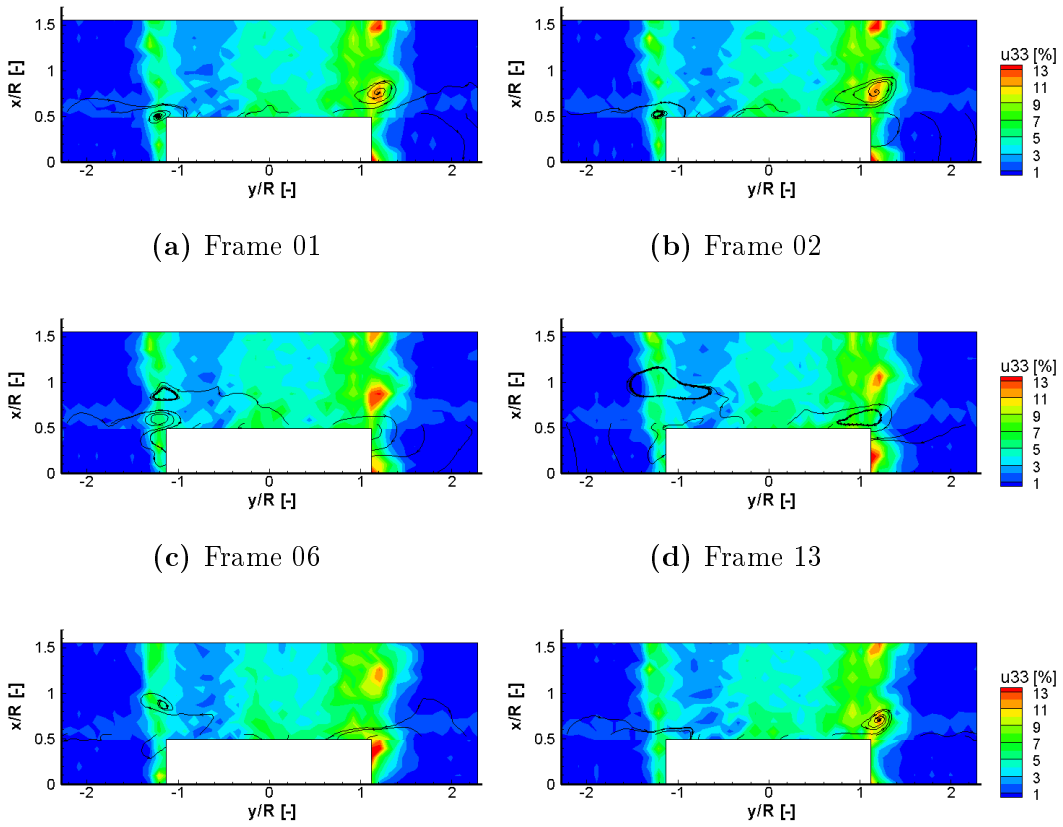

(a) Frame 01 **(b)** Frame 02

(c) Frame 06 **(d)** Frame 13

(e) Frame 24 **(f)** Frame 38

Figure 6.33: Streamwise Reynolds stress at $\lambda_{opt} = 2.4$ ($v_0 = 9\ m/s$; $\omega = 400\ rpm$), represented for four frames in sequence and with the fluctuating streamlines superimposed.

This way it is possible to evidence the distortion of the bulk flow corresponding to the shedding of the vortex. Once again, it is possible to notice the difference between optimal loading and low loading conditions. The first one shows weak structures at the edges of the wake, while the second one experiences stronger vortex shedding and located more inside the core

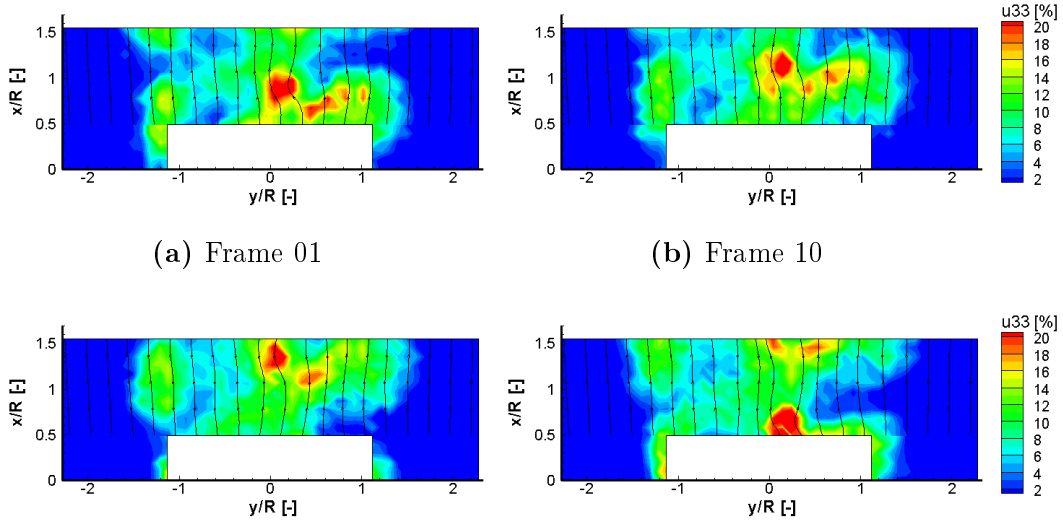

(a) Frame 01 (b) Frame 10

(c) Frame 20 (d) Frame 30

Figure 6.34: Streamwise Reynolds stress at $\lambda = 1.5$ ($v_0 = 14.2\ m/s$; $\omega = 400\ rpm$), represented for four frames in sequence and with the main flow streamlines superimposed.

of the wake. In this second case, the phenomenon is so evident that just four equidistant frames are sufficient to describe it. Another contour that well matches with the streamlines distribution is the streamwise component of the Reynolds stress tensor, analogous to the turbulence intensity. Fig.6.33 and 6.34 present the phenomenon with the same streamlines superposition of Fig.6.31 and 6.32 respectively.

Thanks to the turbulence plot, for the optimal loading condition, it is possible to observe that the the rolling up of the streamline corresponds to the high turbulence region at the edge of the wake, either in the leeward or in the windward zone, and it is well captured by the plotting software when it first detaches from the machine blade. On the other hand, for the low loading case, the mean flow streamlines show a strong deviation as the core of the vortex is shed from the turbine.

A final plot to make even clearer the direction of rotation of these vortical structures is the vector plot, this time represented for the sole frame 20, for both loading conditions, in Fig.6.35. Here, in particular, the vortex direction of rotation is put in evidence. For the optimal loading condition, small counterrotating vortices arise at the wake edges, while the core of the wake is particularly similar to the freestream flow. In the low loading case, instead, the structures that arise in the core of the wake

show a much clearer trend. There is an upper structure rotating clockwise, a lower one rotating counterclockwise, and again another swelling on the leeward side rotating clockwise.

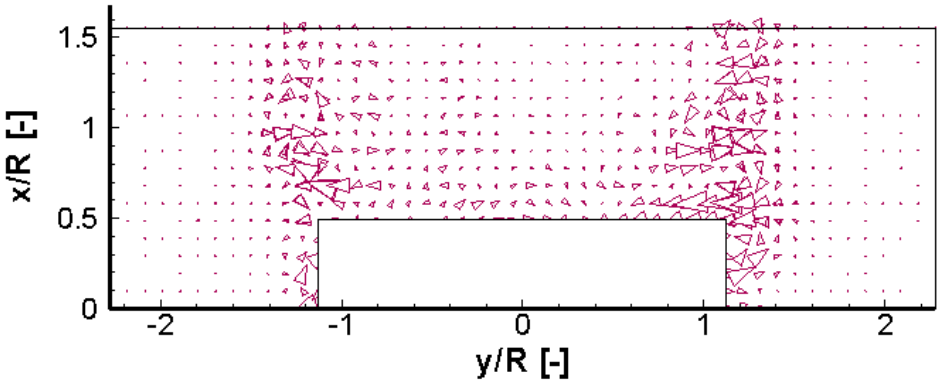

(a) $\lambda = 2.4$

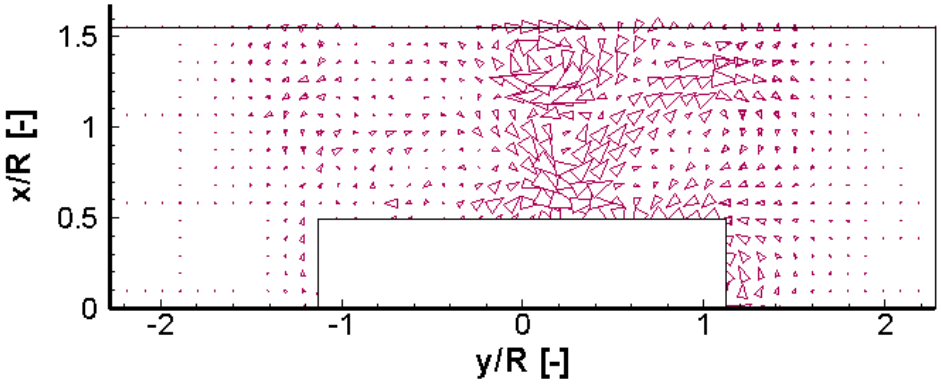

(b) $\lambda = 1.5$

Figure 6.35: Vector plot at $\lambda = 2.4$ ($v_0 = 9\ m/s;\ \omega = 400\ rpm$) (a) and for$\lambda = 1.5$ ($v_0 = 14.2\ m/s;\ \omega = 400\ rpm$) (b).

6.4 The Axial-Flow Turbine Stage

In the present section, the results obtained from the measurements downstream of the axial-flow turbine stator (GT), will be presented. Velocity magnitude, yaw angle, and the 2×2 Reynolds stress tensor have been derived, and their general features will be discussed. Remind that, as discussed in the data processing chapter (Ch.5), the Reynolds stress components have been obtained in a simplified way for the axial turbine stage, compared to the VAWT case, and this is because in the VAWT the measurements are taken downstream of a rotor, characterized by high periodic unsteadiness, while the GT measurements regard the wake of a statoric cascade, whose only periodic unsteadiness is produced by the pressure field generated by the rotor, and propagating upstream of the rotor blades leading edge in subsonic flow conditions. Hence, for the GT flow quantities, the most interesting results are the time-averaged ones, and hence no time dependency will be considered for these phenomena. The streamwise direction will be addressed as x_3, while the crosswise, corresponding to the tangential direction, is addressed as x_2. The complete map has been derived for the acquisition session with three probe rotations, and hence it was obtained with an iso-constrained problem solution. In any case, an acquisition run with nine probe rotation was done as well, and in the next paragraph a comparison of the two solutions is carried out.

When measuring velocity and yaw angle, some critical issues arose, probably connected to the high speed and non-isothermal flow discharged by the cascade, and the Appendix is dedicated to this topic. In Fig.6.36 and 6.37, the Reynolds stress tensor, the overall velocity fluctuation and the turbulence intensities in the two flow directions are reported.

From a first observation of the variables represented in the contours, the viscous wake shed by the blade can be clearly seen laying in the black trace. As a matter of fact, this is the region of highest turbulence intensity, due to the mixing of the flows coming form the pressure and suction side of the blade, which are characterized by different velocities, and the shear layers produced by the steep velocity gradients give rise to high turbulence intensity. Furthermore, significant turbulence levels, are given by the high mixing associated to the tip and hub vortices.

The comparison of the streamwise and crosswise components as well is particularly interesting. The ratio of the two diagonal components is presented in Fig.6.38. From such graph, it is possible to notice that even if the two components seem to distribute on similar levels, their ratio proofs that the streamwise prevails on the crosswise in the wake region, while in

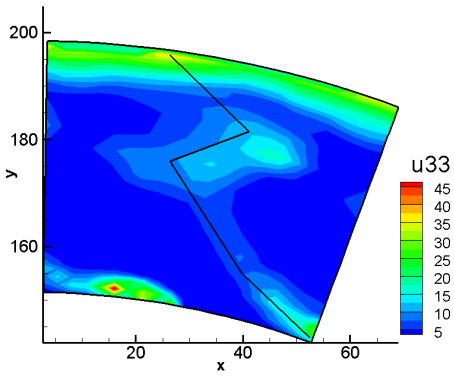

(a) Average quadratic fluctuation of streamwise velocity component ($u_{33} = \overline{u_3'^2}$).

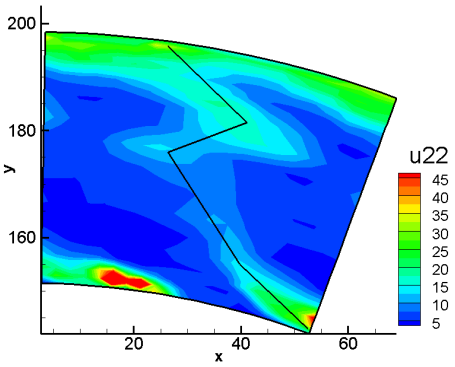

(b) Average quadratic fluctuation of the crosswise velocity component ($u_{22} = \overline{u_2'^2}$).

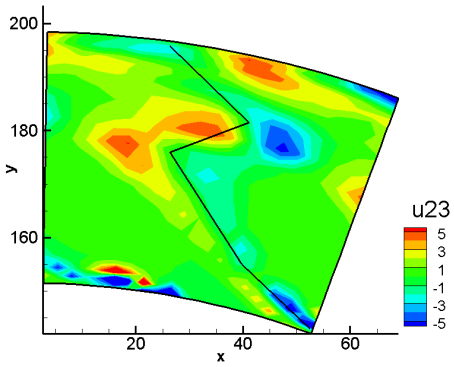

(c) Averaged product of the streamswise and crosswise fluctuations ($u_{23} = \overline{u_2' u_3'}$).

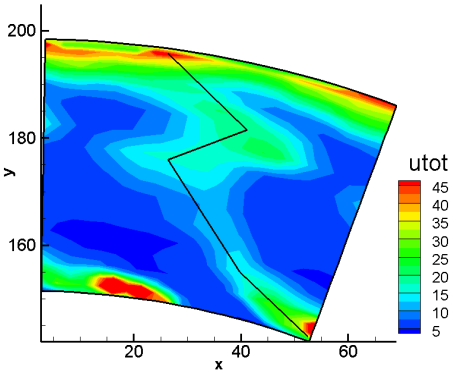

(d) Averaged total velocity quadratic fluctuation ($u_{tot} = \sqrt{\overline{u_3'^2} + \overline{u_2'^2}}$).

Figure 6.36: Reynolds stress components and total velocity fluctuation measured with the Hot wire.

the freestream the situation is reversed. Such observation suggests that in the wake, the mixing process takes place with higher gradients, and hence with higher turbulent stresses along the streamwise direction, while along the crosswise the velocity variations are smaller. On the other hand, in the freestream region, the streamwise component experiences a much more homogeneous pattern compared to the crosswise. This trend is shown in 6.38, where the ratio between u_{33} and u_{22} is represented. Please notice that the core at the bottom-left side is not significant, since its high value

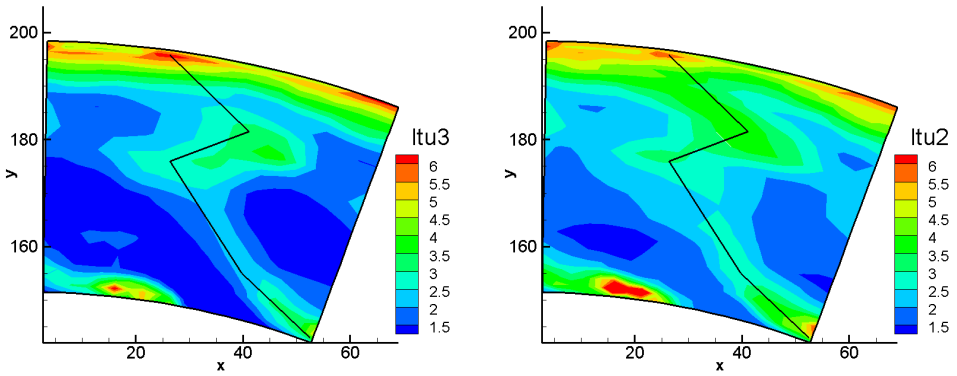

(a) Streamwise turbulence intensity. **(b)** Crosswise turbulence intensity.

Figure 6.37: Hot wire turbulence intensities in the streamwise and in the crosswise directions.

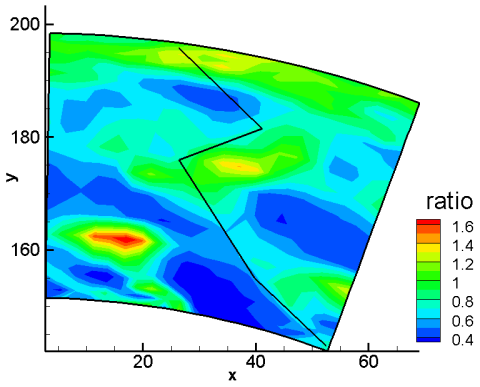

Figure 6.38: Ratio between the streamwise and crosswise component (u_{33}/u_{22}.)

is for sure given by the ratio of very small numbers.

In order to clearly visualize the components fluctuations while crossing the wake, in 6.39 the midspan profile of all the three Reynolds components is shown.

As already commented for the VAWT (Sec.6.3.2.1), the extra-diagonal term of the Reynolds stress is expected to arise in regions of high polarity of the flow [8]. This is again what happens here, downstream of the statoric cascade in the mixing zone, in the most dissipative turbulent region. As a matter of fact, the extra-diagonal term u_{23} changes sign when crossing

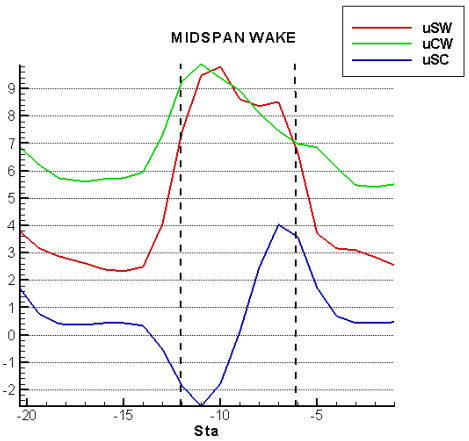

Figure 6.39: Midspan profile of the Reynolds stress components.

the wake, and deeper explanation for this case is given by 6.36c, where the velocity defect associated to the wake is represented in the blade-to-blade plane.

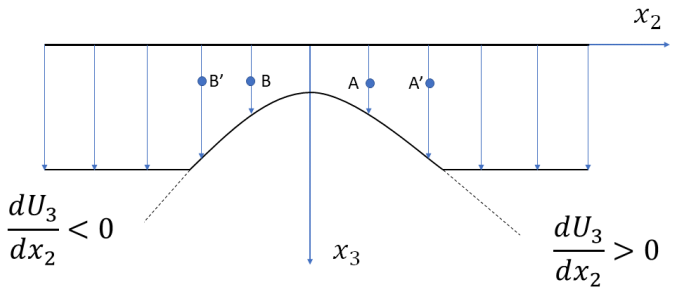

Figure 6.40: Wake velocity defect in the blade-to-blade plane of the GT.

Let us suppose that a particle A moves to A', such that it has a positive crosswise velocity fluctuation ($u'_2 > 0$); since its streamwise velocity is lower than the one of A', this particle is reducing the overall streamwise velocity ($u'_3 > 0$). It follows that:

$$u_{23} = \overline{u'_3 u'_2} < 0 \qquad \text{where } dU_3/dx_2 > 0 \tag{6.2}$$

The same result is obtained considering the opposite motion, from A' to A. On the other hand, moving from B to be B', both velocity fluctuations are negative, since the crosswise velocity in B' is lower than the one of B.

$$u_{23} = \overline{u_3' u_2'} > 0 \qquad \text{where } dU_3/dx_2 < 0 \tag{6.3}$$

It is fundamental to understand how this behavior is related to turbulence. On the right side of the wake, the streamwise velocity is increasing with respect to the positive crosswise direction ($db/dt > 0$); then the negative u_{23} is trying to reduce this gradient, preventing a further increase of the streamwise velocity. On the other side of the wake, where u_3' is decreasing with the positive crosswise direction, the $u_{23} > 0$ is again contrasting the trend imposed by the gradient, and it tends to increase the streamwise velocity u_3'. It can be concluded that this component is clearly contributing to the diffusion effect associated to turbulence, which tends to decrease the gradients, thus flattening the velocity dishomogeneities. All these features are very well captured by the hot wire measurements, by means of the data processing proposed in sec. 5.7.

6.4.1 Comparison between iso- and over-determined problem

To investigate the accuracy of the iso-determined problem, obtained with just three probe rotations, few span measurements were acquired with nine rotations, and hence with a system of equations quite strongly over-determined. Such comparison can be observed in Fig.6.41 for example for the case of the u_{33} Reynolds stress.

The points of the grid acquired for the nine rotations are just for four radial positions, and to facilitate the comparison as much as possible, the midspan traverses have been chosen for such test. Looking at Fig.6.41, the two results are consistent, and aligned. This means that both resolutions give the correct representation of the wake turbulent phenomena, and since the nine rotations algorithm requires three times the acquisition time of the three rotations tests, the trade-off is definitely in favor of the iso-constrained resolution.

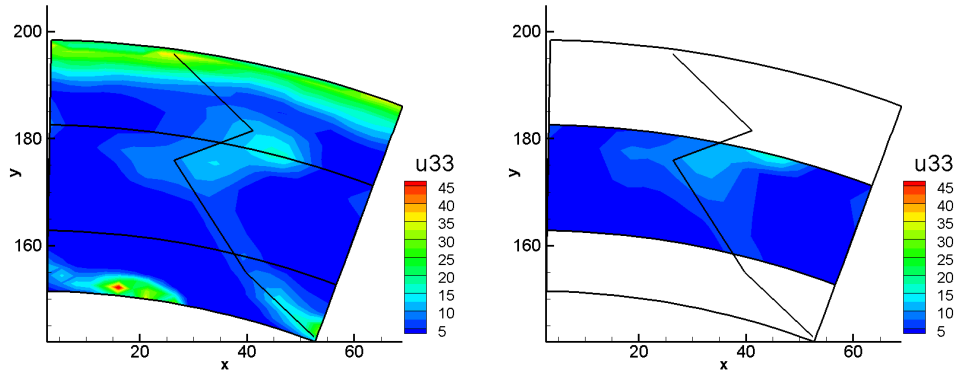

(a) Iso-determined system resolution. **(b)** Over-determined system resolution.

Figure 6.41: Comparison between iso-determined system (a) and over-determined one (b).

Chapter 7

Conclusions and Future Developments

The present Thesis work has been mostly focused on the elaboration of the raw data collected in the past experimental campaign on the H-shaped Vertical Axis Wind Turbine (VAWT). The aim was to to widen the spectrum of data-processing techniques to improve the flow field characterization, especially from an unsteady point of view. The results obtained are definitely satisfactory, they have opened the way to highlight flow and turbulence properties not straight-forward to extract, but extremely relevant to discuss. These efforts were mainly targeted to the innovative blade-to-blade measuring plane, sampled for the first time in winter 2016/17. As a matter of fact, along this plane, it was possible to put in evidence the streamwise evolution of the vortical structures, and diverse graphical artifices have been applied to these measurements to make the periodic shedding phenomenon clearer and clearer. On the overall, from the point of view of the VAWT data elaboration, the results are in line with the expectations, and they suggest to proceed with the investigations on the blade-to-blade plane, that has given such promising results so far. A possible future development to add value to this new innovative measurement plane could be to sample it with a slanted hot wire. This kind of wire was proved to be useless for the evaluation of the pitch angle, which means that the average measurement cannot be considered reliable, but the fluctuations around that average may be accurate, as demonstrated by the results obtained on the TC test rig. In that case as well, issues arose when measuring the velocity and yaw fields, but the Reynolds stress tensor was in accordance with the other probe measurements. The same thing is expected to happen for the slanted wire when measuring velocity fluctuations around the average, which is the key input for the calculation

of the complete 3D Reynolds stress. In this case, a high degree of overdetermination of the solving system is required, maybe with nine rotations for three unknowns. Another interesting chance to use the blade-to-blade plane concept could be to sample other planes parallel to the midspan one. For instance, a very interesting region to investigate could be the tip, where a lot of complex vortices are being shed. The idea is thus to slowly pass from a 2D to a 3D experimental characterization of the VAWT wake.

The results on the axial-flow turbine stage, instead, show a different outcome. In this case, a lot of criticalities arose, and the hot wire was not able to give reliable measurements for the average flow field in terms of velocity magnitude and yaw angle. On the other hand, the results of the Reynolds stresses have been found fully reasonable and, hence, will offer the opportunity for investigating the capabilities of the FRAP probe for turbulence measurements. In particular, thanks to the hot wire measurements, the hub structures are clearly visible, and the crosswise and streamcross stresses can be computed with reliable results. The conclusion that comes from this second campaign is that the hot wire anemometer cannot be used in an axial turbine stage as the TC rig one in the same way as it is used in the wind. The two flows are really different in terms of temperature and velocity. As a matter of fact, the VAWT operates at ambient temperature and at a maximum wind speed of 15 m/s, while the turbine flow enters the stator at 35°C and runs over the wire at $\mathrm{Ma} = 0.3 \div 0.4$. The precautions undertaken during this campaign, such as the high temperature King calibration and the zero velocity temperature dependence, were not enough to achieve a satisfactory understanding of the probe behavior in such working conditions. Thus, with the idea of supporting the FRAPP in the future campaigns, it is of fundamental importance to carry out further tests and studies to deepen the knowledge on the use of hot wires in high-temperature high-speed flows. A starting point, for instance, could be to test the probe downstream of the rotor, where the flow is unsteady, but temperatures and velocities are more moderate.

Finally, the wish of the author is that the new routines developed with this work to make the LFM software more accurate and complete, together with the concerns raised on alternative applications of the hot wire, will be useful for the interpretation of the flow features in the future experimental campaigns, and will encourage further research in the field.

Appendices

Appendix A

Critical issues in the velocity field measurements downstream of the GT stator

The experimental campaign carried out on the GT had the objective of sampling the stator wake and compare the HW results with the FRAPP ones, mainly for what concerns turbulence. To do this, only two of the five operating points were chosen, in order to avoid too high air temperatures and too high flow velocities. This was the first time that the gas turbine of the LFM was investigated with a hot wire. Up to now, all the experimental campaigns on the TC rig were carried out with the FRAPP, while the HW was used mainly for wind turbine tests. This is why during the campaign, the FRAPP was used as a reference, to validate the velocity field measurements of the HW. For the GT operation, the HW probe was pre-rotated with respect to the axial direction of 75°. This way, the hot wire was aligned with the main flow direction, and this is a first simple effective method to make the probe sensitive to the deviations from such direction. Another more sophisticate possibility is to pre-rotate the probe of the expected circumferential average flow direction. This was computed from the FRAPP measurements, calculating an average yaw angle weighted on the mass flow rate at every radial position. This way, a spanwise average is calculated, and used as the probe pre-rotation. Both methods were implemented for both operating conditions, several times and for different probe rotations, to look for a consistent explanation of the observed behavior of the HW. Of all the sets of data acquired, in this chapter are reported only the most relevant ones to explain the critical issues that arose during this test campaign, and to give the reason why the velocity field measurements and the OP-4 working condition were not

presented in the results discussion.

In the following lines the history of the GT campaign is reported, and the tests are listed in the same order in which they have been carried out. The test code contains the operating point (OP4 or OP5), and a sequential serial letter of the test. For simplicity, only the yaw angle results are cited in this chapter, since considered well representative of the problem.

- OP4-A: Pre-rotation = 75°, 3 rotations, 23 radial position (all the span)
- OP5-A: Pre-rotation = 75°, 3 rotations, 23 radial position (all the span)

For these two tests, the calibration matrix obtained at ambient temperature was applied. Only afterwards, a second calibration matrix was applied, this time depending at the test temperature of 35°C, as discussed in Sec.3.2.3. The results of these first tests are reported in Fig.A.1, from which the shift between the two curves is clearly evident. In particular, the maximum shift in OP4 is of $-2°$ and of $3°$ in OP5.

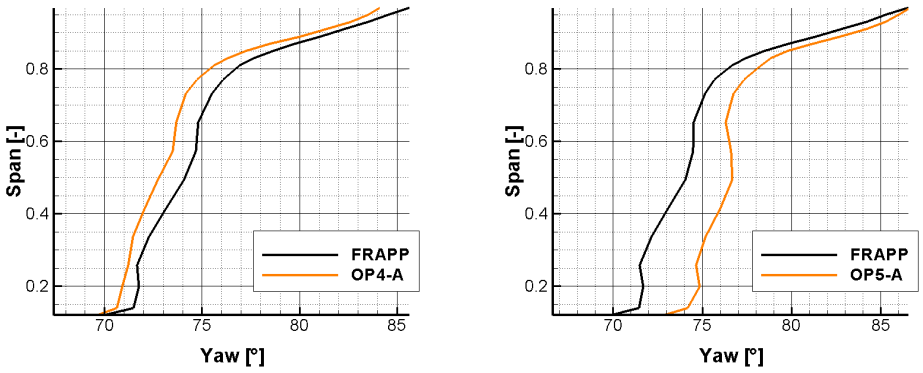

(a) OP4-A **(b)** OP5-A

Figure A.1: The A series of acquisition for OP4 (a), and OP5 (b).

The reasons for this shift were unknown, but some hypotheses were considered, such as the effect of temperature, the choice of the numbers of rotations and the wire deformation during the test. Thus, further tests were repeated a week later:

- OP5-B: Pre-rotation = 75°, 3 rotations, 23 radial position (all the span)

- OP4-B: Pre-rotation = 75°, 3 rotations, 23 radial position (all the span)

The results obtained from these tests are reported in Fig.A.2, where the comparison with the A series of acquisition is reported. Unfortunately, this second testing session did not give an answer to the phenomena taking place inside the wire. Moreover, the shift became even more evident, with also a sign change for OP5.

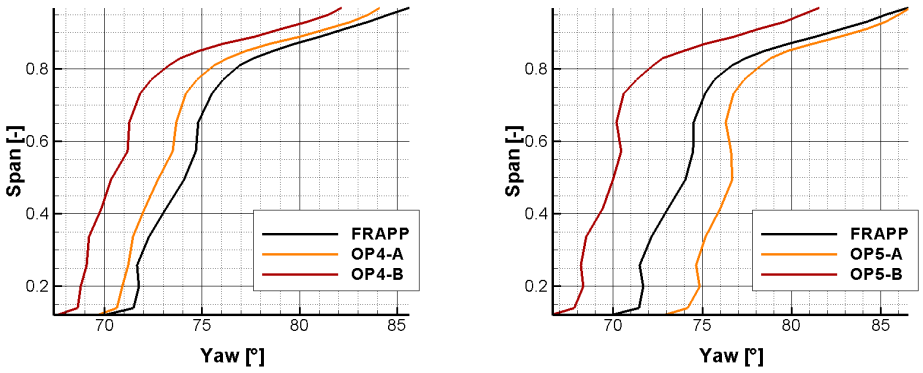

(a) OP4-A **(b)** OP5-A

Figure A.2: The A and B series of acquisition for OP4 (a), and OP5 (b).

Hence, after these, further tests were carried out to verify the repeatability of the results at the same operative points. To test this, it was not necessary to cover the whole measuring grid, but just a stator position was sampled several times for all the radial coordinates. Hence, these operating conditions are not averages, but they are punctual values, and they shall not be compared with the other A and B test series. Of all the tests that were carried out with this approach, this time with a 35°C King's law, and only the most representative ones are reported here in chronological order:

- OP5-R ; OP5-S ; OP5-T ; OP5-U
- OP4-O ; OP4-P ; OP4-Q ; OP4-R
- OP5-V

This testing order is not casual. One of the hypotheses was that the higher Mach numbers of the OP4 test, together with the high temperatures, were deforming the wire. Hence, from this perspective, it was a

good idea to test OP5 before and after a few tests in OP4, to look for an experimental evidence to to support this hypothesis.

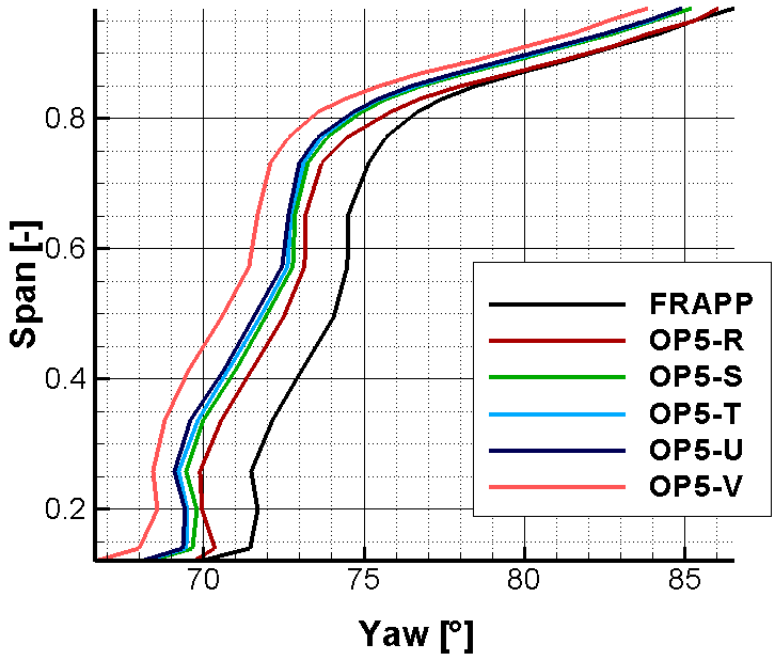

Figure A.3: OP5 tests before and after running OP4.

The results of such procedure are those reported in Fig.A.3. From this plot, it is possible to notice that the curves of OP5 from R to U are nearly overlapped, even if a certain shift from the FRAPP curve still exists. The last acquisition (OP5-V), instead, shows a shift of around 2° from the first group. This observation suggests the presence of permanent deformations in the hot wire, induced by the high stresses of the OP4 tests on the extremely delicate wire sensor. This is finally the most accredited hypothesis for this unexpected behavior of the wire.

Another issue that arose during the gas turbine campaign is the variation of the zero of voltage along the turbine span with the plant completely still. This observation suggested the temperature calibration of the zero voltage discussed in Sec.3.2.2. All the zero voltages used for the data elaboration in the GT were then computed through this calibration, such that the results could not be affected by the uncertainty of the zero capturing procedure.

In conclusion, the experiments show that there has to be a negative

effect of the high temperatures combined with high velocities, that may cause permanent deformations in the wire, which could be responsible for the continuous shifts in the measured quantities. The conditions in which the wire is working in the considered operative points are not completely known yet, and further tests and studies are required in order to better understand the reasons that lead to a non-consistency of the results.

Bibliography

[1] C. S. Ferreira. "The near wake of the VAWT 2D and 3D views of the VAWT aerodynamics". In: *T.U.Delft Thesis* (2009), p. 304 (cit. on pp. viii, xii, xxxii, 115).

[2] H. Y. Peng, H. F. Lam, and C. F. Lee. "Investigation into the wake aerodynamics of a five-straight-bladed vertical axis wind turbine by wind tunnel tests". In: *Journal of Wind Engineering and Industrial Aerodynamics* 155 (2016), pp. 23–35 (cit. on pp. viii, xxxii).

[3] L. Battisti et al. "Aerodynamic Measurements on a Vertical Axis Wind Turbine in a Large Scale Wind Tunnel". In: *Journal of Energy Resources Technology* 133.3 (2011), p. 031201 (cit. on pp. viii, xxxii).

[4] V. Dossena et al. "An Experimental Study of the Aerodynamics and Performance of a Vertical Axis Wind Turbine in a Confined and Unconfined Environment". In: *Journal of Energy Resources Technology* 137.5 (2015), p. 051207 (cit. on pp. viii, xxxii).

[5] G. Persico et al. "Time-Resolved Experimental Characterization of the Wakes Shed by H-Shaped and Troposkien Vertical Axis Wind Turbines". In: *Journal of Energy Resources Technology* 139.3 (2017), p. 031203 (cit. on pp. viii, xii, xxxii, 91, 115, 117, 132).

[6] L. Battisti et al. "Experimental benchmark data for H-shaped and troposkien VAWT architectures". In: *Renewable Energy* 125.September 2018 (2018), pp. 425–444 (cit. on pp. viii, xxxii, 82, 108, 116).

[7] F. Claudino and E. Passaglia. "Two-dimensional and three-dimensional characterization of vertical axis wind turbines wake by means of hot wire anemometers". PhD thesis. Politecnico di Milano, 2016 (cit. on pp. xi, xii, 60, 65, 90, 112).

[8] K. P. Kundu and I. M. Cohen. *Fluid Mechanics*. Fourth Edi. 2008 (cit. on pp. 11, 93, 139).

[9] A. Minuti. "Applicazione di sonde di pressione a misure di turbolenza: valutazione critica mediante confronto con anemometria a filo caldo". PhD thesis. Politecnico di Milano, 2009 (cit. on pp. 37, 40, 99).

[10] C. De Ponti. "Nota Tecnica". In: (1989) (cit. on p. 51).

[11] A. Perdichizzi, M. Ubaldi, and P. Zunino. "A hot wire measuring technique for mean velocity and Reynolds stress components in compressible flow". In: (1990) (cit. on p. 98).

[12] P. Zunino, M. Ubaldi, and A. Satta. "Un metodo per la misura delle velocità medie e delle tensioni di Reynolds in componenti di turbomacchine mediante sonde a filo caldo". In: (1988) (cit. on p. 107).

Acronyms

HW(A)	Hot Wire (Anemometer)
FRAPP	Fast Response Aerodynamic Pressure Probe
VAWT	Vertical Axis Wind Turbine
GT	Axial-Flow Turbine Stage
LMA	Levenberg-Marquardt Algorithm
NR	Newton-Raphson
LFM	Laboratory of Fluid-Machines
TC	Turbine-Compressor
CC	Constant Current
CT	Constant Temperature
CFD	Computational Fluid-Dynamics